THE ROLE OF CLOUDS IN CLIMATE MODEL BIAS AND SENSITIVITY

CARLO LACAGNINA

The real voyage of discovery consists not in seeking new landscapes, but in having new eyes

Marcel Proust

THE ROLE OF CLOUDS IN CLIMATE MODEL BIAS AND SENSITIVITY

Proefschrift

ter verkrijging van de graad van doctor
aan de Technische Universiteit Delft,
op gezag van de Rector Magnificus prof.ir. K.C.A.M. Luyben,
voorzitter van het College voor Promoties,
in het openbaar te verdedigen op 6 oktober 2014 om 15.00 uur

door

Carlo LACAGNINA

Environmental Physics, Universiteit van Turijn, Italië
geboren te Turijn, Italië

Dit proefschrift is goedgekeurd door de promotor:
Prof. Dr. A.P. Siebesma

Copromotor: Dr. Ir. F.M. Selten

Samenstelling promotiecommissie:

Rector Magnificus,	voorzitter
Prof. Dr. A.P. Siebesma,	Technische Universiteit Delft, promotor*
Dr. Ir. F.M. Selten,	Koninklijk Nederlands Meteorologisch Instituut (KNMI), copromotor
Prof. H. Chepfer,	Université Pierre et Marie Curie
Prof. J. Quaas,	Universität Leipzig
Prof. G. Svensson,	Stockholms Universitet
Prof. Dr. H.J.J. Jonker,	Technische Universiteit Delft
Prof. Dr. Ir. H.W.J. Russchenberg,	Technische Universiteit Delft
Prof. Dr. Ing. R. Klees,	Technische Universiteit Delft, reservelid

*Tevens verbonden ann het KNMI

This thesis was accomplished with financial support from the European Union's Seventh Framework Program (FP7/2007-2013) under grant agreement n° 244067.

Cover illustration by Marco Simeoni - www.marcosimeoni.com

Contents

Frequently used abbreviations

CRE	**C**loud **R**adiative **E**ffect
EIS	**E**stimated **I**nversion **S**trength
ENSO	**E**l **N**iño **S**outhern **O**scillation
FAT	**F**ixed **A**nvil **T**emperature
GCM	**G**eneral **C**irculation **M**odel
ISCCP	**I**nternational **S**atellite **C**loud **C**limatology **P**roject
ITCZ	**I**nter**t**ropical **C**onvergence **Z**one
LTS	**L**ower-**T**ropospheric **S**tability
LWCRE	**L**ong **W**ave **C**loud **R**adiative **E**ffect
MBL	**M**arine **B**oundary **L**ayer
OLR	**O**utgoing **L**ongwave **R**adiation
SLP	**S**ea **L**evel **P**ressure
SST	**S**ea **S**urface **T**emperature
SWCRE	**S**hort **W**ave **C**loud **R**adiative **E**ffect
TOA	**T**op **O**f **A**tmosphere

Summary

Clouds are prominent in the climate system, since they play a major role in the way energy and water are cycled through the atmosphere. One of the most relevant impacts of the clouds on the earth's climate is their interaction with the radiative fluxes. Changes in this interaction in response to an external perturbation are known as cloud radiative feedbacks, which form an important contribution to the climate sensitivity of the Earth. An outstanding unanswered question of climate science is how clouds will change as climate warms. General circulation models (GCMs) are invaluable tools for addressing this issue, but they generally disagree in simulating clouds for present-day and future climate. The main reason is that many cloud-related processes take place on spatial and temporal scales typically smaller than the model grid spacing employed, requiring their treatment by means of parameterizations. Despite parameterizations being constantly improved, they remain an approximate representation of the true atmospheric behavior and introduce substantial uncertainties.

Cloud radiative effects depend critically on both the type of cloud and its frequency of occurrence, which define different cloud regimes. This thesis provides insights into the role of the various meteorological conditions in determining the different cloud regimes and transitions among these. It is shown that in the tropics these cloud regimes can be disentangled in a mid-tropospheric pressure vertical velocity (ω_{500}) and sea surface temperature (SST) phase space. Such a bivariate approach is applied using satellite observations to analyse the cloud changes during El Niño. The transitions between different cloud regimes give rise to opposing cloud feedbacks. The sign of the feedback is controlled by the cloud optical thickness. Furthermore, a novel diagnostic technique is developed to quantify the relative contribution of different meteorological factors controlling the cloud interannual and seasonal variability. Changes in the humidity near the surface and SST in the eastern equatorial Pacific and sea level pressure (SLP) in the western part of the basin describe most of the interannual variability, in terms of cloud cover and radiative effects. In addition, it is found that the well accepted relationship between lower-tropospheric stability (LTS) and marine stratocumulus cloud amount has strong seasonal dependence, especially when spatial variations are taken into account.

The understanding of the underlying mechanisms regulating the interplay between clouds, radiation and meteorological conditions, along with the novel diagnostics developed, have been employed in modeling evaluation. In order to avoid much of the ambiguity when it comes to evaluating cloud simulations with satellite retrievals, satellite simulators are embedded in the model code. This approach is demonstrated to be imperative. Specific physical processes are identified as largely responsible for biases in precipitation, cloud amount and radiative fluxes in the EC-Earth GCM. These include the parameterization of the cloud droplet size, the temperature-dependent parameterization that distinguishes between ice and liquid water phases, the overestimated mass flux and the erroneous detrainment parameterization in the convection scheme.

Based on these identified biases, a number of sensitivity experiments have been carried out and are described in the last part of this thesis. These serve to investigate the impact of cloud-related uncertainties on model biases and radiative feedbacks. This approach helps to understand why GCMs simulate the cloud feedbacks, and by implication the climate system, in the way they do. It is found that the details of the representation of cloud microphysical and convective processes do not appear crucial for the total feedback in the EC-Earth GCM, due to compensating effects, but are relevant for the cloud feedback itself, especially its shortwave component. Finally, connections between model bias and the projection of the tropical cloud response to global warming are demonstrated and discussed.

Samenvatting

Wolken vormen een belangrijke component van het klimaatsysteem, aangezien ze een grote rol spelen in de energie- en waterkringloop van de atmosfeer. Een van de meest relevante effecten van wolken op het klimaat van de aarde is hun interactie met de stralingshuishouding. Veranderingen in deze interactie als gevolg van een externe verstoring worden wolken-stralingsterugkoppelingen genoemd, en dragen bij aan de klimaatgevoeligheid van de aarde. Een belangrijke vraag die onbeantwoord blijft in de klimaatwetenschap is hoe wolken zullen veranderen als het klimaat opwarmt. Algemene circulatie modellen (GCMs) zijn van onschatbare waarde bij het beantwoorden van deze vraag, hoewel ze onderling variëren in hoe ze de wolken in het hedendaags en in het toekomstig klimaat simuleren. De hoofdreden voor deze verschillen is dat veel wolkengerelateerde processen plaatsvinden op ruimte- en tijdsschalen die kleiner zijn dan de typische modelroosterafstanden en tijdstappen van de GCMs, met als gevolg dat deze processen geparameteriseerd worden. Ondanks continue verbeteringen aan deze parameterisaties, blijven ze een benadering van de werkelijke atmosferische processen en introduceren ze aanzienlijke onzekerheden.

Wolken-stralingseffecten zijn kritisch afhankelijk van zowel het wolkentype als van de frequentie van voorkomen, welke samen verschillende wolkenregimes definiëren. Dit proefschrift geeft inzicht in hoe verschillende meteorologische omstandigheden de wolkenregimes en de overgangen daartussen bepalen. Er wordt aangetoond dat deze wolkenregimes in de tropen kunnen worden onderscheiden middels de mid-troposferische verticale snelheid en de zeeoppervlaktetemperatuur (SST). Deze bivariate benadering is toegepast op satellietobservaties om wolkenveranderingen te analyseren tijdens El Nino. De overgangen tussen verschillende wolkenregimes leiden tot tegengestelde wolkenterugkoppelingen, waarbij het teken van de terugkoppeling hoofdzakelijk bepaald wordt door de optische dikte van de wolk. Verder is een nieuwe diagnostische techniek ontwikkeld om de relatieve bijdrage van meteorologische factoren te kwantificeren die de interjaarlijkse- en seizoensvariatie in de wolkeneffecten bepalen. Veranderingen in de luchtvochtigheid nabij het oppervlak en SST bij de evenaar in de Oost-Pacifische oceaan en de luchtdruk op zeeniveau in de West-Pacifische oceaan beschrijven het grootste deel van de variabiliteit in de wolkenbedekking en de stralingseffecten.

Ook is gevonden dat de algemeen geaccepteerde relatie tussen stabiliteit onderin de troposfeer en stratocumuluswolken sterk seizoensafhankelijk is, in het bijzonder wanneer rekening wordt gehouden met het ruimtelijke patroon.

Het begrip van de onderliggende mechanismen die de wisselwerking tussen wolken, straling en meteorologische omstandigheden reguleren, is samen met de nieuw ontwikkelde diagnostiek toegepast in modelevaluatie. Om veel van de ambiguïteit te vermijden die optreedt bij evaluatie van wolkensimulaties met satellietwaarnemingen, zijn satellietsimulators ingebed in de modelcode. Er wordt aangetoond dat deze aanpak essentieel is. Specifieke fysische processen zijn achterhaald die grotendeels verantwoordelijk zijn voor systematische fouten in neerslag, hoeveelheid wolken en stralingsfluxen in de GCM EC-Earth. Hieronder vallen de parameterisatie van de druppelgrootte, de temperatuurafhankelijke parameterisatie die onderscheid maakt tussen de ijs- en de vloeistoffase, de overschatte massaflux, en de parameterisatie van detrainment in de opwaartse convectieve massaflux.

Gebaseerd op deze geïdentificeerde systematische fouten zijn een aantal gevoeligheidsexperimenten uitgevoerd, die beschreven worden in het laatste deel van dit proefschrift. Hiermee wordt de impact van wolkengerelateerde onzekerheden op systematische fouten in modellen en stralingsterugkoppelingen onderzocht. Deze benadering vergroot het inzicht in de wolkenterugkoppelingen in de GCMs en hun invloed op de werking van het gehele klimaatsysteem. De details van de manier waarop de microfysica van de wolken en de convectieprocessen wordt beschreven, blijken niet cruciaal te zijn voor het geïntegreerde stralingseffect in het EC-Earth GCM door compenserende processen, maar zijn wel relevant voor de wolkenterugkoppeling zelf, in het bijzonder voor de kortgolvige stralingscomponent. Ten slotte worden relaties tussen de systematische fouten in modellen en projecties van tropische wolken in een opwarmend klimaatsysteem aangetoond en bediscussieerd.

Chapter 1

Introduction

The earth's climate system is controlled by the radiative energy balance at the top of atmosphere (TOA) between the solar radiation absorbed by the earth and the thermal radiation emitted to space. The distribution of absorbed, scattered and emitted radiation in space and time is strongly modulated by many components of the earth's system, such as absorbing gases in the atmosphere, surface albedo, clouds, etc. The time-space structure of planetary radiation balance is both a driver of and is driven by the state of the earth's climate.

Clouds strongly influence the climate system, for a large part due to their influence on the transfer of solar and thermal radiation. Clouds enhance the planetary albedo through scattering of solar radiation. On the other hand a cloudy atmosphere emits less thermal radiation to space than would do under clear-sky conditions. The two effects are not in balance and the net globally averaged radiative contribution by clouds is negative in the present-day climate. Therefore, clouds strongly cool the planet, reducing the net downward radiation at TOA by about 20 W/m^2 [74, 238]. Taking into account that more than half of the planet is covered by clouds in current conditions, an eventual increase of 10% of cloudiness in future climate would result in a further reduction of the downwelling radiation of 4 W/m^2. This quantity is sufficient to compensate the direct forcing caused by doubling CO_2 concentration in the atmosphere. This simple example demonstrates that small changes in cloud amount can have a dramatic impact on the climate. For this reason understanding what governs clouds and how they respond to a warming planet is a crucial climate question.

Changes in the effect of the clouds on the radiative fluxes in response to an external perturbation are known as cloud radiative feedbacks [232]. The response of the clouds to the climate change and their feedbacks contribute to determine the sensitivity of the earth's climate. Equilibrium climate sensitivity is defined as the global mean surface-air temperature change experienced by the climate system after it has attained a new equilibrium in response to a doubling of atmospheric CO_2 concentrations from preindustrial levels (see section 1.4). According to the Fifth Assessment Report (AR5) of the Intergovernmental Panel on Climate Change (IPCC), the equilibrium climate

sensitivity estimates from general circulation models (GCMs) is likely to lie in the range 1.5 °C to 4.5 °C [149]. The large range of uncertainty is primarily due to the global estimates of the climate feedbacks which differ among these models. In particular, the spread associated with the cloud feedbacks is roughly three times larger than that associated with the other main feedbacks [118]. Therefore, the representation of the clouds in GCMs accounts for much of the uncertainties in climate projections. This is a longstanding issue.

The first quantitative studies to formally incorporate cloud feedbacks in a representation of the climate system began to appear in the early 1970s [87]. From the beginning modeling of clouds has been recognized as one of the most difficult tasks for GCMs [1, 80]. More than a decade later Ramanathan (1987) [237] stated that, despite significant progresses in our understanding of the global mean climate, "cloud feedback continues to be the major source of uncertainty in the surface temperature sensitivity of climate models". At present, this statement is still valid, as reported in the IPCC AR5 [149] and in the EUCLIPSE project summary (http://www.euclipse.eu/downloads/DOW_EUCLIPSE_final.pdf). EUCLIPSE (European Union Cloud Intercomparison, Process Study & Evaluation Project) is an international effort ending in 2014 designed to improve the evaluation, understanding and description of the role of clouds in the earth's climate. Achieving this understanding is not easy, given the complex network of interactions between clouds and the hydrological cycle, the atmospheric dynamics and chemistry, the radiation and aerosols. The present thesis work is done in the context of the EUCLIPSE project and aims to provide insights on the role of the clouds in the model biases and their impact on the climate feedbacks.

In the following subsections of the introduction, the main topics that this four year study has covered are described. These serve to introduce the key questions addressed in more detail in the individual chapters.

1.1 Clouds

Clouds consist of condensed water suspended in the atmosphere. They occur on different spatial and temporal scales, ranging from less than a kilometer to thousands of kilometers in the horizontal direction and from seconds to days in time. Since most of the water vapor is confined to the first 15 km above the surface, the majority of clouds forms in the troposphere.

Clouds are central in the climate system, since they play a major role in the way energy and water are cycled through the atmosphere. Clouds are a fundamental component of the global hydrological cycle, they drive and are driven by the atmospheric and ocean dynamics, they act as wet chemical

reactors and interact with aerosols. One of the most relevant direct impact of the clouds on the earth's climate is their interaction with the radiative fluxes, usually referred to as the Cloud Radiative Effect (CRE). This term was formerly referred to as Cloud Radiative Forcing (CRF) in the literature. The longwave and shortwave components of the CRE at TOA, introduced by Charlock and Ramanathan [177], can be defined as:

$$LWCRE = OLR_{clear} - OLR \tag{1.1a}$$
$$SWCRE = TRS_{clear} - TRS \tag{1.1b}$$
$$NetCRE = LWCRE + SWCRE \tag{1.1c}$$
$$N = -SWCRE/LWCRE \tag{1.1d}$$

where OLR, TRS, OLR_{clear} and TRS_{clear} refer to the Outgoing Longwave Radiation and the Total Reflected Solar radiation at TOA in actual and clear-sky conditions, respectively. The sign convention for the quantities used to define CRE is such that the upward radiative fluxes are positive. The advantage of defining the cloud effect on the earth's radiation budget in this way is that both terms on the rhs of Eq. 1.1 have a long satellite record. These radiative fluxes can be observed directly without making assumptions on the properties of the clouds and without detailed knowledge of the state of the atmosphere [3].
The Longwave Cloud Radiative Effect (LWCRE) depends on the cloud top temperature, the cloud fraction and the emissivity, which in turn depends on cloud microphysical variables, such as the cloud water path.
The Shortwave Cloud Radiative Effect (SWCRE) depends on the cloud fraction and on the cloud albedo, which in turn depends on various microphysical parameters, such as the liquid water and ice water path of the clouds as well as the particle shape and size distribution and phase (liquid or ice).
NetCRE indicates the net contribution of the clouds to the earth's radiation budget.
Moreover, the parameter N depends on both cloud macro- and microphysical properties. Its main characteristic, unlike NetCRE, is its invariance to the cloud fraction [225].

The radiative impact of clouds critically depends on both the amount and type of cloud present [131]. In particular, the contribution of optically thick low-clouds, such as boundary layer stratocumulus, to the TOA net radiative budget is negative [74, 135], since they exhibit high albedo and, owing to their low cloud tops, they emit a similar amount of longwave radiation as the surface of the earth. On the other hand, the net contribution to the TOA radiative budget of the tropical deep convective clouds is nearly zero [225, 238]. These clouds are major contributors in driving the tropical circulation and the hydrological cycle and vice versa. Over the tropical belt, the position

of the different type of clouds is strongly related to the large-scale atmospheric circulation and to the Sea Surface Temperature (SST). Low-level boundary layer clouds (stratocumulus and stratus) are present in regions of large-scale subsidence, most of them are found on the eastern cold side of the tropical ocean basins [7]. In contrast, deep convective clouds (cumulonimbus) are associated with large-scale ascending motions, present over the warm pools of the tropical oceans, in particular over the Indonesian region [226]. In the transition regions between these atmospheric circulation regimes, shallow cumulus clouds are often observed; for instance, the trade wind cumuli are found between the upward and downward branches of the Hadley cell [86, 210]. Fig. 1.1 illustrates this and other aspects, described below, of the interaction between radiation, clouds and large-scale dynamics.

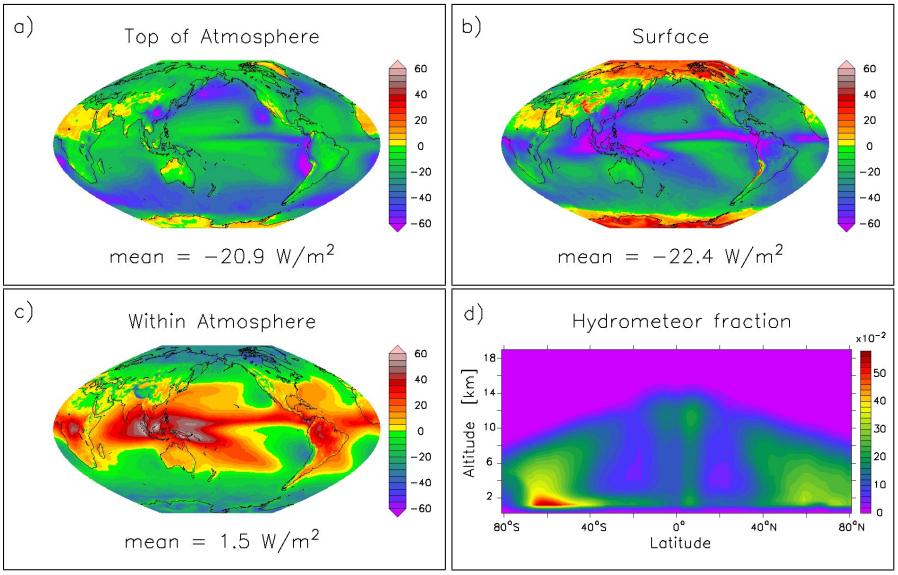

Figure 1.1: NetCRE calculated at the TOA (a), at the surface (b) and within the atmosphere (c) using the CERES-EBAF Ed2.7 product [81, 208] for the period 2000-2010. d) Zonal hydrometeor fraction (clouds and precipitation) for the year 2010 from CloudSat 2B-GEOPROF data [228]. CloudSat is unable to detect clouds in the first 1.2 km above the surface [228]. Observations show the high-clouds in the ITCZ, the downward branches of the Hadley cell associated with the boundary layer clouds and the frontal clouds in the midlatitudes.

On a global average basis, low-clouds make the largest contribution to the net energy balance of the earth and are the most abundant cloud type [e.g. 190]. This latter is a feature of the climate system and arises from fundamental physics involving moist convection and conservation of mass. In a

conditionally unstable atmosphere (cloudy region), upward motion containing saturated air is enhanced by positive buoyancy created through condensation (latent heat release), whereas, in a neighboring clear-sky region, unsaturated downward air movement is hampered by the dry and stable stratification of the atmosphere. This "up-moist, down-dry" asymmetry in convection was first introduced by Bjerknes [236]. According to this theory, convection is favored by rapid rising motion and ascending air currents are faster than related descending currents. Since the downdraft and the updraft velocities are different, the former must be spatially broader than the latter to conserve the total air mass. Therefore, conditions of subsidence, which favor marine low-clouds, prevail [26].

So far the discussion has been limited to the effect of the large-scale atmospheric circulation and SST distribution on the cloud regimes. However, clouds also influence the atmospheric dynamics and temperature. Cloud changes affect the atmospheric circulation by modifying the latent and the radiative heating profiles [112] and through changing the vertical humidity and lapse rate of the atmosphere [231]. For example, deep convective clouds heat the tropical atmosphere relative to clear skies [141] (Fig. 1.1c). This heating fuels the upward branch of the Hadley-Walker circulation [142]. Clouds also influence the SSTs by modulating the solar and thermal radiative fluxes reaching the surface (Fig. 1.1b). This is important, for instance, for the transient response of the atmosphere-ocean system to the El Niño-Southern Oscillation (ENSO) phenomenon [e.g. 35, 126]. ENSO is a regular climate pattern characterized by large interannual variations in the temperature of the sea surface of the tropical eastern Pacific Ocean and in the Walker circulation reflected in changes in the sea level pressure in the western Pacific. Such a change in the meteorological conditions influence the cloud-related properties, which in turn impact the ENSO seasonal phase lock [57, 58]. As a positive (negative) SST anomaly develops in the central Pacific, clouds respond and reflect more (less) solar radiation to space, which reduces (increases) the SST anomaly [239]. That is a negative feedback, but other areas of the tropical Pacific experience a positive cloud feedback. Warmer SST during El Niño enhances convective activity in the eastern tropical Pacific and breaks up the stratiform low-clouds. This leads to an increased solar flux at the surface and enhances the positive SST anomaly [e.g. 213]. This topic is further discussed in chapter 2.

Finally, a more complete picture concerning the interaction between large-scale circulation and clouds requires considering remote effects. In the tropics, the strength of the subtropical inversion, which is observed to be related to the amount of boundary layer clouds [7], is tied to the strength of the Hadley Cell, which in turn is partly determined by the amount of deep con-

vection taking place along the Intertropical Convergence Zone (ITCZ). On the other hand, trade wind cumuli enhance mixing of heat and moisture leading to an increase of the surface evaporation from the ocean. This moisture is transported downstream by the trade winds into the ITCZ, which in turn intensifies deep convection through latent heat release [86, 165]. Moreover, it is a matter of fact that the strength of the subtropical inversion is partly controlled by the free-tropospheric lapse rate. The free-tropospheric temperature in tropical regions of subsidence is mainly determined by the regions of active deep convection and roughly follows a moist adiabat [89]. This is a consequence of the negligible horizontal gradients in the tropical temperature above the boundary layer, due to the weak Coriolis force [88]. Therefore, climate regimes are connected and changes in one region can affect other areas. This is important for future climate analyses as well as for climate modeling. For instance, modification in the moist convection parameterization can influence the marine boundary layer (MBL) cloud evolution, as shown in chapter 5.

Besides the well-known relationship between the atmospheric circulation and cloud-related variables [200, 204], several studies identified correlations between cloud properties and regional or large-scale meteorological conditions at different time scales [90, 209, 239]. For instance, in the stratocumulus regime, the maximum in the amount of boundary layer clouds coincides with the season of largest lower-tropospheric stability (LTS), as observed by [7], or of largest estimated inversion strength (EIS), according to [194]. Moreover, several analyses have identified important environmental factors associated with the transition from unbroken sheets of stratocumulus to fields of scattered cumulus. Increased SST promotes enhanced convective activity which breaks up the low-cloud deck. As the SST increases, the stratocumulus dominated region experiences increasing entrainment of warm and dry free-tropospheric air at cloud top, which leads to a reduction of the transport of warm, moisture-laden air from the surface to the cloud layer. This promotes a situation known as decoupling, where the MBL is decoupled into two turbulent layers with well-mixed stratocumulus at the top of the MBL and sporadic cumulus beneath the stratocumulus. Decoupling reduces the moisture provided from the surface while a significant amount of dry air from above the inversion is entrained into the MBL. As SST increases relative to the air above the inversion, LTS decreases and the MBL deepens, along with a rapid rise in latent heat fluxes. Therefore, changes in the local thermal structure and circulation gradually evaporate the stratocumulus. These mechanisms are described in several studies [e.g. 116, 206].

Relationships between meteorological parameters and cloud-related variables have been identified for deep convective clouds as well. In tropical deep

convective regions the radiative shortwave cooling and longwave heating effects by clouds tend to cancel each other, with the former slightly dominating, so that NetCRE is near zero in the observations (Fig. 1.1a). Kiehl [225] and Cess et al. [46] argued that the dominant factor for this near cancellation is the tropical tropopause temperature in the deep convective regions. In addition, Kiehl [225] stated that CRE is determined by the high-clouds in this region and that changes in the amount of this cloud type are strongly dependent on variations in SST. Further discussion on the relationship between environmental conditions and cloud variability is given in chapter 3.

Quantifying the relative importance of the different processes that control cloud properties may help to understand where and why climate models exhibit a large spread in the cloud feedbacks. The spread among the models in representing cloud feedbacks is present at all latitudes, but it tends to be larger in the tropics [113, 198], with a sizeable contribution from MBL clouds [199]. An example of MBL clouds are the stratocumulus. The amount of this cloud type is usually underestimated by the GCMs, even when the observed SSTs are prescribed [21]. The misrepresentation of cloud properties affects the radiation budget [e.g. 16] and model biases in clouds can stem from their representation in the cloud scheme, the convective mixing scheme, the representation of their microphysics or a combination of any of those. Understanding both how clouds may change in the future and, by implication, the climate system is still an open question [26]. Climate models represent invaluable tools for addressing this issue, but, as mentioned above, GCMs still generally disagree in simulating clouds [2, 111]. In section 1.2 the main reasons for such a large disagreement among GCMs are discussed.

1.2 General Circulation Models

GCMs are numerical models that explicitly calculate the evolution of flow patterns based on fundamental physical laws to yield the complete description of the large-scale motions of the atmosphere or ocean [136]. A system of differential equations is used to calculate the evolution of the atmosphere, ocean and other components of the climate. In order to solve the equations, the planet is divided into a 3-dimensional grid on which the equations are discretized.

GCMs can reproduce a reasonable climatology of the present climate for those quantities that can explicitly be simulated, including the zonal mean flow and the transient eddies in the midlatitudes. Other processes, such as gravity waves, turbulent eddies and clouds are not well reproduced for present climate conditions and lead to disagreement among GCMs' future climate projections [2, 111, 136]. These represent critical limitations, since

GCMs are the main tools we use to predict future climate in sufficient detail to be useful for mitigation and adaptation studies. The main reason for such a disagreement is that some key processes take place on spatial and temporal scales typically smaller than the model grid spacing employed, requiring their treatment by means of parameterizations. These processes are known as diabatic terms and are often associated with subgrid scale fluid dynamics or non-fluid dynamical aspects such as radiative transfer. As an example, Fig. 1.2 shows the contribution of different diabatic tendencies (sometimes referred to as model physical tendencies) to the temperature tendency in a GCM.

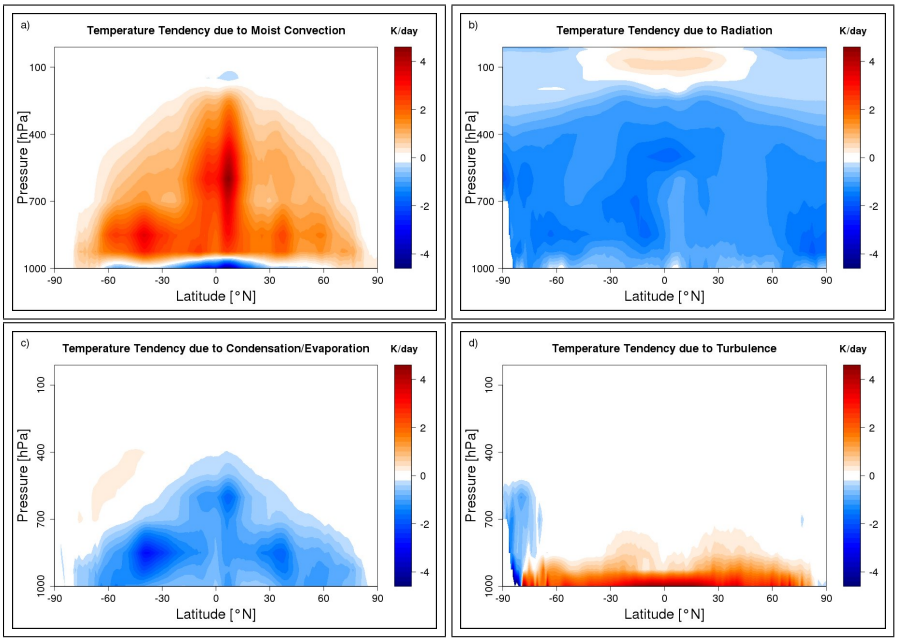

Figure 1.2: Zonal mean temperature tendency due to diabatic processes: moist convection (a), radiation (b), "large-scale" condensation/evaporation (c) and boundary layer turbulence (d). Outputs are from the EC-Earth GCM forced with prescribed observed SST and integrated for the period from 1986 to 2008.

Clouds play a prominent role in each of these processes. In a GCM clouds contribute to at least four relevant effects: vertical transports of moisture, heat and momentum by convection of saturated air; the interaction of the cloud condensate with radiation; the condensation of water vapor, associated with precipitation and release of latent heat; mixing of heat and moisture in cloudy boundary layers. All these processes are not explicitly simulated by

the resolved motion, but are represented statistically by subgrid scale closure theories. Parameterizations aim to capture the essence of the known subgrid processes in simple formulations. The main problem is that the precise mechanisms underlying some key cloud-related processes are not well-understood or are too complex, because of the many thermodynamic, microphysical and dynamical factors that can influence them. Moreover, devising a single parameterization that accounts for the full range of large-scale conditions present in nature is challenging [204]. Every parameterization contains one or more adjustable parameters to relate subgrid processes to large-scale variables explicitly calculated at the grid-box scale. These parameters cannot often be determined on the basis of fundamental principles, but rather are carefully calibrated (tuned) within a physical plausible range that gives the best simulation of the present climate. Therefore, parameterizations introduce substantial uncertainty and the differences among them are a major reason for the differences among models results.

For instance, the cloud amount in a GCM is determined with a parameterization. In the early GCMs, the fraction of the grid-box that a cloud occupies (C) was often diagnosed as a function of the relative humidity (RH) of the grid-box [168]. The simplest example of such a function was given by Sundqvist [92]:

$$C = 1 - \sqrt{\frac{1 - RH}{1 - RH_c}} \tag{1.2}$$

where RH_c is a critical condensation threshold at which cloud is assumed to form. There is neither observational nor theoretical basis to justify the assumption that cloud formation is dependent on a fixed RH_c [52].

An other example is represented by the moist convection parameterization that is often based on a mass flux scheme [166, 175]. In such a parameterization, a cloud ensemble within a grid-box is approximated by one effective cloud (bulk approach), where air moves upward while compensating downward air moves in the cloud-free environment. Upward air is controlled by the mass flux, whose vertical profile depends on the lateral mass exchange between the cloud and the environment, known as entrainment and detrainment. At the turbulence scale, these parameters are often prescribed constants, essentially based on dimensional arguments [61, 181]. Chapter 5 and previous studies [e.g. 84] demonstrate that GCMs are particularly sensitive to the choice of these quantities and, more in general, to the way convection is parameterised.

Moist processes are critical also to the behavior of the boundary layer when it contains clouds, e.g. oceanic stratocumulus. An increasing number of GCMs accounts for these situations by adopting a combination of the eddy-diffusivity and mass flux approaches [155]. This parameterization represents

non-local mixing due to strong up/down-draughts with mass fluxes, while the remaining small-scale turbulent part is described with diffusion. The former estimates the turbulent flux ($\overline{w'\phi'}$) of a moist conserved variable ϕ with:

$$\overline{w'\phi'} = \frac{M}{\rho}(\phi_u - \overline{\phi}) \tag{1.3}$$

where the subscript "u" stands for the updraught properties, M is the mass flux and ρ is the density of the air.
The latter, the eddy-diffusivity approach, is a local first order closure where ϕ is approximated as diffusion by:

$$\overline{w'\phi'} = -K_\phi \frac{\partial \overline{\phi}}{\partial z} \tag{1.4}$$

where K_ϕ is a turbulent diffusivity coefficient.
One of the most critical tasks of such a parameterization is determining the strength of the turbulent diffusion across the inversion. This is often prescribed according to the top-entrainment, given in turn by an additional parameterization [178].

Finally, cloud microphysics is crudely treated by means of parameterizations and sometimes certain relevant aspects are not considered at all, e.g. aerosol-cloud interaction. In addition, radiation transfer calculations in GCMs require assumptions on how cloud layers are arranged with respect to each other along the vertical (cloud overlap assumption). Each assumption has different effects on the radiation budget [179]. All these uncertainties potentially lead to systematic errors in simulating important features of the mean climate and its variability, including ENSO [99] (see also chapter 2), the Madden-Julian oscillation [48], the frequency and intensity of convective precipitation [47].

Model performance evaluation is a first step in order to reduce systematic errors. GCMs are evaluated against observations, usually satellite retrievals (see section 1.3), using metrics, i.e. a quantitative error measurement, and diagnostic techniques. An example of model evaluation is shown in chapter 4.

1.3 Satellite observations and simulators

Many measurement campaigns have been set up to learn more about the dynamics, microphysics and chemistry of clouds. Observations come from different sources: radiosondes, weather ships, aircraft and in particular satellites. Since the 70s measurements from satellites have been increasingly used and now represent the most important source of the global observing network. Satellites are powerful tools as they provide global or nearly-global coverage.

Unlike most of the other instruments, satellites do not measure geophysical variables, but the radiance that reaches the TOA at a given frequency (or channel). The measured radiance is related to the geophysical atmospheric variables by the radiative transfer equation [173].

Let us suppose we know an atmospheric variable, such as the temperature profile. We can then compute uniquely the radiances (I) that a sounding instrument would measure using the radiative transfer equation. This is known as the forward problem.

$$I_\nu = \int_0^\infty B_\nu[T(z)] \frac{\partial \tau_\nu(z)}{\partial z} dz \tag{1.5}$$

where[1] ν identifies a wave number, B_ν is the Planck function and τ_ν is the trasmittance. $\partial\tau_\nu(z)/\partial z$ is the weighting function and represents the contribution of an atmospheric layer extending from level z to TOA.
What actually the satellite instruments do is solving the inverse problem: retrieving the atmospheric temperature profile from a set of measured radiances. Since the weighting functions are generally broad and only a finite number of channels is available, the inverse problem is formally ill-posed, because an infinite number of different temperature profiles could give the same measured radiances [51, 173]. The inverse problem is then reduced by assuming some a priori information in the retrieval algorithms.

When the satellite instruments retrieve cloud properties, the observed radiances are used to detect a wealth of information, e.g. the presence of clouds, the optical depth, the emissivity and sometimes the droplet size. The retrieval of these quantities is influenced by the viewing direction, the instrument resolution, the wavelength used, the orbit of the satellite and the attenuation of the remote signals. These limitations introduce additional uncertainties into the retrievals and make the observation of the same variable different from one satellite to another one. This suggests that more than one source of data is desirable in order to measure the cloud properties properly. Furthermore, all these peculiarities typical of the satellite observations are not present in the GCMs. For instance, the cloud droplets simulated by a model do not depend on the wavelength. In addition, some cloud layers might not be observed from space when shielded by thick upper-level clouds. This implies that the cloud-related variables from GCMs and from remote sensing observations are a priori not the same thing. Therefore, a consistent definition of cloud properties is necessary when it comes to compare model outputs with satellite estimates.

Satellite simulators represent a possible approach to reduce ambiguities in the comparison between model results and satellite retrievals. The simulator is a run-time diagnostic tool that mimics what a satellite would retrieve

[1] Eq. 1.5 is written for clear-sky conditions.

if the real-world atmosphere had the clouds of the model. The use of a satellite simulator also facilitates model intercomparison by minimizing the impacts of how clouds are defined in different parameterizations [2]. In a simulator the input values from the model are converted to a set of subgrid scale profiles by dividing each grid-box into a certain number of subcolumns generated randomly. Each layer of these subcolumns is completely clear or overcast, statistically consistent with the grid-averaged model diagnostics and the cloud overlap assumption. The radiances are then calculated in each subcolumn of each grid-box, that is treated as a satellite pixel (forward problem). Finally, a satellite-like cloud fraction is computed at the resolution of the model grid-box using the radiance profiles, making similar assumptions to those that the satellite algorithm uses (inverse problem). Satellite simulators have been developed for many different satellite instruments, such as MISR [188], Cloudsat QuickBeam [151], CALIPSO GOCCP [83], MODIS [193] and ISCCP [8]. Outputs from this latter can be compared with the longest record of cloud observations and is extensively used in chapters 4 and 5. Unlike the other simulators, it does not make full forward simulations of radiances [2].

Many of the limitations of using satellite instruments are also included in the simulators. For instance, the screening of clouds low in the atmosphere by clouds above when passive sensors are used or the assumption that clouds are single layered. Moreover, some retrieval algorithms (ISCCP) may underestimate the altitude of clouds with partial emissivity, especially if the partially emissive cloud lies above an optically thick cloud. On the other hand, other limitations are not taken into account in a simulator, such as calibration and view angle dependent biases present in the observational dataset [193, 224].

1.4 Climate sensitivity and feedbacks

Representation of clouds in GCMs is an example of parameterization of fast processes that impact crucial aspects of long-term climate characteristics, such as climate sensitivity. Climate sensitivity is the "amount by which an objective measure of climate changes when one of the assumed independent variables controlling the climate is varied" [136]. It can also be used as a metric for the model performance [136]. Commonly, the climate sensitivity is calculated by analysing the global mean surface-air temperature (T_s) change in response to the change in the radiative fluxes at TOA. Shifts in T_s are particularly important, because many regional and global climate responses scale well with it [12]. As T_s changes, many climate variables change in concert. Processes arisen from these changes, that affect the relationship between the imposed forcing and the magnitude of the climate change response, are known as feedback mechanisms. The concept of feedback is used

to characterize the behavior of a dynamic system which takes into account the outputs to modify the features of the system itself and thus to modify the future outputs. Climate feedbacks can either amplify or damp the climate response to an imposed perturbation. The extent to which the climate changes due to an external radiative forcing depends largely on radiative feedbacks [97].

Let R be the net TOA radiative flux. At equilibrium R is zero, i.e. the absorbed shortwave radiation must balance OLR:

$$R = \frac{S_0}{4}(1-\alpha) - OLR \tag{1.6}$$

where S_0 is the insolation and α is the planetary albedo. Let us impose now on the climate system a radiative forcing (ΔF), such as a change in a greenhouse gas concentration or in the solar constant. The climate system responds to ΔF with a change in R to restore the energy balance, which is approximately linearly dependent on the global mean surface-air temperature change ΔT_s, such that:

$$\Delta R = \Delta F + \lambda \Delta T_s \tag{1.7}$$

where λ (< 0) is the *climate feedback parameter* and its inverse is referred to as the climate sensitivity parameter (fluxes are positive downward). The parameter λ determines to what extent T_s needs to change in order for the TOA fluxes to return in equilibrium, i.e. λ must be negative to yield a stable climate. When the climate system reaches a new steady state ($\Delta R = 0$), a new equilibrium temperature is reached as well. If the initial forcing is doubled CO_2, the new equilibrium temperature is named the *equilibrium climate sensitivity* [198].

The total feedback parameter λ is commonly decomposed into the effect of different individual climate components affecting R:

$$\lambda = \lambda_P + \lambda_w + \lambda_l + \lambda_c + \lambda_\alpha + Re \tag{1.8}$$

This separation is based on the assumption of additivity and has been supported by several studies [4, 93, 232]. The rhs of Eq. 1.8 is the sum of the Planck (P), water vapor (w), lapse-rate (l), cloud (c) and surface albedo (α) feedback parameters, plus a residual term (Re), which is small at the global scale (less than 10%) for modest climate changes [163] (see also chapter 5). The sum of λ_P, i.e. the response due to a vertically uniform warming of surface temperature throughout the troposphere, and of λ_l, i.e. the response due to departures from the vertically uniform tropospheric warming, is referred to as the temperature feedback. Finally, λ may also be separated into its longwave and shortwave components.

Different methods have been proposed to diagnose radiative feedbacks. One of these is known as the partial radiative perturbation (PRP) method [232], where the radiative effect of a climate variable (water vapor, clouds, temperature or albedo) is examined by taking that variable from the perturbed simulation and substitute it into the instantaneous flux computation of the control simulation, holding all other inputs fixed. The radiative response is then divided by ΔT_s to compute the feedback strength. An other technique is the so called CRE method [44]. In this case the difference between the clear- and all-sky radiative response is referred to as the CRE and then normalized by ΔT_s. An alternative solution is the radiative kernels method [107]. Using this approach, climate feedbacks are computed as products of two terms: one dependent on the radiative transfer algorithm (kernel) and the other one on the climate response of a specific climate variable. An application of the kernel technique is shown is chapter 5.

Each method has its own strengths and weaknesses, as reviewed in Bony et al. [198] and Soden et al. [108]. In particular, each approach strives to diagnose correctly the cloud feedback. The PRP method biases both the cloud and water vapor feedback calculations, by assuming that all fields are temporally uncorrelated with each other. This implies that cloud changes in response to water vapor changes are not considered. As far as the CRE method is concerned, a sizeable part of the CRE change does not result from a change in cloud properties alone, but it depends also on changes in the environment (temperature, water vapor, surface albedo). Finally, in the radiative kernels approach the cloud feedbacks cannot be evaluated directly, because of strong nonlinearities arising from the vertical overlap of clouds.

As a final step, one would wonder what is the link between feedback parameters and climate sensitivity. In other words, what is the contribution of each feedback to the equilibrium ΔT_s? Following Dufresne and Bony [118], it can be demonstrated that:

$$\Delta T_s = \Delta T_{s,P} + \sum_{i \neq P} \Delta T_{s,i} \tag{1.9}$$

where i indicates a generic climate variable affecting R. $\Delta T_{s,P} = -\Delta F / \lambda_P$ is the temperature response due solely to the Planck feedback. $\Delta T_{s,i} = -\frac{\lambda_i}{\lambda_P} \Delta T_s$ represents the influence of each feedback i on the climate sensitivity.

1.5 Outline of the thesis

The remainder of the thesis is structured as follows.

Chapter 2: Since clouds are intimately coupled with the large-scale circulation, Bony et al. [200] proposed a method to combine cloud-related

quantities with changes in the frequency distribution of the mid-tropospheric vertical pressure velocity (ω_{500}). The present chapter highlights the shortcomings of using this method to sort different cloud regimes. Therefore a diagnostic technique is developed, that enables one to distinguish between different cloud types and their radiative impacts through a bivariate decomposition of the clouds on ω_{500} and SST in the tropical regions. Changes in cloud and radiation properties as a result of changing dynamical and thermodynamical regimes are extremely important, as they determine the sign and strength of the cloud feedback. A few studies have shown that the cloud feedbacks not only change in space, but also in time during the ENSO events [64, 99, 100]. The technique devised in this chapter is applied to analyse the transition between cloud regimes in the ENSO cycle. The use of the El Niño case study illustrates the validity of the diagnostics and its advantages over regime decompositions that use a single variable. The study advances our understanding of the reasons for cloud variability in the tropics and provides some insights related to cloud feedbacks on climate.

Chapter 3: Cloud properties depend on the meteorological conditions. Analysing this relation may help to understand why GCMs exhibit a large spread in the cloud feedbacks. Clement et al. [28] took some steps in this direction by proposing a cloud metric to evaluate GCMs based on the correlation between meteorological quantities and cloud cover. However, they did not go as far as to quantify to what extent the environmental conditions contribute to the cloud changes. This point is addressed in this chapter, that is primarily about a new diagnostic technique, developed by expanding on previous works [28, 200], to quantify the relative contribution of environmental factors to the variability of cloud-related quantities. The method centers on the use of the change in probability distribution functions of the environmental factors to derive the integrated changes in associated cloud properties. The technique is applied to analyse the factors tied to the interannual variation of tropical clouds and seasonal variation of MBL clouds. Furthermore, it is argued that this diagnostic tool can be used as a novel way of testing the fidelity of the cloud simulation in GCMs.

Chapter 4: Climate models still generally disagree in simulating clouds for current and future climate [2, 21, 111]. A practical method to acquire greater confidence in cloud changes for future climate predictions is to assess the realism of the cloud simulation in present-day conditions. The aim of this chapter is to investigate the capability of the EC-Earth GCM to faithfully reproduce the observed CREs, cloud-related variables and precipitation in the recent decades. The model is forced with prescribed observed SSTs and an atmosphere-only experiment is carried out. For the first time, satellite simulators are embedded in the EC-Earth code and used to derive diagnos-

tics more readily comparable to observations. Several satellite products and novel regime-compositing techniques, devised in the previous chapters, are used to isolate the sources of errors in the model. Connections are made between cloud biases and CREs, as well as to specific physical parameterizations within the model that may cause the biases.

Chapter 5: Motivated by the cloud biases found in the previous chapter, the parameterization structure of two physical processes (turbulent mixing and the aerosol indirect effect) is revised in the EC-Earth GCM. These two novel EC-Earth configurations, along with others obtained by altering tunable parameters in the model, serve to carry out sensitivity experiments for present-day and warmer climate conditions. The goal is analysing the impact of the formulation of cloud-related processes on the model biases and climate feedbacks. Connections between model biases in current climate and the strength of the cloud feedbacks are discussed.

In **chapter 6** the main results from this dissertation are summarized. This chapter also discusses the still open questions and what further can be done to explore the consequences of this study.

Chapter 2

Changes in the cloud properties in response to El Niño: a bivariate approach

We analyse the dependence of the cloud radiative effect (CRE) and cloud amount on mid-tropospheric pressure velocity (ω_{500}) and sea surface temperature (SST) and point out the shortcomings of using these two proxies separately as means to separate cloud regimes. A bivariate approach is proposed to overcome these shortcomings and it is used to systematically investigate marine cloud properties at different spatial and time scales in the present-day (1985 to 2001) tropical climate. During the 1997-1998 El Niño, the greatest regional change in CRE and cloud cover coincides with the greatest local change in circulation and SST. In addition, we find that the cooling effect of the stratiform low clouds reduces at the rate of approximately 1 W/m^2 per percent of cloudiness reduction in the subsident cold pools of the Pacific ocean. During El Niño, the transition between different cloud regimes gives rise to opposing cloud feedbacks. The sign of the total feedback is controlled by the cloud optical thickness. More generally, we find that the largest part of the cloud response to El Niño, when averaged over the tropical Pacific, is not directly associated with ω_{500} and SST changes, so other factors must play a role as well.

This chapter has been published as: *Lacagnina C. and F. Selten. Changes in the cloud properties in response to El Niño: a bivariate approach. Climate Dynamics, 40:2973-2991, 2013.*

2.1 Introduction

It has been recognized that clouds strongly affect the earth's climate in a variety of ways over a wide range of time and space scales. The most important of these effects are the changes in the radiative fluxes, which are usually referred to as the Cloud Radiative Effect (CRE). Clouds enhance the albedo of the surface-atmosphere column by scattering solar radiation; at the same time, they emit less thermal radiation to space than the surface-atmosphere column would under clear-sky conditions. The two effects are not in balance and the net globally averaged radiative contribution by clouds is negative [e.g. 74, 238], that is clouds cool the planet.

Changes in CRE in response to an external perturbation are known as cloud feedbacks. Despite the importance of these feedbacks in determining the sensitivity of earth's climate, the fidelity of their representation in climate models continues to remain a topic of debate, because of their large spread among models [42, 144, 216]. This spread is larger than for other feedbacks [107, 118, 187]. As was pointed out by Bony and Dufresne [199], marine boundary-layer clouds are at the heart of tropical cloud feedback uncertainties in climate models; understanding how they may change in a perturbed climate therefore constitutes a crucial part of the cloud feedback problem.

The radiative impact of clouds critically depends on both the amount and type of cloud present [131]. In particular, the contribution of optically thick low-clouds, such as boundary layer stratocumulus, to the net radiative budget is negative [74, 135], since they exhibit high albedo and, owing to their low cloud tops, they emit a similar amount of longwave radiation as the surface of the earth. On the other hand the net contribution to the radiative budget of the tropical deep convective clouds is nearly zero [225, 238]. On a global average basis, low clouds make the largest contribution to the net energy balance of the earth and cover a very large fraction of the tropical area [e.g. 190].

Over the tropical belt the position of the different type of clouds is strongly related to the large-scale atmospheric circulation and to the Sea Surface Temperature (SST). Low-level boundary layer clouds (stratocumulus and stratus) are present in regions of large-scale subsidence, most of them are found on the eastern cold side of the tropical ocean basins [7]. In contrast, deep convective clouds (e.g. cumulonimbus) are associated with large-scale ascending motions, present over the warm pools of the tropical oceans, in particular over the Indonesian region [226]. In the transition regions between these atmospheric circulation regimes shallow cumulus clouds are often observed; for instance, the trade wind cumuli are found between the upward and downward branches of the Hadley cell [86, 210].

Since the large-scale atmospheric circulation in the tropics closely depends

on the spatial distribution of SST [197], perturbations in marine cloud cover could be related with changes in SST pattern, such as those associated with El Niño-Southern Oscillation (ENSO) phenomenon [e.g. 35, 72, 126]. Indeed, studies concerning El Niño variability highlighted that variations in low cloud amount are negatively correlated to the local SST anomaly [183].

So far we discussed the effect of the tropical circulation and SST on the cloud properties. However, clouds also influence the atmospheric dynamics and temperature. Cloud changes affect the atmospheric circulation by modifying, for instance, the latent and the radiative heating profiles [112] and influence the SSTs by modulating the solar and thermal radiative fluxes reaching the surface. This latter represents a well-known atmosphere feedback relevant for ENSO [57, 58]. As a positive (negative) SST anomaly develops in the central Pacific, clouds respond and reflect more (less) solar radiation to space, which reduces (increases) the SST anomaly [239]. That is a negative feedback, but other areas of the tropical Pacific experience a positive cloud feedback. Warmer SST during El Niño enhances convective activity in the eastern tropical Pacific and breaks up the stratiform low clouds. This leads to an increased solar flux at the surface and enhances the positive SST anomaly [e.g. 213]. A few studies have shown that the cloud feedbacks not only change in space, but also in time during the ENSO events [64, 99, 100]. They found that the seasonal evolution of the cloud feedbacks can partly explain the ENSO seasonal phase lock. In this study the role of the clouds in the amplification, peak and decay phases of the 1997-1998 El Niño is further explored at the seasonal scale by distinguishing the different cloud regimes.

Since the clouds are intimately coupled with the large-scale circulation, Bony et al. [200] proposed a method to combine radiation budget quantities with changes in the frequency distribution of the mid-tropospheric vertical motion to isolate the dynamical effect from other environmental factors on the cloud properties. We highlight the shortcomings of using this method to sort different cloud regimes in section 2.4. Therefore a bivariate approach is developed, following Williams et al. [128], which enables a more complete distinction among different cloud regimes (section 2.4.1) and may help to isolate influences on cloud properties other than temperature at the surface and large-scale circulation (section 2.6). Unlike Williams et al. [128], we quantitatively evaluate these influences. In addition, we examine the observed changes in the cloud amounts and CREs associated with the 1997-1998 El Niño, providing physical explanations for such a response to ENSO (section 2.5). The cloud feedbacks involved in the El Niño seasonal phase lock are discussed in section 2.5.1.

2.2 Data

In this study we use monthly mean observations from different sources for the years 1985 through 2001. Top of atmosphere Global Energy and Water Cycle Experiment (GEWEX) Surface Radiation Budget (SRB) Release-3.0 data [96, 120] is extensively used in our analyses. It is archived at the Atmospheric Science Data Center (ASDC) at the National Aeronautics and Space Administration (NASA). Cloud amounts and tropopause temperature are taken from the International Satellite Cloud Climatology Project (ISCCP) data product D2 [246]. Two ISCCP D2 classifications are considered. One provides three cloud types defined only by cloud top pressure P_c (hereafter P_c categories) and one provides nine cloud types classified based on their cloud top pressure and optical thickness τ (hereafter P_c-τ categories) [23, 24]. For SST we use the Extended Reconstructed Sea Surface Temperature (ERSST) data [164] and the Global Precipitation Climatology Project (GPCP) product [195] for precipitation.

Two different reanalysis products are used to provide the vertical pressure velocity at 500 hPa: ERA-40 Reanalysis products from the European Centre for Medium-range Weather Forecasting (ECMWF) [222] and the NCEP/DOE Atmospheric Model Intercomparison Project (AMIP-II) Reanalysis, an updated version of NCEP/NCAR Reanalysis with some significant improvements [154].

All data used here are analyzed over the tropical oceans between 30 °N - 30 °S and they are gridded at $2.5^\circ \times 2.5^\circ$ resolution, the original $1^\circ \times 1^\circ$ SRB and ERSST values are also interpolated to $2.5^\circ \times 2.5^\circ$ grid boxes.

2.3 Methodology

The longwave and shortwave components of the CRE at the top of atmosphere (TOA), introduced in Charlock and Ramanathan [177], can be defined as:

$$LWCRE = OLR_{clear} - OLR \quad (2.1)$$

$$SWCRE = TRS_{clear} - TRS \quad (2.2)$$

$$NetCRE = LWCRE + SWCRE \quad (2.3)$$

$$N = -SWCRE/LWCRE \quad (2.4)$$

where OLR, TRS, OLR_{clear} and TRS_{clear} refer to the Outgoing Longwave Radiation and the Total Reflected Solar radiation, a measure of the outgoing shortwave radiation, at the TOA in actual and clear-sky conditions, respectively. The sign convention is such that upward radiative fluxes are positive.

The Longwave Cloud Radiative Effect (LWCRE) depends on the cloud top temperature, the cloud fraction and the emissivity, which in turn depends on cloud microphysical variables, such as the cloud water path. The Shortwave Cloud Radiative Effect (SWCRE) depends on the cloud fraction and on the cloud albedo, which in turn depends on various microphysical parameters, such as the liquid water and ice water path of the clouds as well as the particle shape and size distribution and liquid or ice phase. NetCRE indicates the net contribution of the clouds to the earth's radiation budget. In addition, the parameter N depends on both cloud macro- and microphysical properties. Its main characteristic, which is different from the NetCRE, is its invariance to the absolute magnitude of the cloud effect and to the cloud fraction [46, 225]. This parameter is evidently different for different cloud regimes and it has a typical value of N $\sim$ 1.2 for deep convective clouds, N $\sim$ 4 for stratocumulus and N $\sim$ 1 for trade cumulus [114].

Several studies investigated the links between radiation, clouds and environmental factors in different ways, here we follow and further develop one of the latest techniques. The Bony et al. [200] method is a technique to decompose the changes in clouds and CREs (hereafter indicated as C) in a dynamic component and a component not related to changes in the large scale circulation, by sorting data of interest as a function of the pressure velocity at 500 hPa (ω_{500}). The monthly mean of ω_{500} defines different dynamical regimes. The range of ω_{500} values is binned and monthly mean values of C from observations are averaged over the region with the same ω_{500} values, in order to get C_ω . Then the tropically averaged temporal change in any cloud or radiative variable ($\overline{\delta C}$) can be expressed as the sum of a term arising from a temporal change in the Probability Density Function (PDF) of ω_{500} (δP_ω), called the *dynamic component* and a term arising from a temporal change in the mean value of the variable binned in each dynamical regime (δC_ω), called the *thermodynamic component*. The analytical formula is:

$$\overline{\delta C} = \underbrace{\int_{-\infty}^{\infty} \delta P_\omega C_\omega \, d\omega}_{\text{dynamic}} + \underbrace{\int_{-\infty}^{\infty} P_\omega \delta C_\omega \, d\omega}_{\text{thermodynamic}} + \underbrace{\int_{-\infty}^{\infty} \delta P_\omega \delta C_\omega \, d\omega}_{\text{co-variation}} \tag{2.5}$$

where P_ω indicates the PDF of ω_{500} and the last term is the co-variation component, which has been found small compared to the other terms [200]. By definition, the thermodynamic component includes every influence that is not captured by changes of ω_{500}, such as SST, atmospheric temperature, moisture profiles, dry intrusions in the free troposphere, etc. In this study we propose an extension of this method to isolate the effect of temperature variations on CRE, hence SST is used instead of ω_{500} as a proxy.

In addition a novel composite technique for clouds is developed. The Bony et al. [200] analysis is not able to distinguish among very different

cloud regimes, such as stratocumulus and trade cumulus regions, subjected to the same ω_{500}, since pools with the same subsiding motion can have very different SST and cloud conditions [114]. In order to enable this distinction we computed a bivariate PDF depending on ω_{500} and SST, which must respect the condition:

$$\int_0^\infty \int_{-\infty}^\infty P_{\omega,sst}\, d\omega dsst = 1 \tag{2.6}$$

so that the tropically averaged C variable can be expressed as:

$$\overline{C} = \int_0^\infty \int_{-\infty}^\infty P_{\omega,sst} C_{\omega,sst}\, d\omega dsst \tag{2.7}$$

This bivariate approach enables a more complete distinction among different cloud regimes, as will be shown in the next section.

The variation in C that occurs within ω_{500} and SST regimes will be used to assess the impact on the cloud properties of other environmental factors, which are not directly related to the large-scale circulation and the surface temperature. Therefore $\int_0^\infty \int_{-\infty}^\infty P_{\omega,sst}\delta C_{\omega,sst}\, d\omega dsst$ may be referred to as the *residual component* of $\overline{\delta C}$ in the bivariate approach. Note that is case of using only ω_{500} as a proxy for the decomposition, the residual component coincides with the thermodynamic component in Eq. 2.5.

2.4 Cloud composite techniques in the tropics

Fig. 2.1 shows various cloud properties and the precipitation as a function of ω_{500} on the left and of SST on the right side. The observational variables are decomposed in ω_{500} (SST) bins following Bony et al. [200], as explained above. Error bars and shadows represent the 95% range of the variations in the 204 monthly decompositions.

Fig. 2.1a shows the PDF of the pressure velocity and the decomposition on ω_{500} of the coverage of four different cloud types. The ISCCP P_c-τ cloud categories are grouped and distinguished only by cloud-top height, following Ockert-Bell and Hartmann [172], but here the low-level clouds are also distinguished by τ. Clouds with tops below 680 hPa and optical thickness greater than 3.6 are defined as "stratocumulus", whereas clouds at the same height with optical thickness less than or equal to 3.6 are defined as "cumulus", following Rossow and Schiffer [246] just grouping stratus and stratocumulus in the "stratocumulus" category. Sorting monthly mean cloud amount in monthly mean ERA-40 mid-tropospheric ω bins enables to distinguish between regions where high clouds are predominantly present and regions governed by low clouds (Fig. 2.1a). The two very different cloud regimes are also highlighted by the GPCP precipitation decomposition on ω_{500} shown in

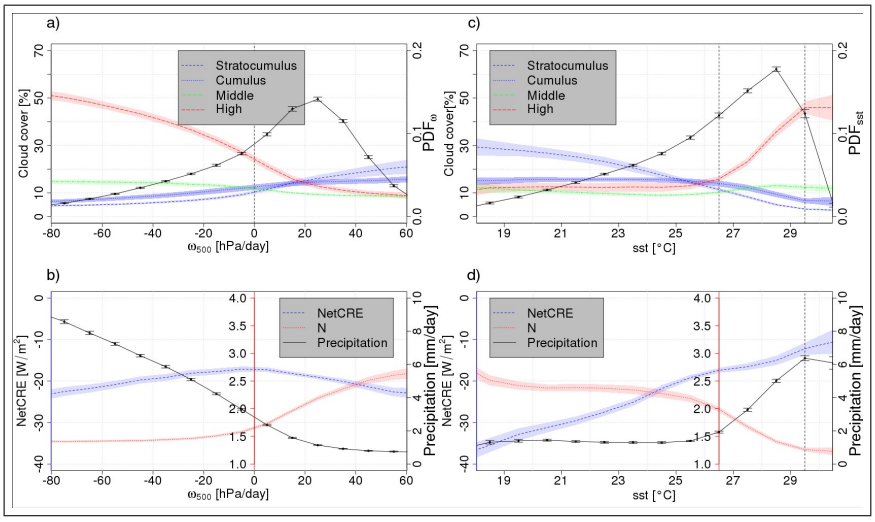

Figure 2.1: Various cloud-related variables composited on monthly values of ERA-40 ω_{500} on the left and of ERSST SST on the right over the tropical oceans (30 °N - 30 °S) during 1985-2001. Shaded areas and vertical bars show the 95% range of the monthly variability. a) Cloud cover (dashed lines) and PDF of ω_{500} (solid line); c) Cloud cover (dashed lines) and PDF of SST (solid line); b) and d) SRB-derived NetCRE, N (=-SWCRE/LWCRE) and GPCP precipitation. ISCCP P_c-τ categories are used for thin ($\tau \leq 3.6$, cumulus) and thick ($\tau > 3.6$, stratocumulus) low-level ($P_c \geq 680$ hPa) clouds, middle-level (440 hPa $\leq P_c <$ 680 hPa) clouds, high-level ($P_c >$ 440 hPa) clouds. The dotted vertical lines in c) and d) indicate the supergreenhouse range limits discussed in the text.

Fig. 2.1b, where the strong precipitation is associated with the high cloud amount in the regions of strong rising motions. Fig.2.1b also shows various CREs based on monthly mean SRB data. The NetCRE is almost independent of ω_{500}; it exhibits values around -20 W/m^2. However, several studies showed that the observed annual mean NetCRE ranges from near zero over the warm pools of the tropical oceans to less than -40 W/m^2 over the eastern cold side of the tropical ocean basins [e.g. 226].

The parameter N has values of about 1.2-1.4 where ω_{500} is negative, which is typical for deep convective clouds, but it reaches values of 2-2.5 where ω_{500} is positive, which is a mixture of values typical for stratocumulus (N $\sim$ 4) and trade cumulus (N $\sim$ 1) [114] . Hence ω_{500} is not a good proxy to distinguish between regions dominated by stratocumulus and regions dominated by cumulus, with very different CRE, as highlighted by the typical N values. We will come back to this in next section where we introduce a diagnostic tool that does distinguish between these two regimes.

Figs. 2.1c-d are similar to Figs. 2.1a-b except for using SST as a proxy instead of ω_{500}. The maximum of the PDF for the temperatures coincides with the supergreenhouse range (26.5 °C - 29.5 °C), a region where OLR_{clear} and SST are inversely proportional. This behavior is known as the clear-sky supergreenhouse effect [239]. Bony et al. [201] have also shown that water vapor, convection and cloud-related parameters behave differently in this particular range of temperature.

The frequency of occurrence of SST values beyond 30 °C decreases dramatically. These pools are generally associated with diminished convection and the presence of hot spots [70, 71]. Finally, the PDF of SST shows a negative skewness toward cold pools, which are regions generally dominated by low-level clouds, in particular the optically thick clouds.

Apparently, using SST as a proxy, one can distinguish between high and low clouds as in the case for ω_{500}, but also between stratocumulus and cumulus clouds (Fig. 2.1c). This better distinction is also evident when looking at the NetCRE in Fig. 2.1d, where a stronger dependence on SST is found. The parameter N reaches higher values, closer to values typical for stratocumulus regimes. SST looks like a good proxy to separate different cloud regimes, but cumulus and upper-level cloud properties are often combined in the same SST-bin. These cloud types have similar impact on NetCRE and N (1 and 1.2 respectively) and therefore SST related shortcomings can not be noted from evaluating the CREs as in Fig. 2.1d.

This point is illustrated by scatter plots of monthly SRB-derived CREs versus ERA-40 pressure velocity on the left and ERSST SST on the right side (Fig. 2.2). Only a randomly selected subset of 1% of all data points is plotted.

Moderate positive ω_{500} bins include both cold (SST < 26 °C) and warm (SST ≥ 26 °C)[1] waters (Figs. 2.2a-c). The former often exhibits much more negative SWCRE values, likely associated with sheets of stratocumulus, whereas the latter is associated with similar low LWCRE but less negative SWCRE, a characteristic of scattered cumulus. A similar ambiguity is shown in Figs. 2.2c-d, where warm SST bins capture both convective ($\omega < 0$ hPa/day) and subsident ($\omega > 0$ hPa/day) regimes. The former is characterized by higher CRE values, associated with upper-level clouds and the latter comprises weak albedo low-clouds. Using SST as a proxy leads to averaging areas with similar SST but different vertical motions and clouds. We further explore this by employing a bivariate approach in the next section.

To a first approximation, if SST would play a dominant role in changing the cloud distribution, one may infer from Fig. 2.1c that, in a warmer climate,

[1] The threshold of 26 °C has been chosen because, beyond this temperature value, the supergreenhouse range begins.

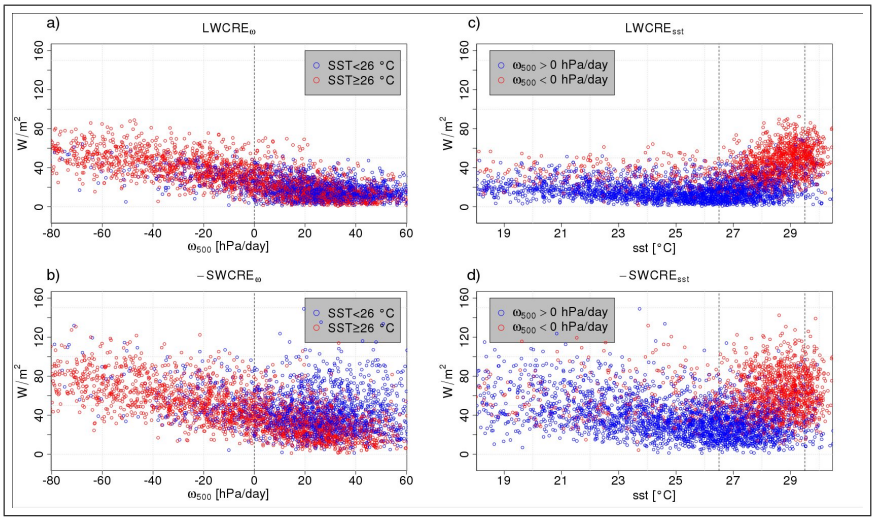

Figure 2.2: Scatter plots of monthly SRB-derived longwave (a-c) and shortwave (multiplied by -1) (b-d) CRE versus ERA-40 ω_{500} on the left and ERSST SST on the right. Only randomly selected 1% of the points over the tropical oceans (30 °N - 30 °S) during 1985-2001 is plotted.

the regions dominated by high-clouds should increase with respect to the regions with stratiform low-clouds. On the other hand Vecchi and Soden [17] showed that the tropical atmospheric circulation weakens consistently in a simulated warmer climate in all CMIP3 models; according to Fig. 2.1a, it would imply a more peaked ω_{500} PDF with the consequent reduction of deep convective regions, associated with high-clouds. Hence the "dynamic" and the "thermodynamic" influences could affect the cloud regime distribution in opposite ways. An assessment of both influences during El Niño is subject of the sections 2.5 and 2.6.

2.4.1 Bivariate composite technique

In the previous section we examined the weak and strong points of using ω_{500} or SST as a proxy to detect and sort different cloud regimes. Here we show that using these two quantities together enables a better distinction among cloud regimes.

Fig. 2.3 is similar to Fig. 2.1 except that a bivariate approach is taken. SRB-derived CRE and ISCCP P_c cloud categories cover are decomposed on ω_{500} and SST, whose bivariate PDF is shown in Fig. 2.3a. The area covered by large-scale subsidence is the most dominant: most of the frequency is

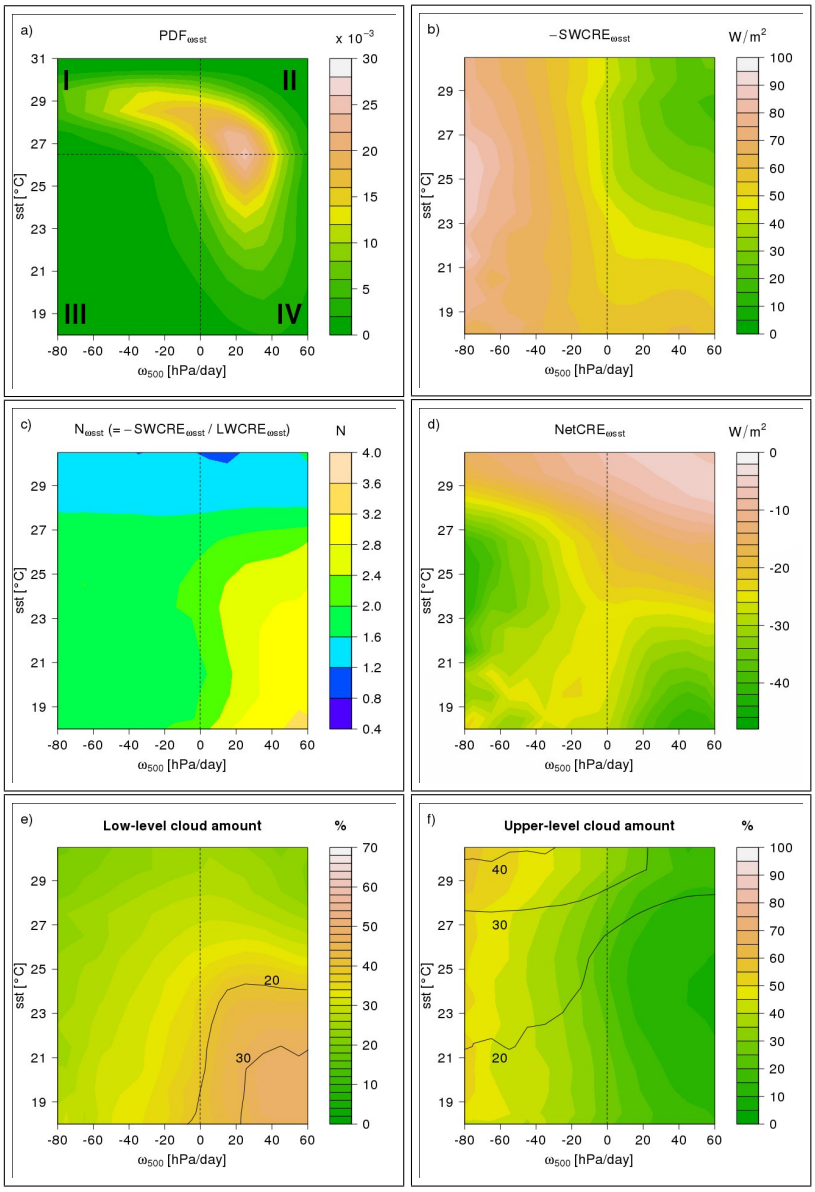

Figure 2.3: SRB-derived CREs and ISCCP cloud cover composited with respect to ERA-40 ω_{500} and ERSST SST over the tropical oceans (30 °N - 30 °S) during 1985-2001. a) bivariate PDF of ω_{500} and SST; dashed lines delimit the four regimes used in Figs. 2.4-2.5. b) (-)SWCRE; c) N; d) NetCRE; e) low-level cloud amount ($P_c \geq 680$ hPa), the black solid lines indicate 20 and 30% of stratocumulus amount ($\tau > 3.6$); f) high and middle level cloud amount ($P_c < 680$ hPa), the black solid lines indicate 20, 30 and 40% of thin high and middle level cloud amount ($\tau \leq 3.6$).

found in the region of moderate warm waters, namely at the edge of the tropical convergence zones. The negative skewness of the PDF of SST, seen in Fig. 2.1c, is here detectable in subsidence areas, namely on the eastern side of the ocean basins, which are covered by a considerable amount of low-level clouds (Fig. 2.3e). The convective areas are particularly frequent in very warm pools, mostly coinciding with the Indonesian region and the Intertropical and South Pacific Convergence Zones (ITCZ, SPCZ), which are governed by upper-level clouds (Fig. 2.3f). The geographical distribution of the ω_{500} and SST fields over the tropics will be discussed below. Finally Fig. 2.3a highlights the non-linear relationship between vertical motion and SST in the tropical belt, which is the main reason for the loss of information in using the two proxies separately.

Compositing the Walker-Hadley circulation with this bivariate approach allows to avoid to average regions with similar vertical motions but different SST. These two regimes present similar LWCRE, but have different albedo, for this reason the (-)SWCRE in Fig. 2.3b ranges from 60 W/m^2 to 15 W/m^2 for the same downward motion ($\omega \sim 40$ hPa/day). The dependence of SWCRE on SST in the subsidence regimes confirms that, also on the large-scale, temperature is one of the factors in the observed transition between unbroken stratiform clouds to scattered cumulus [95, 125, 171]. These different values of SWCRE for the same positive ω_{500} bins are consistent with the parameter N values (Fig. 2.3c), that tend to be higher over the pools where stratocumulus clouds are expected. The upper region of Fig. 2.3c, associated with warmer waters, where LWCRE and SWCRE tend to cancel each other, shows N values of ~ 1.2 or above, typical of deep convective clouds, but also a small area of values around 1, typical of trade cumulus, is found for very warm SST and subsident motions.

The NetCRE gives a measure of the net cooling effect of the clouds. Fig. 2.3d shows that it is stronger over the subsident cold pools, coinciding with the largest amount of the stratocumulus in Fig. 2.3e (black contour lines)[2], and over the convective moderate warm pools, dominated by upper-level clouds, in particular where the thin clouds are less present (Fig. 2.3f black contour lines). The upper-level clouds are defined as the sum of high and middle clouds and, based on their optical depth, they have been sorted in thin ($\tau \leq 3.6$) and thick ($\tau > 3.6$) clouds, following Rossow and Schiffer [246] just grouping cirrus and altocumulus in the same thin upper-level category and the remaining clouds (high and middle) in the thick upper-level category. As shown by Kubar et al. [137], values of τ around 3.6 discriminate between upper-level clouds having a positive or negative effect on the net radiation.

[2]The black contour lines are drawn considering cloud fractions only for day-time, for which the optical depth is available (ISCCP P_c-τ categories). In contrast, the colored contours are drawn considering night and day times (ISCCP P_c categories).

Despite the strong cooling effect of the clouds covering the moderate warm convective pools, their contribution to the earth's radiation budget is quite small compared to the thick low clouds, because of their relatively small frequency of occurrence in the tropics (Fig. 2.3a).

Part of what we have already explained using the bivariate approach can be observed in Fig. 2.4. These are the spatial distributions of the PDF in Fig. 2.3a (expressed in %) and of the cloud properties in Figs. 2.3b-e-f. We show these to clarify the correspondence between large-scale ω_{500}-SST patterns and the cloud regimes, which allows to successfully employ the bivariate technique to distinguish among different cloud regimes. Fig. 2.4(upper-panel) highlights that subsidence occurs over both warm (Fig. 2.4b) and cold (Fig. 2.4d) SSTs, as well as that both upward (Fig. 2.4a) and downward (Fig. 2.4b) vertical motion can be found over similar warm SSTs. Fig. 2.4(lower-panel) shows the very good association between ω_{500}-SST conditions and CREs or cloud types. Beyond the well-known relationship between large-scale downward (upward) motion and low-level (upper-level) clouds and related radiative impact, we point out the correspondence between the highest values of occurrences in Fig. 2.4b, namely the edge of the warm convective zones, and the low values of CREs and cloud amounts in the same areas (Fig. 2.4 lower-panel), likely associated with trade cumulus or mostly clear sky regimes [50].

Three different data sets (ERA-40 reanalysis, SRB and ISCCP) are consistent with each other and it enables to use jointly ω_{500} and SST to sort cloud properties. Particularly relevant is the possibility to disentangle cloud types with similar top height but different optical thickness, such as stratocumulus, cirrus and altocumulus. In several studies stratocumulus regions are separately analyzed [e.g. 7, 95] or merged with other cloud types [e.g. 200], but with this diagnostic tool one can check the behavior of all of these and their radiative contribution in a single analysis. This feature might turn out useful in the analysis of large intermodel differences in the sensitivity of the SWCRE to SST changes, which occur both in climate change and in present-day interannual variability in tropical subsidence regimes [199]. An other advantage of using a bivariate technique compared to the more common approach to look at the spatial distribution is that one can easier estimate the mean relationships among different fields and quantify the relative contribution of different cloud regimes to the tropics-wide climate. We will take advantage of these characteristics when investigating the changes in cloud properties in response to El Niño, in the next section.

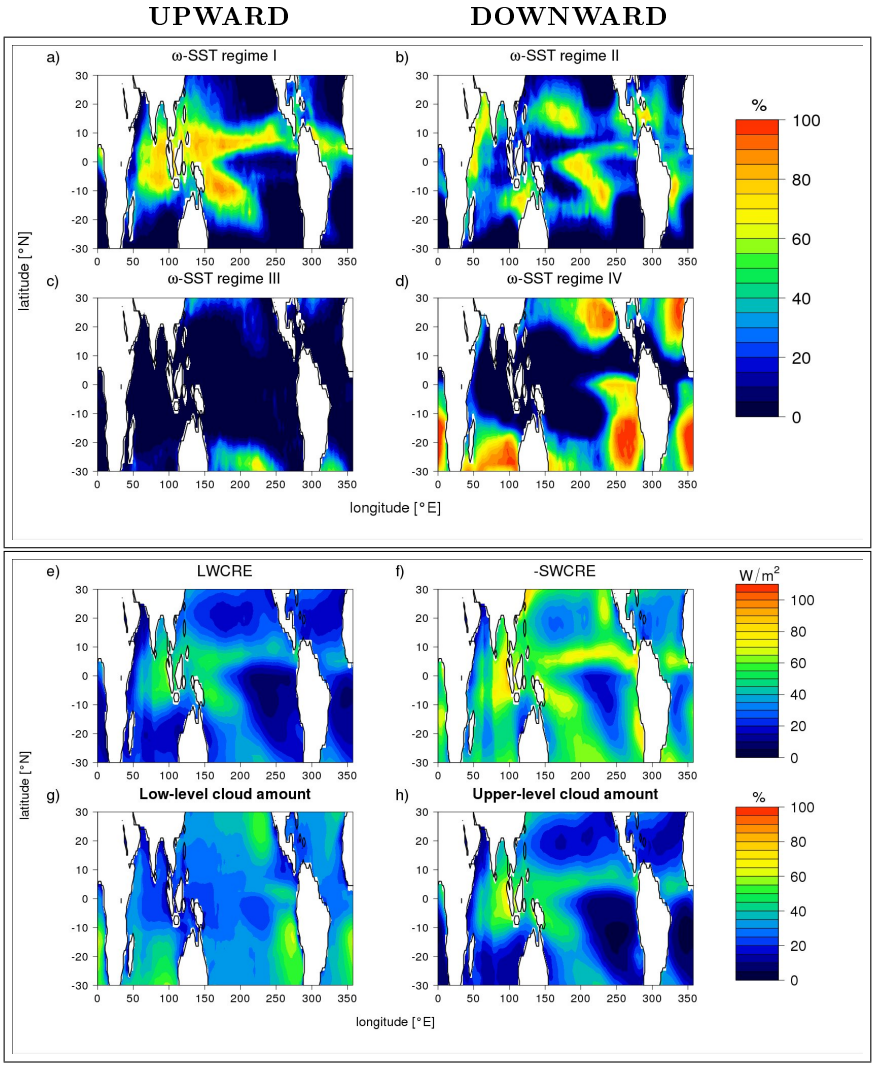

Figure 2.4: Spatial distribution of the frequency of occurrence (expressed in %) of ERA-40 ω_{500} and ERSST SST (upper panel) in four large-scale vertical motion and temperature regimes, as indicated in Fig. 2.3a. Lower panel: spatial distribution of the SRB-derived longwave (e) and shortwave (multiplied by -1) (f) CRE and of the ISCCP P_c categories low-level (g) and upper-level (h) cloud amounts. The period of analysis ranges from 1985 to 2001.

2.5 Changes in cloud properties during El Niño

We now evaluate the relationships among large-scale circulation, SST and various cloud properties which occur in association with the short-term climate anomalies observed in the present-day tropical climate, such as El Niño-Southern Oscillation (ENSO). ENSO is a regular climate pattern characterized by large variations in the temperature of the sea surface of the tropical eastern Pacific Ocean and in the Walker circulation reflected in changes in the sea level pressure in the western Pacific. In this study we will focus on the strongest El Niño event of the last decades and its effect on various cloud-related variables over the tropical Pacific. The El Niño event analyzed here lasted from May 1997 to April 1998. This period has been chosen as the ENSO event, since it is the 12 consecutive months period with the largest warm anomaly in the Niño 3.4 region (5 °N - 5 °S, 120 °W - 170 °W), during 1985-2001. The Niño 3.4 is often used as an index to define ENSO events [e.g. 67].

An overview of the main El Niño effects on the spatial distribution of the large-scale circulation, SST and of the cloud regimes in shown in Fig. 2.5. Fig. 2.5(upper-panel) is similar to Fig. 2.4(upper-panel) except for presenting the anomalies of the frequency of occurrence of ω_{500} and SST; the anomalies (hereafter) are calculated as the mean of the 1997-98 El Niño event minus the climatological annual mean (1985 to 2001). The black solid lines in Fig. 2.5(upper-panel) indicate the statistical significance of the changes at the 95% level, calculated with a two-tailed normal test. Since our sample includes just 17 years, we used the bootstrapping technique to estimate the distribution from a large number of random selections of 12 calendar months from the 17 years of data. The changes in ω_{500} and SST in the regions delimited by the black solid lines are significantly different at the 95% confidence level from the 17 year climatology, due to the El Niño event.

The cold tongue, usually present over the eastern and central equatorial Pacific, becomes warmer, most of it still remains under subsidence conditions (Figs. 2.5d-b), while its western part also becomes convective (Fig. 2.5a). The ascending branch of the Walker circulation shifts eastward, as highlighted by the higher frequency of warm convection particularly over the central equatorial Pacific. At the same time the typical convergence zones, such as the Indonesian region and the SPCZ, experience an unusual intrusion of downward motion; further to the west, the area off the coast of Kenya and Somalia becomes warmer and is affected by more frequent ascending motion. All these are clues of a shift of the Walker circulation and a significant warming of the mean value of SST over the tropical Indian and Pacific oceans.

As mentioned in the introduction, variations in the large-scale atmospheric circulation and SST distribution can affect the cloud regimes. This

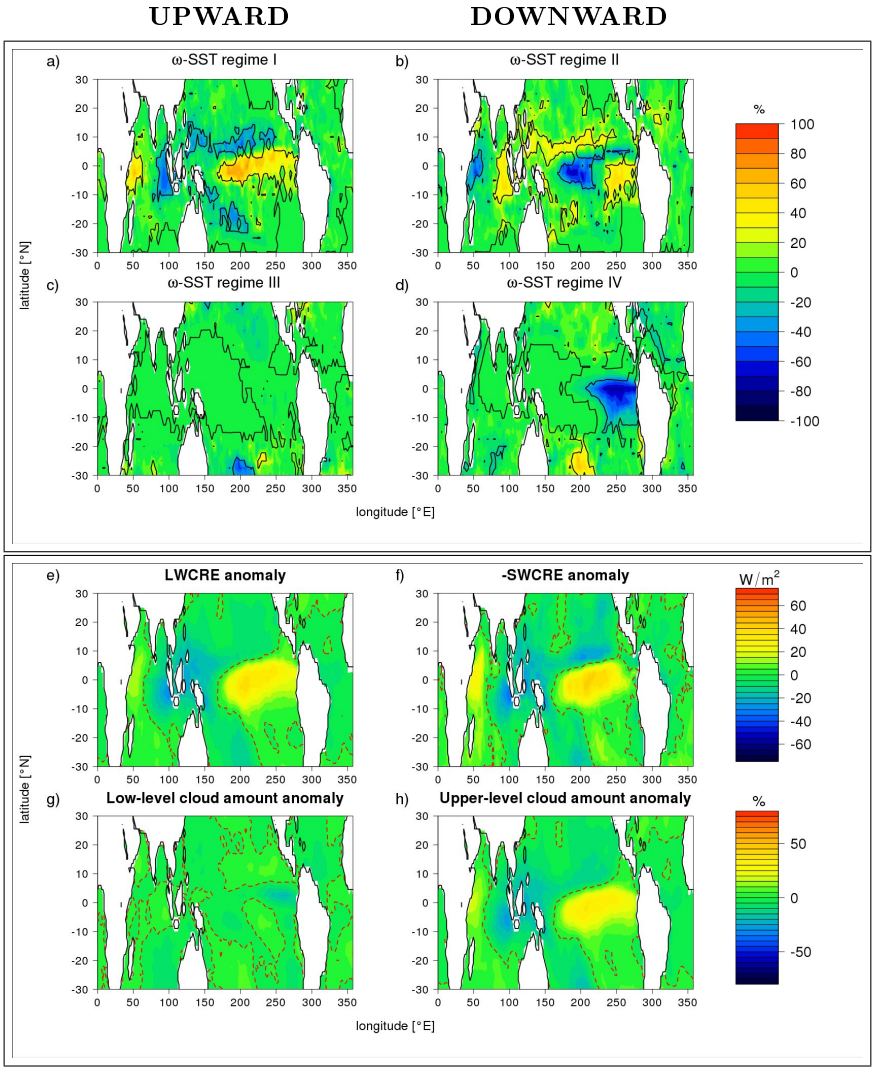

Figure 2.5: As in Fig. 2.4, except for showing the data as the mean difference between 12 months of the El-Niño event (May 1997-April 1998) and the annual mean of period 1985-2001. The black solid lines indicate the statistical significance of the changes at the 95% level, calculated with a two-tailed normal test. The red dashed lines indicate the zero change.

relationship is evident in Fig. 2.5(lower-panel): the changes in the cloudiness and related radiative impact often match the changes in Fig. 2.5(upper-panel). For instance, the increased high cloud amount over the central and

eastern tropical Pacific and off the coast of Kenya and Somalia coincides with the more frequent occurrence of convection over these regions; as a consequence, the LW and SW components of the CRE enhance over the same areas. Interesting is also to note that the greatest low cloud reduction occurs in the eastern tropical Pacific, associated with SSTs which warm and reach the supergreenhouse range (Figs. 2.5b-d), where convection is activated and cloud properties dramatically change, as explained in section 2.4. These observations suggest a correlation between meteorological conditions and cloud-related variable changes which will be explored below.

The changes observed so far can be summarized and better quantified using the bivariate approach. The analysis is now restricted to the tropical Pacific Ocean (30 °N - 30 °S, 100 °E - 280 °E), where most of the ENSO signal remains confined.

Fig. 2.6a shows the difference between the PDF of the 1997-98 El Niño and that of the 1985-2001 climatology. The frequency distribution of the bivariate PDF not only obviously shifts toward warmer waters but it also shifts toward more subsidence, in a region generally favorable for a transition from unbroken sheets of stratocumulus to fields of scattered cumulus, as discussed in the previous section. We point out that the reduction of the regions with moderate positive/negative pressure velocity is only partly offset by the correspondent warmer areas increase. This is more clear when the change in the frequency of occurrence of ω_{500} is examined (Fig. 2.6b): a larger number of grid points with extreme pressure velocity values are found during El Niño, consistently in both two of the major reanalysis projects, ERA-40 and NCEP-DOE. The increased frequency of the strongest upward/downward motions (ω_{500} < -70 hPa/day, ω_{500} > 30 hPa/day) is consistent with an increase in the frequency of intense precipitation events in Fig. 2.6c. The increase in extremes of precipitation is a striking feature of the El Niño phenomenons [e.g. 207].

Fig. 2.7 shows the mean anomalies in CREs and cloud amounts (defined as the monthly $C_i^w - C_i^c$, where i refers to a grid box and the superscripts w, c to the value in this grid box during the El Niño month and the correspondent month in the mean annual cycle, respectively) binned based on the annual cycle (averaged over the 1985-2001 period) 500 hPa ω_{500} and SST bins. The usually subsident warm pools, namely the edge of the Pacific convective zones in Fig. 2.4b, experience an increase of the LWCRE and of the (-)SWCRE[3] (Fig. 2.7a-b), which are very well correlated with the high and middle cloud amount rise (Fig. 2.7d). Conversely, the usually convective zones (Fig. 2.4a) exhibit a reduction of upward motion (Fig. 2.5a) and of upper-level cloud

[3] This CRE component is negative, hence a positive anomaly implies less negative values. To prevent confusion, we chose to show its changes multiplied by -1, in this way negative anomalies must be interpreted as a reduced cloud cooling effect.

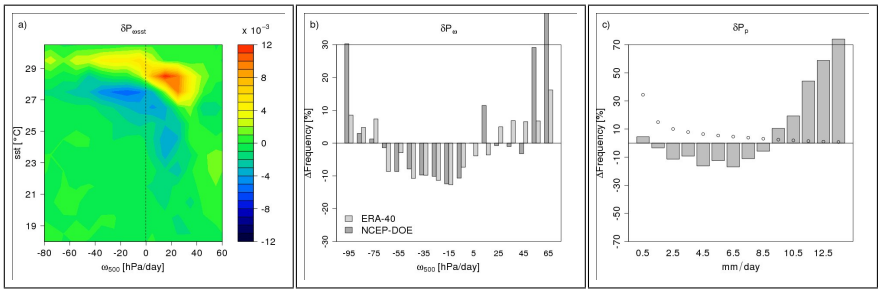

Figure 2.6: The El Niño event (May 1997-April 1998) minus the annual mean of period 1985-2001 change in the bivariate PDF of ERA-40 ω_{500} and ERSST SST (a), in the PDF of ERA-40 and NCEP-DOE ω_{500} (b) and in the PDF of GPCP precipitation (c). The last two are expressed in percentage change of the respective PDFs. The dots in (c) indicate the climatology (1985-2001) of the precipitation PDF expressed in percentage. The analysis is restricted to the tropical Pacific Ocean (30 °N - 30 °S, 100 °E - 280 °E).

amount and their radiative impact (Fig. 2.7). It is consistent with [174], who correlated the unusual intrusion of descending air into regions with strongly rising motion with part of the anomalous value of N (=-SWCRE/LWCRE) and cloud cover in 1998. Moreover, the (-)SWCRE reduction over the subsidence cold pools is associated with the low-level cloud amount drop (Fig. 2.7c), likely because of the transition from stratocumulus, on average detectable in this region (Fig. 2.3e), to scattered cumulus. It appears to be supported by the roughly no change of the LWCRE in Fig. 2.7a, which is tied to the cloud top pressure, similar for these two cloud types.

The regions where most of the CRE changes occur are associated with significant changes in ω_{500} and SST (Fig. 2.5), suggesting a relation between cloud properties and environmental conditions. We now quantitatively explore this relation in order to provide a physical explanation. Fig. 2.8 shows the CRE and cloud fraction anomalies binned based on the regional ω_{500} and SST anomalies ($\omega_i^w - \omega_i^c$ and $SST_i^w - SST_i^c$) over the tropical Pacific Ocean (30 °N - 30 °S, 100 °E - 280 °E).

LWCRE and (-)SWCRE anomalies (Figs. 2.8a-b) are almost linearly proportional to the ω_{500} and positive SST anomalies. The main difference between the two relationships is that the CRE anomaly, in regimes where there is no monthly circulation change ($\Delta\omega_i = 0$), is roughly zero, whereas it is negative for no monthly surface temperature change ($\Delta sst_i = 0$) and insensitive to negative SST anomalies.

The PDFs of the regional ω_{500} and SST anomalies ($\omega_i^w - \omega_i^c$ and $SST_i^w - SST_i^c$) in Figs. 2.8a-b are positively skewed. These PDFs are used as

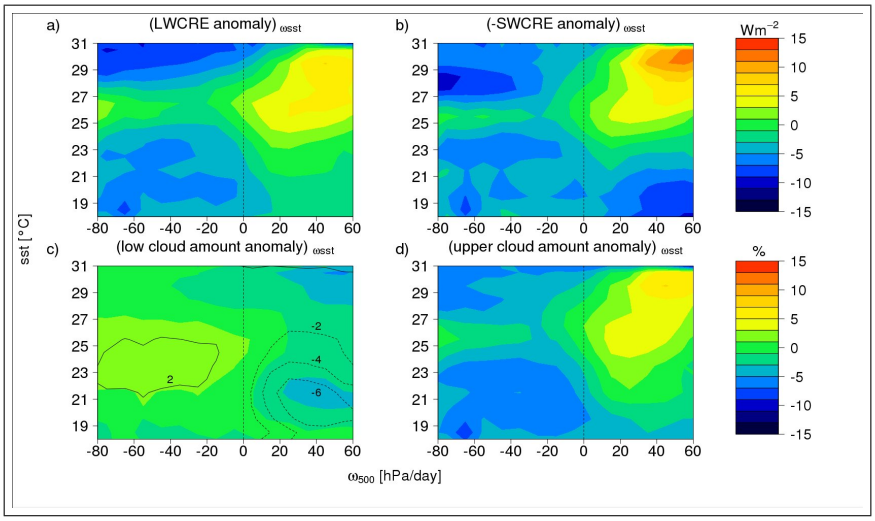

Figure 2.7: Mean anomalies [El-Niño event (12-mo between May 1997 to April 1998) minus the annual mean of period 1985-2001] of SRB-derived CRE (a and b) and ISCCP P_c categories cloud cover (c and d) binned based on the annual cycle (12-mo between 1985 to 2001) ERA-40 ω_{500} and ERSST SST bins. Analysis is for the tropical Pacific Ocean (30 °N - 30 °S, 100 °E - 280 °E). The dashed (solid) black lines in c) indicate the negative (positive) stratocumulus amount ($P_c \geq 680$ hPa, $\tau > 3.6$) anomalies, expressed in %.

statistical weights to quantify the mean NetCRE change that occurred during the 1997-98 El Niño event over the tropical Pacific. This change, based on SRB data, is $+1.0 \pm 1.9$ W/m^2. The large standard deviation reflects the monthly variability which occurs during El Niño with respect to the annual cycle. The slightly positive value implies a reduced cooling effect of the clouds over the tropical Pacific Ocean (30 °N - 30 °S, 100 °E - 280 °E) during the El Niño year (May 97 to April 98 mean SST of 26.6 ± 0.1[4] $°C$) compared to the annual mean (1985 to 2001 mean SST of 26.2 ± 0.2 $°C$). This indicates an overall cloud positive feedback during El Niño. The cloud feedback issue will be further examined in section 2.5.1.

We now analyze the cloud fractions and their role in the NetCRE change during the warm phase of ENSO. The greatest cloud amount anomalies observed during El Niño are due to the high and middle clouds (Figs. 2.7c-d) and these are associated with significant changes in ω_{500} and SST (Figs. 2.8c-d). Both CRE components behave similarly (Figs. 2.8a-b). Based on the

[4]The standard deviation stems from the monthly variability of SST tropically averaged over the Pacific.

results shown in Figs. 2.7-2.8, we propose the following mechanism: higher (lower) SST promotes enhanced (reduced) convection [63, 197], which implies more (less) high cloud amount [e.g. 127], hence higher (lower) CREs.

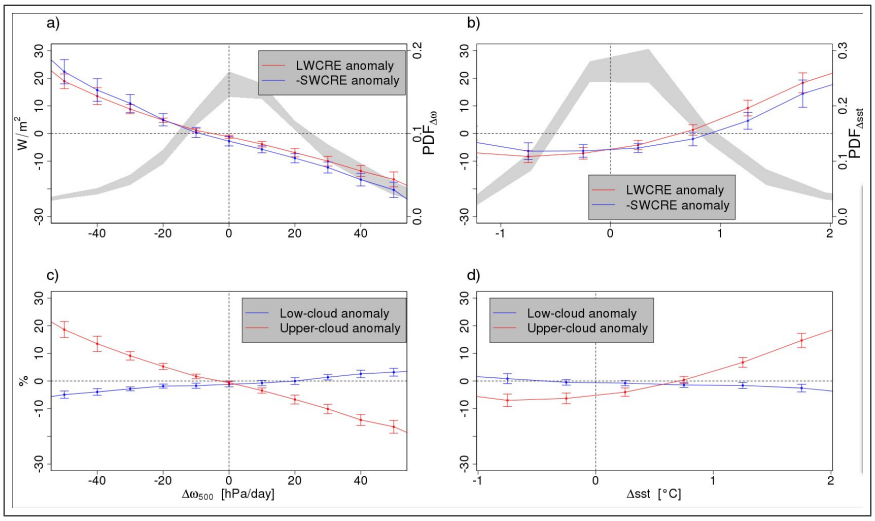

Figure 2.8: Mean anomalies [El-Niño event (12-mo between May 1997 to April 1998) minus the annual mean of period 1985-2001] of SRB-derived cloud radiative effect (a and b) and ISCCP P_c categories cloud cover (c and d) composited with respect to ERA-40 $\Delta\omega_{500}$ (left) and to ERSST Δsst (right). $\Delta\omega_{500}$ and Δsst (right) represent the mean anomalies of ω_{500} and SST, respectively. Frequency distribution of $\Delta\omega_{500}$ (a), Δsst (b) and 95% range of the monthly variability are also shown.

Regarding the low-level cloud anomalies, Fig. 2.7c shows that most of the decrease occurs in regions usually governed by downward vertical motion, in particular in the area of cold pools, where the observed reduction essentially arises from stratocumulus (Fig. 2.7c black contour lines). The similar reduction of low clouds detectable over the warmer waters might be due to the increase of upper-level clouds in that area (Fig. 2.7d). High clouds may obscure part of the lower clouds, due to the "top-down" ISCCP satellite view and thus this reduction is probably overestimated.

Fig. 2.8c shows that negative $\Delta\omega$ values, indicating areas with stronger rising (or weaker subsident) motion during El Niño, are associated with negative low-level cloud anomalies. It is consistent with the mechanism for which enhanced convection breaks up the stratiform clouds in the atmospheric boundary layer [62, 183]. Beside this relationship, reduced low-level cloud amount during El Niño is also correlated with warmer SST (Fig. 2.8d), which has been recognized to be the fundamental driver in the stratocumu-

lus to cumulus transition [25, 125, 171, 202]. In particular, increased SST causes larger buoyancy fluxes and increased entrainment of warm and dry free-tropospheric air at cloud top, which leads to inhibit convection below the cloud base, hence to inhibit the transport of warm, moisture-laden parcels toward the cloud layer, which in turn promotes a situation known as *decoupling*. This decoupling reduces the moisture provided from the surface which, together with the increased entrainment at cloud top and the deepening of the Marine Boundary Layer (MBL), gradually evaporates the stratocumulus [206]. Finally, if the clouds are thin enough, their optical depth may decrease as well, which might cause the observed weakening of the SWCRE over the usually subsident cold pools in Fig. 2.7b.

Moreover, we note a mean stratocumulus fraction reduction of about -6% over the usually subsident cold pools in Fig. 2.7c (black contour lines), which is associated with a (-)SWCRE weakening of about -6 W/m^2 in the same area. This suggests that the stratiform clouds reduce their cooling effect at the rate of approximately 1 W/m^2 per percent of cloudiness reduction in this region.

2.5.1 Cloud feedbacks during El Niño at the seasonal time scale

As ENSO signals have a strong seasonal dependence, it is also interesting to examine cloud changes in different seasons rather than annually. A few studies [e.g. 64, 99] have shown that clouds have a role in the amplification, peak and decay phases of El Niño. We show this by using the bivariate approach.

Fig. 2.9 is similar to Fig. 2.7. The monthly anomalies (September 1996 to August 1998 minus the correspondent month in the mean annual cycle of period 1985-2001) of CREs, optical depth (τ) and cloud top pressure (P_c) are binned based on the annual cycle of ω_{500} and SST bins and then seasonally averaged. SST and ω_{500} anomalies have been composited in the same way and displayed in Fig. 2.9-panel3. The usually subsident warm regions experience an increase of (-)SWCRE and of LWCRE (shadings in Figs. 2.9-panels1-2) during the North Hemisphere spring (MAM) 97 till MAM 98, with a peak during DJF 97-98. These anomalies are in phase with the SST warming in the subsidence regimes, which starts in MAM 97 and develops for approximately 1 year (shadings in Fig. 2.9-panel3; [60]). The (-)SWCRE changes are higher than the LWCRE changes, implying that the cloud contribution to the albedo dominates the cloud greenhouse effect. This gives rise to a negative feedback: the SST warming is constrained by the cooling effect of the clouds. It is due to the presence of thick convective clouds that replace shallow cumuli, notably from JJA 97 to DJF 97-98 seasons. During this El Niño phase, P_c

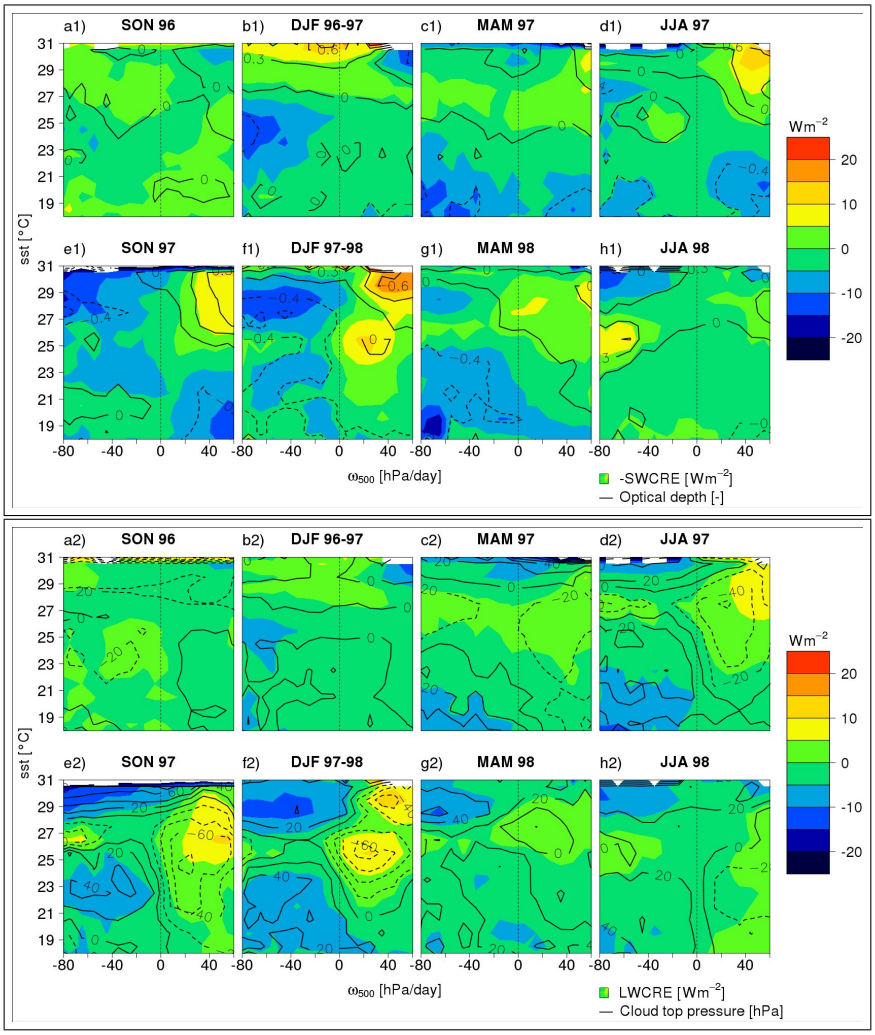

Figure 2.9: Similar to Fig. 2.7: monthly anomalies (September 1996 to August 1998 minus the corresponding month in the mean annual cycle of period 1985-2001) of various quantities are binned based on the annual cycle (averaged over the 1985-2001 period) ERA-40 ω_{500} and ERSST SST bins and then seasonally averaged. The shadings represent the SRB-derived SWCRE (panel 1) and LWCRE (panel 2) anomalies and ERSST SST (panel 3) anomalies. The black solid (dashed) lines indicate the positive (negative) ISCCP optical depth anomalies (panel 1), the positive (negative) ISCCP cloud top pressure anomalies (panel 2) and the positive (negative) ω_{500} anomalies (panel 3). The different seasons are indicated above each box.

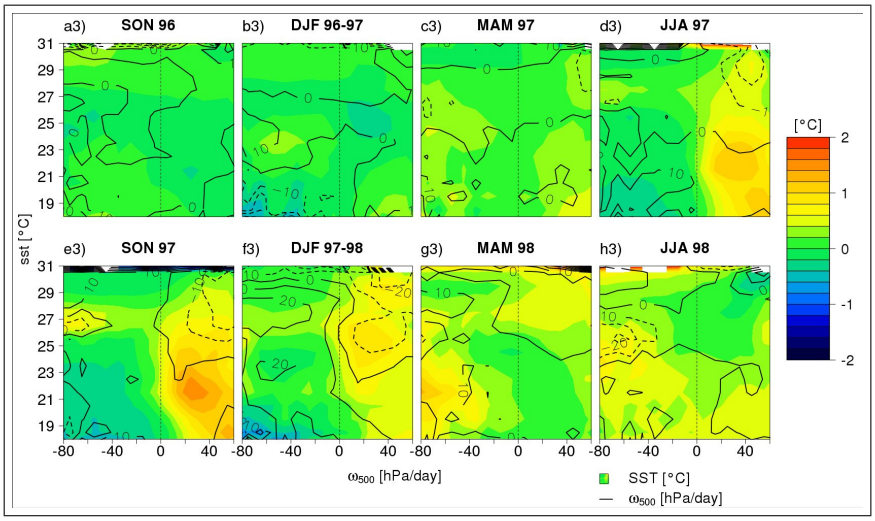

Figure 2.9: *(Continued)*

decreases while τ increases, which are indicators of the presence of higher and thicker clouds. P_c and τ control the LWCRE and the SWCRE, respectively (see section 2.3), while both the CREs depend on the cloud amount, that increases in this area during the El Niño event (Fig. 2.7). Therefore, the changes in τ, although small, play a more important role in determining the sign of the feedback than changes in P_c, i.e. the (-)SWCRE increase dominates on the LWCRE increase. The presence of convective clouds in the usually subsident warm pools is due to the anomalous convective activity (or reduced subsidence) during El Niño (Figs. 2.9d3-e3-f3).

When the 1997-98 El Niño starts (MAM 97), the usually subsident cold pools exhibit a negative (-)SWCRE anomaly, which remains till SON 97 and is associated with roughly no change in LWCRE (Figs. 2.9c-d-e). The changes in the CRE regime are likely due to the transition from stratocumulus, on average dominating this region (Fig. 2.3e), to scattered cumulus. This is consistent with the reduction of τ together with the slightly negative P_c anomaly. The stratocumulus amount also reduces in this area (Fig. 2.7). Therefore, the clouds are less efficient in scattering solar radiation and the surface warms faster. This is a positive cloud feedback, which opposes the negative feedback mentioned above. The two feedbacks are not in phase, indeed the former peaks during SON 97, whereas the latter peaks during DJF 97-98 (Figs. 2.9e-f), which coincide with the phases of maximum and declining ENSO anomaly, respectively in the usually subsident regions. This is consistent to previous findings [64, 99], but here it is shown for the first

time the transition between different cloud regimes. Both feedbacks occur in regions usually associated with similar downward motion, but with very different SSTs. This highlights once more the importance of disentangling different cloud regimes with the bivariate approach.

Finally, we note that CREs in the usually convective warm pools exhibit appreciable changes during the peak and decay phases of the El Niño event (Figs. 2.9e-f-g). The anomalies of the two components of CRE are roughly similar, hence the CRE changes do not produce a relevant direct feedback in this area. We also note that the CRE anomalies are associated with the increase of P_c, which reflects the unusual occurrence of mean subsiding motion over the tropical west Pacific during 1998 (Figs. 2.9f3-g3), consistent with Allan et al. [174].

2.6 Residual component in the bivariate approach

In the previous section we noted that the regional changes in CRE and cloud amounts primarily match the ω_{500} and SST changes. However, some changes in the cloud properties are associated with local processes and meteorological influences which are not captured by the two proxies used so far, and occur within the same ω_{500}-SST bins. The part of the tropically averaged change in a cloud-related variable ($\overline{\delta C}$) that does not directly result from the ω_{500}-SST change is referred to as the *residual component* of the C response to El Niño, an expression of it is given in section 2.3.

In order to show that some changes in C arise under given ω_{500}-SST conditions we composited monthly C in ω_{500} and SST bins for the tropical Pacific Ocean (30 °N - 30 °S, 100 °E - 280 °E). Then the decomposition has been averaged once on the 1997-98 El Niño period (May 1997 to April 1998) and once on the climatological mean state (1985-2001) and the difference gives $\delta C_{\omega,sst}$. Finally, $\delta C_{\omega,sst}$ has been multiplied by the climatological frequency distribution (1985 to 2001) of ω_{500} and SST ($P_{\omega,sst}$). Since ω_{500} and SST conditions are significantly different between the climatology and an El Niño year (Fig. 2.5-upper-panel), the residual component refers to changes which occur in grid boxes associated with the same ω_{500} and SST but, in general, are not associated with the same geographical position.

Various examples of residual components in the bivariate approach are shown in Fig. 2.10. We note they represent the effective contribution of $\delta C_{\omega,sst}$ to $\overline{\delta C}$ because they are weighted by $P_{\omega,sst}$ ($P_{\omega,sst}\delta C_{\omega,sst}$). The greatest contribution to the LWCRE-Residual component decrease comes from the regimes of large-scale warm convection (Fig. 2.10a). It matches in part the reduction of upper-level clouds in Fig. 2.10d and is not com-

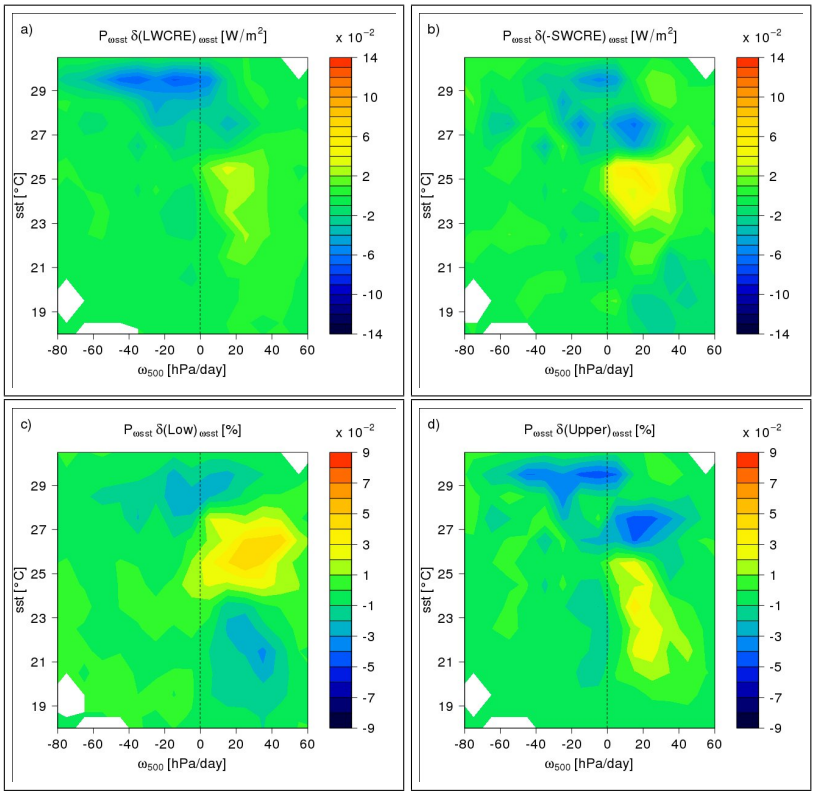

Figure 2.10: Various cloud-related variables composited with respect to monthly values of ERA-40 ω_{500} and ERSST SST during the El Niño event (12-mo mean for May 1997-April 1998) minus its composite in the annual mean (17-yr mean of monthly composites during 1985-2001) ($\delta C_{\omega,sst}$), multiplied by the annual mean bivariate PDF of ω_{500} and SST ($P_{\omega,sst}\delta C_{\omega,sst}$). SRB-derived LWCRE (a) and SWCRE (b). ISCCP P_c categories of low-level (c) and high and middle level (d) cloud amounts. Analysis is for the tropical Pacific Ocean (30 °N - 30 °S, 100 °E - 280 °E).

pletely offset by the (-)SW component decrease (Fig. 2.10b). It leads to a strong negative NetCRE anomaly, which corresponds to an enhanced cooling cloud effect in this area. This effect is also present over moderate warm (23 °C $< sst <$ 26 °C) subsident regions, but in this case it is due to the SWCRE-Residual component strengthening not balanced by the positive LWCRE-Residual component. It is correlated with the increased amount of the low-level clouds (Fig. 2.10c). Finally, the reduction of the low-level cloud amount in subsident cold regimes is likely responsible for the weak-

ening of the SWCRE-Residual component in the same area, while the LW component does not change appreciably. It might indicate the transition from stratocumulus to trade cumulus, which have similar cloud top pressure but different cloud albedo. By definition of residual component this transition occurs independently of circulation and surface temperature changes.

The changes in cloud properties within the same ω_{500}-SST bins observed so far highlight the intrinsic sensitivity of the clouds to other meteorological variables. This term is referred to as the residual component and dominates the tropically averaged cloud property changes (see bivariate-Residual component in Tab. 2.1). In Tab. 2.1 the different components of Eq. 2.5 are reported, calculated using once ω_{500} as a proxy, once SST and once ω_{500} and SST combined (bivariate approach). Note that the integral over the whole ω_{500}-SST range of $P_{\omega,sst}\delta C_{\omega,sst}$ in Fig. 2.10 equals the residual component in Tab. 2.1.

	$[W/m^2]$		[%]	
	LWCRE	-SWCRE	low cloud amount	upper cloud amount
Total ($\overline{\delta C}$)	-0.73	-1.75	-0.97	-0.68
ω-Dynamic	-0.09	0.03	0.04	-0.13
SST-Dynamic	2.09	1.34	-0.90	1.93
bivariate-Dynamic	0.63	-0.81	-0.74	0.41
ω-Residual	-0.67	-1.81	-1.07	-0.55
SST-Residual	-2.68	-3.23	0.09	-2.67
bivariate-Residual	-1.25	-1.01	-0.25	-1.02
ω-Co-variation	0.03	0.03	0.06	0.00
SST-Co-variation	-0.14	0.14	-0.16	0.06
bivar.-Co-variation	-0.12	0.07	0.02	-0.07

Table 2.1: Dynamic, residual and co-variation components (see Eq. 2.5) of averaged change in CRE and cloud amounts ($\overline{\delta C}$) in response to El Niño 1997-98 in the tropical Pacific Ocean (30 °N - 30 °S, 100 °E - 280 °E). The components are calculated once using ω_{500} as a proxy for the decomposition, once using SST and once using the two proxies together (bivariate approach, see section 2.3). Note that the "bivariate-Residual" components are the sum of the values reported in Fig. 2.10 and "Total" is the spatial average of the changes in Fig. 2.6 (lower-panel). SRB and ISCCP P_c categories data are used.

The term arising from changes in the bivariate PDF of ω_{500} and SST ($\int_0^\infty \int_{-\infty}^\infty \delta P_{\omega,sst} C_{\omega,sst}\, d\omega dsst$, bivariate-Dynamic component) falls in between the term arising from changes in the PDF of ω_{500} and SST separated (ω or SST Dynamic components in Tab. 2.1) and in one case (SWCRE) it describes better the changes of C than ω_{500} and SST separately. However, the residual component often contributes most to $\overline{\delta C}$, in all three cases of decomposition. Since the residual component describes the part of $\overline{\delta C}$ that arises within the same ω or/and SST regime, this indicates that a sizable amount of $\overline{\delta C}$ does not directly result from circulation and surface temperature changes

during El Niño. Finally, Tab. 2.1 also shows that the Co-variation components are very weak and generally smaller than the other components.

2.7 Summary and discussion

In the Tropics, cloud properties, such as CREs and cloud amounts, are coupled to the large-scale atmospheric circulation and SST distribution. These relationships can be quantified with the mid-tropospheric pressure velocity ω_{500}, used as a proxy for large-scale rising and sinking motions, or with SST, in order to analyze observed and simulated climate variations at different time scales. In this study, we highlighted the shortcomings of using ω_{500} and SST as tools to sort cloud regimes. In particular, they are not capable to distinguish between regions dominated by very different CRE regimes. Using ω_{500} (SST) as a proxy one averages areas with similar ω_{500} (SST) but different cloud presence. The frequency distribution in a bivariate ω_{500}-SST phase space, highlights the non-linear relationship between these two variables in the tropical oceans (30 °N - 30 °S), which is the main reason for the loss of information about cloud regimes using the two proxies separately.

For this reason we propose a bivariate approach (following Williams et al. [128] to systematically investigate the cloud property climatology and change in response to El Niño. This diagnostic tool enables a better distinction among different cloud regimes, in particular it allows to isolate stratocumulus from other cloud types. One of the main advantages of using a bivariate approach compared to the more common spatial distribution maps is that one can easier estimate the mean relationships among different fields and quantify the relative contribution of different cloud regimes to the tropics-wide climate.

The cloud property climatology has been examined in the period 1985 to 2001. The dependence of SWCRE on SST in the subsidence regimes confirms that, also at the large-scale, temperature appears to be one of the principal factors in the observed transition between unbroken stratiform clouds to scattered cumulus [95, 125, 171]. In contrast, this dependence is very weak for a given value of the large-scale rising motion. We noticed a region of moderate warm convective pools characterized by a strong cloud cooling effect, but its contribution to the earth's radiation budget is quite small compared to the stratocumulus effect, because of its relatively small frequency of occurrence in the tropics.

Part of the present study has been focused on the short-term climate perturbation resulting from the 1997-1998 El Niño. Our analysis, although inconclusive, is not entirely inconsistent with the picture of a strengthened tropical circulation over the Pacific during this event. Clearly, this interpre-

tation needs further validation in future studies.

The usually subsident and warm Pacific pools, namely the edge of the convective zones, experience a strengthening of the LW and SW cloud radiative effect, which matches very well the high and middle cloud amount increasing in the same area. Conversely, the usually convective zones exhibit a reduction of upward motion associated with a reduction of upper-level clouds and their radiative impact. As a result, the NetCRE slightly weakens during the warm phase of ENSO.

During the 1997-98 El Niño, the greatest regional change in CRE and cloud cover are on average associated with the greatest local change in circulation and SST. Observations suggest that higher (lower) SST promotes enhanced (reduced) atmospheric convection [63, 197], which implies more (less) high and middle cloud amount [e.g. 127], hence higher (lower) CREs. An other striking feature of El Niño is that the low cloud fraction change is negatively correlated with stronger rising (or weaker subsident) motion and warmer SSTs. It is consistent with other observational studies [e.g. 183] and appears to be supported by theoretical considerations [206], as briefly explained in the text.

The reduced low cloud amount also contributes to the observed SWCRE decrease in the subsident cold pools of the Pacific ocean. In fact, taking advantage of the bivariate approach, we noticed that the stratiform low clouds tend to reduce their cooling effect at the rate of approximately 1 W/m^2 per percent of reduced cloudiness in this region. We stress that this latter observational evidence can not be obtained just using ω_{500} as a proxy for the decomposition.

As ENSO signals have a strong seasonal dependence [e.g. 64], the cloud changes were also investigated at the seasonal time scale. We show that the transition from shallow cumuli to thick upper-level clouds acts to reduce the amount of solar radiation reaching the surface, contributing to damp the warm SST anomaly during El Niño. On the other hand, the transition from stratiform low-level clouds to scattered cumuli acts as a positive feedback, which contributes to amplify the El Niño anomaly. The two opposing feedbacks coexist during the ENSO events, but they peak in different seasons (DJF for the former and SON for the latter). This is consistent with Guilyardi et al. [64] and Lloyd et al. [99], but here the transition between different cloud regimes is shown for the first time and the related feedbacks are analyzed in greater isolation.

It is also shown that changes in the cloud optical depth (τ) play a prominent role in determining the sign of the cloud feedback during the El Niño seasonal phase. τ controls the SWCRE and is determined by the microphysical properties of the clouds. Climate models exhibit large biases in the

simulation of the cloud microphysical properties [e.g. 170]. Since the SW flux feedback is the main source of model uncertainty when it comes to simulate ENSO events [100], we link this to the biases in the microphysical properties of the (MBL) clouds. Therefore, a more detailed assessment of the biases in the microphysical properties of the clouds, such as water path and droplet size, is needed to reduce the intermodel uncertainties in simulating ENSO. Since ENSO events are primarily associated with large-scale atmospheric and SST changes, analyzing cloud properties in the framework of the bivariate approach provides a useful tool for understanding the source of the ENSO amplitude biases, due to erroneous cloud feedbacks.

However, not all the cloud-related variable variations during El Niño are associated with ω_{500} and SST changes. Using the bivariate approach it is also possible to evaluate the residual anomalies in cloud properties within the same ω_{500}-SST bins (residual component). These residual anomalies describe a larger fraction of the cloud changes, when averaged over the tropical Pacific, than ω_{500} and SST. This indicates that the averaged cloud changes often result from processes other than the direct effect of circulation and surface temperature variations during El Niño.

Finally, this study focused on cloud changes and feedbacks associated with El Niño variations. In a warming climate, the cloud changes and feedbacks might be different. Lu et al. [101] have shown that variations in the large-scale dynamics and thermodynamics of the atmosphere in response to greenhouse gas forcing are very different from the response to El Niño. Zhu et al. [183] claimed that changes in the cloud amount in response to these forcings may involve different mechanisms. Furthermore, Sun et al. [59] have demonstrated that there is no significant correlation between the intermodel variations in the cloud albedo feedback during ENSO and the intermodel variations in the cloud albedo feedback during global warming. However, whilst the planet warms, many studies show that cloud feedbacks arise through a transition from one cloud type to another [e.g. 56, 113]. The ability of the bivariate approach to isolate the cloud properties and feedbacks of the various cloud regimes can thus be exploited in the investigation of cloud changes in a warmer climate and in the interpretation of intermodel differences. This feature of the bivariate approach is particularly relevant in subsidence regimes, where intermodel differences of tropical cloud feedbacks are the largest, both in climate change and in present-day interannual variability [199].

Acknowledgments

The research leading to these results has received funding from the European Union's Seventh Framework Program (FP7/2007-2013) under grant agreement n° 244067.
The authors thank the anonymous reviewers for their thoughtful and constructive comments on the original manuscript. SRB data were obtained from the NASA Langley Research Center Atmospheric Science Data Center. NCEP/DOE data is provided by the NOAA/OAR/ESRL PSD, Boulder, Colorado, USA.

Chapter 3

A novel diagnostic technique to investigate cloud-controlling factors

Cloud properties depend on the local meteorological conditions. This relation is quantified using a simple framework which expands on previous methodologies. This novel diagnostic technique is applied in order to understand and assess the relative contribution of various environmental factors to the observed interannual and seasonal variations in cloud properties. In this analysis framework, sea surface temperature, sea level pressure and, to a lesser extent, the humidity field are the largest contributors to the interannual cloud anomalies in the equatorial Pacific. In addition, in contrast to previous studies, we find that the interannual variability of the ratio of shortwave to longwave cloud radiative effect (N) is independent of the tropopause temperature. Finally, we quantify the role of different factors which are thought to influence the seasonal cycle of the stratocumulus in the subtropics. Off the California coast, the lower-tropospheric stability (LTS) better describes the seasonal low-cloud amount changes than the estimated inversion strength (EIS). When the spatial variation in LTS (or EIS) and low-cloud amount is considered within a season, a different relationship is found that depends on the season. The nonlinear relationships between environmental factors and cloud properties can, to a certain extent, be described within the novel framework proposed.

This chapter has been published as: *Lacagnina C. and F. Selten. A novel diagnostic technique to investigate cloud-controlling factors. J. Geophys. Res. Atmos., 118, 5979-5991, 2013.*

3.1 Introduction

The impact of potential changes in cloud properties as a key factor in the issue of climate change has been recognized since several decades [e.g. 80, 87]. Despite this prominent role of clouds, their representation in climate models continues to be one of the major uncertainties in climate projections [43, 187, 216]. In the tropics, the spread among current models in predicted temperature changes mostly arises from the radiative response of the marine boundary-layer (MBL) clouds to a change in surface temperature [199].

Quantifying the relative importance of the different processes which control cloud properties may help to understand where and why climate models exhibit such a large spread in the cloud feedbacks. Clement et al. [28] took some steps in this direction by proposing a cloud metric to evaluate General Circulation Models (GCMs) based on the correlation between meteorological quantities and cloud cover. However, they did not go as far as to quantify to what extent the meteorological conditions contribute to the cloud changes. This point will be the focus of this paper.

Besides the well-known relationship between the atmospheric circulation and cloud-related variables [200, 204], several studies identified correlations between cloud properties and regional or large-scale meteorological conditions at different time scales [90, 174, 209, 239]. For instance, in the stratocumulus regime, the maximum in the amount of MBL clouds coincides with the season of greatest lower-tropospheric stability (LTS), as observed by [7] or of greatest estimated inversion strength (EIS), according to [194]. Moreover, several analyses identified important environmental factors associated with the transition from unbroken sheets of stratocumulus to fields of scattered cumulus. Changes in sea surface temperature (SST), surface fluxes and entrainment rate of free-tropospheric dry, warm air are considered primary regulators of MBL cloudiness [29, 205, 211]. Free-tropospheric humidity controls to a certain extent the drying effect of the entrained air into the cloud layer and thus plays a role as cloud-controlling factor [95]. Relationships between meteorological parameters and cloud-related variables have been identified for deep convective clouds as well. In tropical deep convective regions the radiative shortwave cooling and longwave heating effects by clouds tend to cancel each other, with the former slightly dominating, so that the ratio between these two effects is near one in the observations. Kiehl [225] and Cess et al. [46] argued that the dominant factor for this near cancellation is the tropical tropopause temperature in the deep convective regions. In addition, Kiehl [225] stated that the cloud radiative effect (CRE) is determined by the high-clouds in this region and that changes in the amount of this cloud type are strongly dependent on variations in SST. The relative importance of these cloud-controlling factors is quantified in the present study applying

an original approach.

Because of the strong relationship between cloud types and local meteorological conditions, it is plausible to expect that changes or shifts, for instance, in the large-scale circulation induce variations in CRE. Based on this idea Bony et al. [200] proposed a method to combine radiation budget quantities with changes in the frequency distribution of the mid-tropospheric vertical motion (ω_{500}) to isolate the dynamical effect from other influences on the cloud properties. We further develop this method using different meteorological variables as a proxy instead of ω_{500} (section 3.3). This study aims to provide a systematic approach to quantitatively assess the relative contribution of different environmental conditions to cloud amount and CRE variations. The novel approach is used to investigate the interannual (section 3.4) and seasonal (section 3.6) cloud variations in the tropical Pacific. Section 3.7 summarizes and discusses the major findings.

3.2 Data

We use monthly mean observations from different sources for the years 1985 through 2001, gridded at $2.5° \times 2.5°$ resolution.

TOA radiative fluxes are retrieved from Global Energy and Water Cycle Experiment (GEWEX) Surface Radiation Budget (SRB) Release-3.0 data [96]. Another similar data set available for a long-term period is the International Satellite Cloud Climatology Project Flux Data (ISCCP-FD) [251], that we also use in our analysis.

Cloud amounts are taken from the International Satellite Cloud Climatology Project (ISCCP) data product D2 [246]. In this data set cloud amount is categorized based on the cloud top pressure (P_c in hPa): high, middle, and low clouds are defined as $P_c < 440$, $440 < P_c < 680$, and $680 < P_c$, respectively. Cloud amount is retrieved from satellite measurements of infrared (IR) and visible (VIS) radiances during day-time, while it can only be obtained from IR radiances for night-time conditions. We use monthly means of day and night retrievals for high and middle clouds, whereas only day-time retrievals are used for low-clouds. The reason for this is that using only IR radiances it is difficult to detect this cloud type. The combined VIS/IR estimates (visible adjustment) are superior and allow to detect more low-level cloudiness [23, 122]. Furthermore, due to the top-down satellite view, low-clouds may partially be obscured by middle and high clouds. Such an effect can be corrected to some extent by assuming that ISCCP low-clouds (L) are randomly overlapped with upper-level clouds (U), following

Rozendaal et al. [13]:

$$L' = \frac{L}{1-U} \tag{3.1}$$

where L' indicates the adjusted low-cloud fraction. In order to be consistent with the low-cloud field, only day-time retrievals for high and middle clouds are used when these enter in the overlap assumption. As stated in Zhu et al. [183], thick low-clouds can only be obscured by thick upper-clouds and not by thin high and middle clouds. This requires a more refined definition of the random overlap assumption, that may be accomplished by modifying Eq. 3.1 in the following way:

$$L' = \frac{L_{thin}}{1-U} + \frac{L_{thick}}{1-U_{thick}} \tag{3.2}$$

where L_{thin} indicates ISCCP thin low-clouds (optical thickness $\tau < 3.6$; $P_c > 680$ hPa), L_{thick} stands for thick low-clouds ($\tau > 3.6$; $P_c > 680$ hPa) and U_{thick} represents thick middle+high clouds ($\tau > 3.6$; $P_c < 680$ hPa). Hereafter only this latter definition of adjusted low-cloud fraction (L' in Eq. 3.2) is considered. Finally, only ISCCP retrievals for day-time are used to characterize the total cloud amount (A_t), as low-clouds can be the largest contributor to A_t in some circumstances, such as in subsident regimes.

For SST we use the monthly mean Extended Reconstructed Sea Surface Temperature (ERSST) data [164]. ERA-40 Reanalysis products from the European Centre for Medium-range Weather Forecasting (ECMWF) [222] are used to provide different atmospheric variables: the vertical pressure velocity at 500 hPa (ω_{500}), the sea level pressure (SLP), the tropopause temperature (TT), the specific humidity at surface (q) and at 700 hPa (q_{700}) and the potential temperature at 700 hPa. The combination of the latter with SST gives a measure of the marine LTS [7]. A refinement of LTS, known as EIS, was proposed by Wood and Bretherton [194] and is calculated as follows:

$$EIS = LTS - (z_{700} - LCL)\Gamma_m^{850} \tag{3.3}$$

where Γ_m^{850} is the moist-adiabatic potential temperature gradient at 850 hPa, z_{700} is the height of the $p = 700$ hPa surface and LCL is the lifting condensation level. Monthly rather than synoptic-scale ERA-40 data are used to retrieve all these quantities. This impacts especially the calculations of LCL and Γ_m^{850}. However, Kawai and Teixeira [85] have shown that the sign of the correlation coefficient between EIS and low-cloud amount is the same at the synoptic timescale as it is at the monthly mean timescale. In addition, the relationship is weaker on timescales less than a month. Therefore, it seems reasonable to study these relationships for monthly means. Finally,

we compute the difference of humidity between the boundary layer and the free troposphere just above (Δq) by subtracting q from q_{700}.

Reanalysis products, such as ERA-40 data, have a number of advantages: good global coverage and long time series and can be used with reasonable confidence [20]. On the other hand, reanalysis products suffer from model biases. Quantities such as latent (LA) and sensible (SE) heat fluxes are computed from parameterizations using surface observations. The Objectively Analyzed Air-Sea Fluxes (OAFlux) project [146] in part reduces this shortcoming. The OAFlux products are constructed from an optimal blending of ground-based observations, satellite retrievals and various atmospheric reanalyses. OAFlux estimates of LA and SE are unbiased and have the smallest mean error compared to the main reanalyses projects [146]. In the present study, LA and SE quantities are taken from the OAFlux dataset.

3.3 Methodology

The longwave and shortwave components of the CRE at the top-of-atmosphere (TOA), introduced in Charlock and Ramanathan [177], are defined as:

$$LWCRE = OLR_{clear} - OLR \quad (3.4)$$

$$SWCRE = TRS_{clear} - TRS \quad (3.5)$$

$$N = -SWCRE/LWCRE \quad (3.6)$$

where OLR, TRS, OLR_{clear} and TRS_{clear} refer to the Outgoing Longwave Radiation and the Total Reflected Solar radiation, a measure of the outgoing shortwave radiation, at the TOA in actual and clear-sky conditions, respectively. The sign convention for the quantities used to define CRE is such that the upward radiative fluxes are positive.

Several studies investigated the links between radiation, clouds and environmental factors in different ways. Here we follow and further develop one of the latest techniques. Bony et al.'s analysis [200] is a methodology to decompose the changes in cloud amount and CREs (hereafter indicated as C) in a dynamic component and a component not related to changes in the large-scale circulation, by sorting data of interest as a function of ω_{500}. The monthly mean of ω_{500} defines different dynamical regimes. The range of ω_{500} values is binned and monthly mean values of C from observations are averaged over the region with the same ω_{500} values, in order to get C_ω . Then, the tropically averaged temporal change in any cloud or radiative variable ($\overline{\delta C}$) can be expressed as the sum of a term arising from a temporal change in the Probability Density Function (PDF) of ω_{500} (δP_ω), called

the *dynamic component*, and a term arising from a temporal change in the mean value of the variable binned in each dynamical regime (δC_ω), called the *thermodynamic component*. The analytical formula is:

$$\overline{\delta C} = \underbrace{\int_{-\infty}^{\infty} \delta P_\omega C_\omega \, d\omega}_{\text{dynamic}} + \underbrace{\int_{-\infty}^{\infty} P_\omega \delta C_\omega \, d\omega}_{\text{thermodynamic}} + \underbrace{\int_{-\infty}^{\infty} \delta P_\omega \delta C_\omega \, d\omega}_{\text{co-variation}} \tag{3.7}$$

where P_ω indicates the PDF of ω_{500} and the last term is the co-variation component. By definition, the thermodynamic component includes every influence that is not captured by changes of ω_{500}, such as SST, atmospheric temperature, moisture profiles, dry intrusions in the free-troposphere, etc. In this study we propose an extension of this method to isolate the effect of different meteorological conditions on C. It is straightforward to compute PDFs for other relevant environmental factors in order to quantitatively evaluate which process is more strongly related to the changes in the cloud properties. Using a generic proxy γ, Eq. 3.7 can be rewritten as:

$$\overline{\delta C} = \underbrace{\int_{\gamma} \delta P_\gamma C_\gamma \, d\gamma}_{\text{environmental forcing}} + \underbrace{\int_{\gamma} P_\gamma \delta C_\gamma \, d\gamma}_{\text{residual forcing}} + \underbrace{\int_{\gamma} \delta P_\gamma \delta C_\gamma \, d\gamma}_{\text{co-variation}} \tag{3.8}$$

The first term on the rhs of Eq. 3.8 will be referred to as the *environmental forcing component* (hereafter γ-EFC) of that specific cloud-controlling factor, which, in the case of $\gamma = \omega_{500}$, coincides with the dynamic component of Eq. 3.7. The second rhs term represents the remaining variation of C which is not directly related to the γ changes (*residual forcing component*). Finally, the *co-variation component* arises from the correlation of γ and non-γ effects in $\overline{\delta C}$. This term is small compared to the others, as will be demonstrated in section 3.4. The different EFCs also imply a decomposition of the so called thermodynamic component in Eq. 3.7, which was found to dominate the change in CRE tropically averaged [200]. Obviously, the EFCs calculated in this way are not independent of each other and it is true that in nature all processes contributing to a certain relationship between two variables are interdependent and occur simultaneously [156]. Using the method described above, we determine the relative contribution of different environmental factors (γ) to the observed cloud-related variable changes ($\overline{\delta C}$).

3.4 Environmental forcing components in the interannual variability

It has already been emphasized in the introduction that different meteorological conditions influence the properties of clouds and their variations. ω_{500}

and SST are intimately coupled with clouds [e.g. 200, 201], but also LTS [7], SLP [28], Tropopause Temperature (TT) [46], specific humidity at the surface (q) and at 700 hPa (q_{700}) [95], latent (LA) and sensible (SE) heat fluxes [206] have been observed to play a role in the cloud property variations.

Therefore cloud-related variables (C) vary with the different meteorological conditions examined in these studies. These variations can be described by changes in the PDF of a specific environmental factor (γ) to extract its effect on the cloud property of interest (γ-EFC), as explained in section 3.3. We will analyze the interannual variations in marine CREs and cloud amounts in a restricted area of the tropical east [7.5 °N - 7.5 °S, 200 °E - 280 °E; (EP)] and west [10 °N - 5 °S, 100 °E - 170 °E; (WP)] Pacific. Other authors chose these regions to study interannual changes in the cloud properties [45, 114] and often interpreted their findings in connection to El Niño-Southern Oscillation (ENSO). The EP region is characterized by low-level clouds and a considerable interannual variability in spatially-averaged SST (±1.1 °C) and the WP region by upper-level clouds and small, to within ±0.3 °C, SST interannual anomalies. Both regions experience a great reduction in their typical cloud population during the positive ENSO phase [e.g. 213].

In order to get the environmental forcing component (EFC) of a particular environmental factor (γ), CREs and cloud amount (C) are composited with respect to monthly means of γ. The range in which γ varies is binned and monthly mean values of C are averaged over the region with the same γ values, to get monthly C_γ^m. For each month, the number of occurrences of each γ-bin normalized by the total number of occurrences in the area considered is referred to as the PDF of γ (P_γ^m). The 17-yr mean (1985-2001) of monthly C_γ^m and P_γ^m gives the climatological mean-state C_γ and P_γ, respectively. Finally, the mean-state P_γ is subtracted from the 12-mo mean of monthly P_γ^m of a specific year, to get the annual anomaly δP_γ. The integral over all γ range of $\delta P_\gamma C_\gamma$ of a particular year, is referred to as γ-EFC and defines the contribution of γ to the annual anomaly of C ($\overline{\delta C}$). $\overline{\delta C}$ is the spatially-averaged annual mean C when the climatological mean-state (17-yr mean of 1985-2001) is removed (see also the explanation of the methodology in section 3.3).

As an example of application of the method, Fig. 3.1a shows annual mean time series of high-cloud amount (for brevity referred to as C here) in the EP region together with various γ-EFCs. The high-cloud anomalies ($\overline{\delta C}$, black line) match very well the magnitude and the variability of ENSO: they are positive during El Niño (e.g. 1987, 1992, 1997) and negative during La Niña (e.g. 1988, 1999) years. The EFCs show that the SST changes exert a stronger control on $\overline{\delta C}$ compared to the ω_{500} changes. Indeed, the contribution of ω_{500} (ω_{500}-EFC) often falls below the annual anomalies of C,

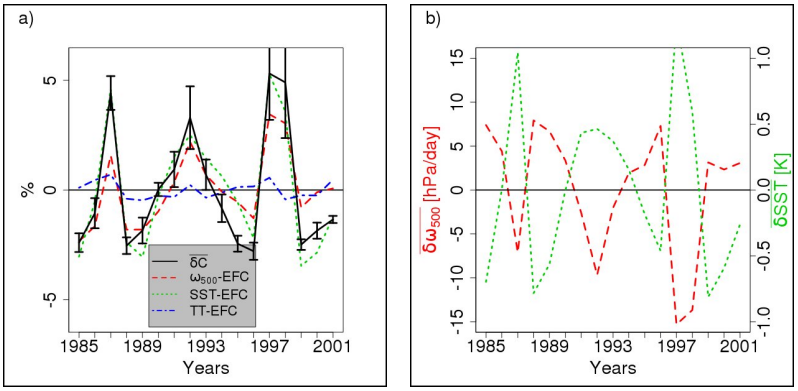

Figure 3.1: a) Anomalies of annual mean spatially-averaged marine ISCCP high-cloud amount (C) relative to the annual mean of period 1985-2001 ($\overline{\delta C}$), together with EFCs of ERA-40 ω_{500}, tropopause temperature (TT) and ERSST SST. Error bars are 95% ranges of monthly variability of C. Analysis is for the East Pacific Ocean (7.5 °N - 7.5 °S, 200 °E - 280 °E). The correlation and regression coefficients between $\overline{\delta C}$ and γ-EFC are given in Tab. 3.1 in the row labeled "environmental forcing components (EFCs)". b) Anomalies of annual mean spatially-averaged ω_{500} (red line) and SST (green line) relative to the annual mean of period 1985-2001.

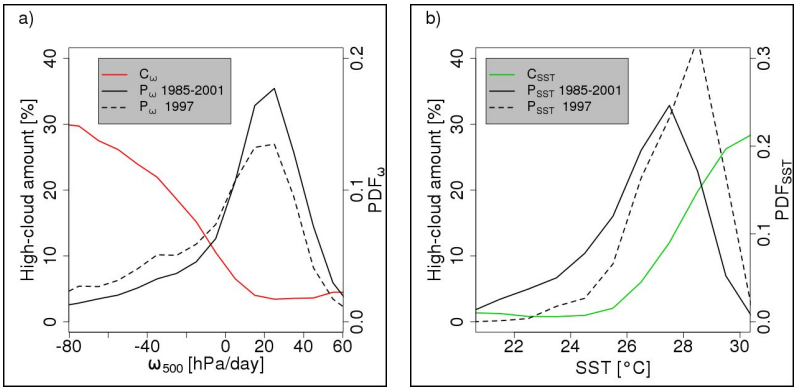

Figure 3.2: The black lines indicate the PDF (P) of ERA-40 ω_{500} (a) and of ERSST SST (b). The black solid lines indicate the mean of the monthly PDFs for the period 1985-2001. The black dashed lines are the mean of the monthly PDFs for the 1997 El Niño year. Colored lines are marine ISCCP high-level cloud amount (C) composited on monthly values of ω_{500} (a) and SST (b) during 1985-2001, in the East Pacific region (note that $\int_\gamma \delta P_\gamma C_\gamma \, d\gamma$, with $\gamma = \omega_{500}$ or SST, equals the values in Fig. 3.1a for the year 1997).

although it predicts correctly their sign. The contribution of SST (SST-EFC) tracks $\overline{\delta C}$ closer. This translates in a high correlation coefficient between ω_{500}-EFC or SST-EFC and $\overline{\delta C}$ for both factors, but in a lower value of the slope of the linear regression between ω_{500}-EFC and $\overline{\delta C}$ than between SST-EFC and $\overline{\delta C}$. In general, the higher the correlation coefficient, the more similar the frequency and the phase of the two signals (γ-EFC and $\overline{\delta C}$). The closer to 1 the slope of the linear regression, the closer the amplitude of the two signals. Fig. 3.1a also shows the EFC of TT, which is an example of a signal that poorly tracks $\overline{\delta C}$, both in amplitude and in phase.

When statistically significant, the correlation coefficient between γ-EFC and $\overline{\delta C}$ is always positive by construction. This is illustrated in Figs. 3.1-3.2. Fig. 3.1 shows the well-known relationship between convective activity and high-clouds [e.g. 183], which leads to a negative correlation coefficient (compare the red line in Fig. 3.1b and the black line in Fig. 3.1a). The ω_{500}-EFC (Fig. 3.1a), on the other hand, is positively correlated with the high-cloud cover. For instance, the 1997 El Niño year is characterized by more convective activity (i.e. more negative ω_{500} values) in the EP region, as a consequence the PDF of ω_{500} (Fig. 3.2a) shifts towards higher values of the binned high-cloud amount (C_ω). This leads to a positive ω_{500}-EFC for the year 1997 (Fig. 3.1a), which correlates positively with $\overline{\delta C}$. In contrast, $\overline{\delta\omega_{500}}$ is negative for the same year (Fig. 3.1b) and correlates negatively with $\overline{\delta C}$. During El Niño also SST tends to increase in the EP region and the relative PDF shifts towards higher values of C_{sst} (Fig. 3.2b). As a consequence, SST-EFC is positive for the year 1997 (Fig. 3.1a). In this case, since the correlation between SSTs and high-cloud anomalies is also positive (Fig. 3.1b), the sign of the correlation is consistent between $\overline{\delta C}$ correlated to $\overline{\delta\mathrm{SST}}$ and $\overline{\delta C}$ correlated to SST-EFC. Therefore, the correlation coefficient between γ-EFC and $\overline{\delta C}$ is adjusted using the sign of the correlation between spatially and yearly averaged C and γ, to make the actual relationship visible.

The above figures and discussion are intended to clarify how the values reported in Tab. 3.1 are calculated and why it is necessary to study both the correlation (first row) and the slope of the linear regression (second row) between $\overline{\delta C}$ and γ-EFC.

Along with the correlation and regression coefficients between $\overline{\delta C}$ and γ-EFC, the third row of Tab. 3.1 reports the slope of the linear regression between $\overline{\delta C}$ and the co-variation component of Eq. 3.8. The small values demonstrate that this term describes very little of $\overline{\delta C}$, thus it can be neglected in our analysis. Finally, in the fourth row of Tab. 3.1 is shown the correlation coefficient between the spatially and yearly averaged γ environmental factors and the high-cloud amount anomaly ($\overline{\delta C}$), following Clement et al. [28]. The correlation coefficients are generally similar to those arising using the EFCs

High-cloud amount ($\overline{\delta C}$)	γ environmental factors									
	ω_{500}	SST	LTS	SLP	TT	q	q_{700}	Δq	LA	SE
Environmental Forcing Components (EFCs)	**-0.91**	**0.95**	**-0.52**	**-0.78**	-0.30	**0.90**	**0.75**	**0.63**	**0.85**	**0.68**
	0.56	**0.94**	**0.32**	**0.42**	0.04	**0.89**	**0.86**	**0.23**	**0.13**	**0.23**
Co-variation	0.02	0.00	-0.03	-0.01	0.00	0.02	-0.01	0.07	-0.01	0.03
Clement et al. [28]	**-0.96**	**0.92**	**-0.60**	**-0.80**	-0.31	**0.86**	**0.76**	0.03	**0.83**	**0.52**

Table 3.1: Statistical relationships between spatially and yearly (1985 to 2001) averaged climate anomalies over the East Pacific Ocean (7.5 °N - 7.5 °S, 200 °E - 280 °E). Statistical significance of the values is calculated with a one-tailed t test. The effective degrees of freedom are derived from the lag-1 autocorrelation. The values that are statistically significant at the 95% level are shown in bold. First two rows: Correlation (first row) and slope of the linear regression (second row) between high-cloud amount annual anomalies ($\overline{\delta C}$) and various γ-EFCs. Third row: Slope of the linear regression between $\overline{\delta C}$ and various γ-co-variation components (see Eq. 3.8). Fourth row: Correlation between $\overline{\delta C}$ and various environmental factors (γ), following Clement et al. [28]. Marine ISCCP, ERSST, OAFlux and ERA-40 data are used.

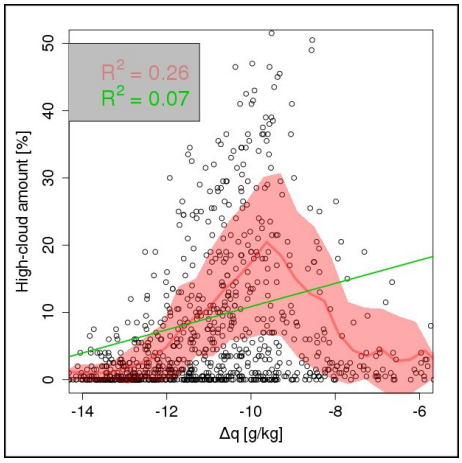

Figure 3.3: Scatter plot of marine ISCCP high-level cloud amount (C) versus ERA-40 Δq (black points). Only randomly selected 2% of the points over the East Pacific region during 1985-2001 is plotted. The red line represents C composited on Δq ($C_{\Delta \mathrm{q}}$, average of monthly composites). Shaded area represents the standard deviation of the monthly composites. A least-squares regression line (green) and coefficients of determination (R^2) are also shown.

(first row), but in one case (Δq) they differ strongly. The main distinction between the Clement et al.'s [28] and EFCs methods stems from the fact that this latter takes also into account the spatial co-variation between the two quantities. This co-variation can be nonlinear, as shown in Fig. 3.3. In the example, only 7% of the total variation in the cloud cover can be explained by the linear relationship between Δq and C, but the variance explained increases when a nonlinear fitting function is considered. This latter function is given by $C_{\Delta \mathrm{q}}$ and leads to a higher correlation when weighted by $\delta P_{\Delta \mathrm{q}}$ (Δq-EFC).

3.4.1 Caution in the interpretation of the EFCs

The γ-EFCs are meaningful only when the scatter plot variable C against the environmental factor γ indicates a clear dependence in space and in time. This point is illustrated by scatter plots of monthly SRB-derived CRE versus various γ factors for the EP region (Fig. 3.4). For instance, Fig. 3.4b4 shows that $\mathrm{SWCRE}_{\mathrm{SLP}}$ is almost independent of SLP, given the statistical error bounds. As a consequence, it is not possible to predict changes in SWCRE from SLP variations alone. When less than 10% of the total variation in C is described by C_γ (measured by the coefficient of determination: $R^2 < 0.1$), the relationships in Tab. 3.2 are reported in italics. For these cases, the value of the slope of the regression between $\overline{\delta C}$ and γ-EFCs are always very small (less than 0.2, second rows in Tab. 3.2). This is due to the fact that C_γ is almost flat (compare Figs. 3.4a5-b4-b5-a9-b9 with related second rows in Tab. 3.2). As a consequence, $\int_\gamma \delta P_\gamma C_\gamma \, d\gamma$ (EFC) is close to zero. In these situations the EFCs method only indicates that the space-time correlation between C and γ is too weak to give meaningful predictions.

3.4.2 Interannual variability

Tab. 3.2 is similar to the first two rows of Tab. 3.1, but for a larger number of cloud-related variables. The CREs derived from two radiative data sets (SRB and ISCCP-FD) do not exhibit marked differences. In the EP region, SST- and q-EFCs give the largest contribution to the cloud changes ($\overline{\delta C}$), whereas SLP is the most important factor in the WP region (second rows of Tab. 3.2). SST and SLP changes are striking features of the ENSO variability in the respective tropical Pacific areas. It does not surprise that the change of their PDFs often describes more than half of $\overline{\delta C}$. These relationships give a measure of the contribution of ENSO to the observed anomalies of the radiative balance at the TOA, since the interannual variability is primarily driven by ENSO [40, 68].

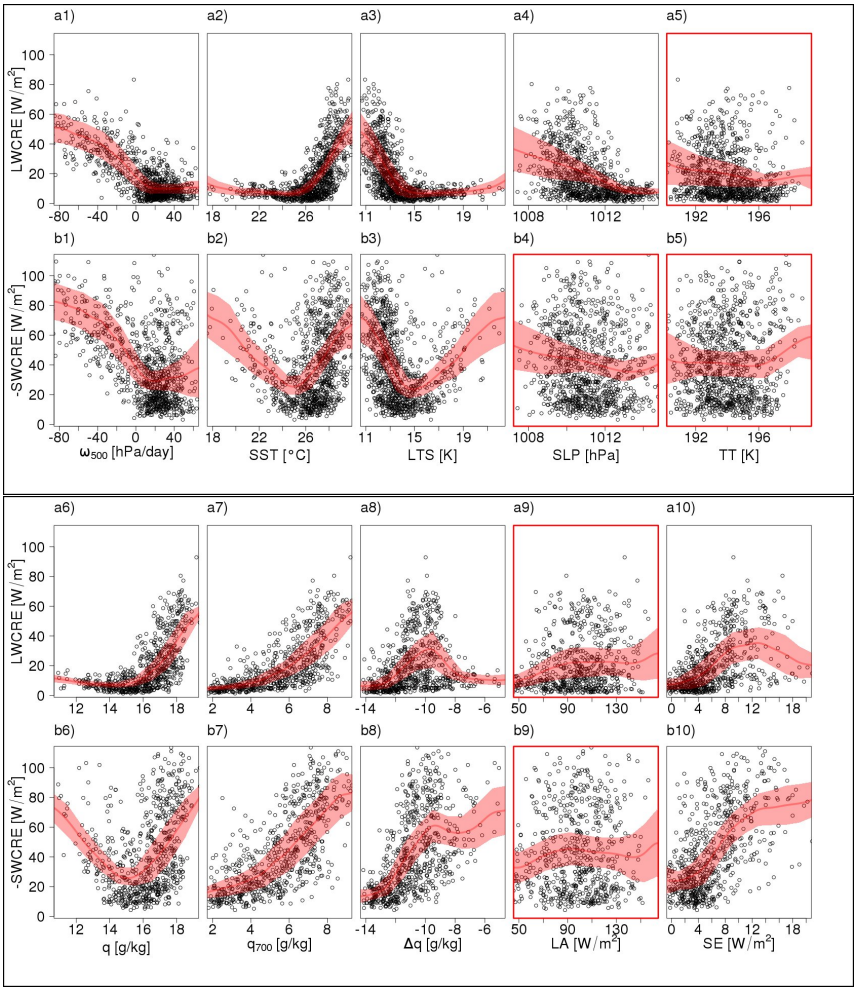

Figure 3.4: Scatter plots of monthly longwave (a) and shortwave (multiplied by -1) (b) CRE (C) versus various environmental factors (γ). Only randomly selected 2% of the points over the East Pacific Ocean (7.5 °N - 7.5 °S, 200 °E - 280 °E) during 1985-2001 is plotted. The red lines represent C composited on γ (C_γ). Shaded areas show the standard deviation of the monthly composites. When C_γ explains less than 10% of the C variance, the panels are bordered in red. SRB, ERSST, ERA-40 and OAFlux data are used.

	γ Environmental Forcing Components (EFCs)										
$\overline{\delta C}$	ω_{500}	SST	LTS	SLP	TT	q	q_{700}	Δq	LA	SE	A_t
						East Pacific Ocean					
SRB	**-0.91**	**0.94**	**-0.49**	**-0.78**	*-0.37*	**0.89**	**0.77**	**0.72**	***0.86***	**0.73**	**0.70**
LWCRE	**0.52**	**0.91**	**0.28**	**0.39**	*0.07*	**0.85**	**0.76**	**0.23**	***0.12***	**0.22**	**0.28**
ISCCP-FD	**-0.92**	**0.91**	**-0.43**	**-0.72**	*-0.34*	**0.90**	**0.81**	**0.78**	***0.85***	**0.82**	**0.66**
LWCRE	**0.43**	**0.78**	**0.20**	**0.34**	*0.08*	**0.79**	**0.70**	**0.19**	***0.09***	**0.18**	**0.19**
SRB	**-0.69**	**0.70**	-0.03	***-0.54***	*-0.21*	**0.71**	**0.58**	0.35	***0.50***	**0.62**	**0.79**
-SWCRE	**0.77**	**0.86**	-0.02	***0.20***	*0.04*	**0.94**	**1.22**	0.34	***0.06***	**0.50**	**0.95**
ISCCP-FD	**-0.67**	**0.74**	-0.02	***-0.62***	*-0.10*	**0.74**	**0.55**	0.22	*0.14*	**0.62**	**0.84**
-SWCRE	**0.52**	**0.55**	-0.01	***0.07***	*-0.02*	**0.68**	**0.87**	0.17	*0.00*	**0.36**	**0.72**
SRB	**0.91**	**-0.91**	**0.72**	**0.78**	*0.33*	**-0.85**	**-0.70**	**-0.82**	***-0.92***	***-0.93***	**-0.50**
N	**0.29**	**0.79**	**0.33**	**0.47**	*0.11*	**0.75**	**0.34**	**0.17**	***0.15***	***0.13***	**0.03**
ISCCP-FD	**0.91**	**-0.84**	**0.65**	**0.70**	*0.32*	**-0.80**	**-0.74**	**-0.80**	***-0.88***	***-0.91***	**-0.48**
N	**0.32**	**0.80**	**0.31**	**0.49**	*0.13*	**0.80**	**0.41**	**0.17**	***0.14***	***0.14***	**0.03**
Low-cloud	*0.25*	**-0.45**	**0.42**	0.32	*0.42*	**-0.60**	*-0.09*	-0.14	***-0.46***	-0.12	
amount	*0.02*	**0.19**	**0.12**	0.14	*0.13*	**0.28**	*0.02*	-0.05	***0.04***	-0.02	
Mid-cloud	**-0.84**	**0.84**	-0.45	**-0.62**	*-0.30*	**0.82**	**0.75**	**0.47**	***0.83***	**0.63**	
amount	**0.48**	**0.72**	0.29	**0.37**	*0.08*	**0.77**	**1.01**	**0.26**	***0.09***	**0.27**	
High-cloud	**-0.91**	**0.95**	**-0.52**	**-0.78**	*-0.30*	**0.90**	**0.75**	**0.63**	***0.85***	**0.68**	
amount	**0.56**	**0.94**	**0.32**	**0.42**	*0.04*	**0.89**	**0.86**	**0.23**	***0.13***	**0.23**	
						West Pacific Ocean					
SRB	**-0.75**	-0.18	**-0.68**	**-0.76**	*-0.50*	-0.20	-0.05	0.17	***-0.81***	-0.02	**0.96**
LWCRE	**0.23**	0.04	**0.29**	**0.53**	*0.13*	-0.09	-0.04	0.08	***0.02***	0.01	**0.78**
ISCCP-FD	**-0.78**	-0.17	**-0.65**	**-0.72**	*-0.51*	-0.13	-0.02	0.18	***-0.82***	-0.02	**0.94**
LWCRE	**0.20**	0.03	**0.20**	**0.46**	*0.17*	-0.05	0.01	0.07	***0.02***	0.01	**0.68**
SRB	**-0.87**	*0.23*	**-0.67**	**-0.72**	*-0.44*	0.20	0.41	**0.50**	***-0.64***	0.42	**0.72**
-SWCRE	**0.43**	*0.06*	**0.41**	**0.62**	*0.12*	0.12	0.55	**0.49**	***0.02***	0.33	**0.95**
ISCCP-FD	**-0.80**	*-0.23*	**-0.66**	**-0.65**	*-0.41*	0.06	0.13	0.17	*-0.06*	-0.09	**0.91**
-SWCRE	**0.39**	*0.04*	**0.31**	**0.56**	*0.20*	0.04	0.16	0.14	*0.00*	0.06	**1.18**
SRB	***0.63***	*0.05*	**0.56**	**0.55**	*0.47*	*0.48*	***0.73***	***0.62***	***0.72***	***0.60***	-0.08
N	***0.02***	*0.00*	**0.04**	**0.15**	*0.06*	*-0.04*	***0.15***	***0.13***	***0.01***	***0.05***	0.00
ISCCP-FD	***0.79***	0.04	**0.63**	**0.70**	*0.54*	*0.22*	***0.61***	*-0.44*	***0.61***	*0.35*	**-0.84**
N	***0.04***	0.00	**0.09**	**0.25**	*0.07*	*-0.03*	***0.05***	*0.06*	***0.02***	*0.02*	**0.10**
Low-cloud	*0.29*	**-0.57**	0.26	**0.43**	*0.38*	*-0.38*	**-0.57**	***-0.54***	*-0.46*	*-0.46*	**-0.60**
amount	*0.01*	**0.14**	0.08	**0.16**	*-0.04*	*0.07*	**0.18**	***0.08***	*-0.04*	*-0.04*	**0.09**
Mid-cloud	**-0.89**	*0.47*	**-0.80**	**-0.88**	*-0.44*	*0.26*	**0.53**	**0.55**	*0.04*	*0.04*	**0.54**
amount	**0.25**	*0.06*	**0.34**	**0.48**	*0.12*	*0.06*	**0.47**	**0.43**	*-0.01*	*-0.01*	**0.24**
High-cloud	**-0.78**	-0.10	**-0.65**	**-0.70**	*-0.16*	-0.18	-0.09	0.07	***-0.61***	-0.02	
amount	**0.29**	0.03	**0.38**	**0.55**	*0.02*	-0.10	-0.09	0.05	***0.06***	-0.01	

Table 3.2

Table 3.2: As in Tab. 3.1, but for a larger number of cloud-related variables and for the East (7.5 °N - 7.5 °S, 200 °E - 280 °E) and West (10 °N - 5 °S, 100 °E - 170 °E) Pacific Ocean. CREs are derived from SRB and ISCCP-FD data. Marine ISCCP total (A_t), adjusted low-level, mid-level and high-level cloud amounts are considered. Note that the values in row "High-cloud amount" for the East Pacific Ocean are copied from the first two rows of Tab. 3.1. When the mean composite C_γ describes less than 10% of the C variance, the values are reported in italics (see section 3.4.1).

During the positive phase of ENSO the EP region experiences an SST increase, which is associated with the reduction of low-level clouds and the increase of high and middle clouds [e.g. 114]. Warmer SSTs favor the transition between a stratiform deck of low-clouds to scattered clouds [25, 125, 171]. Warmer SSTs are associated with a weaker atmospheric stability, measured by weaker LTS and stronger upward motion. Enhanced convective activity breaks up the stratocumulus and lower LTS values are indicative of an MBL that is less effective in trapping moisture. Therefore, the low-cloud amount reduces in response to changes in these meteorological parameters. The sign of the correlation between SST-, LTS- and SLP-EFCs with low-clouds is consistent with this mechanism. On the other hand, weaker atmospheric stability favors more upper-level clouds. Indeed, the correlations between high, mid and the aforementioned meteorological parameters change sign accordingly. In contrast to the EP region, the WP area experiences a weakening of the convective activity, consistent with the tendency of the upward branch of the Walker circulation to move eastward during El Niño. As a result, SLP and ω_{500} increase and high and mid clouds reduce. Indeed, SLP-EFC and ω_{500}-EFC are anti-correlated with the upper-cloud anomalies, but the former contributes more to $\overline{\delta C}$ than the latter. During ENSO the radiative fluxes at TOA change all over the tropical Pacific Ocean, consistently with the CRE anomalies [e.g. 45]. Changes in the cloud type and amount influence the CREs [131], which indeed correlate significantly with the aforementioned environmental factors. These mechanisms have been widely recognized by observations and simulations [e.g. 183, 191]. Park and Leovy [213] noticed a negative correlation between the local SST anomaly and the change in low-cloud amount which occurs during El Niño, particularly strong along the eastern Pacific. SST-EFCs indicate the same but it also shows that the SST changes contribute to one fifth of the low-cloud interannual variability. Moreover, SST-EFCs track more than three fourth of the high-level cloud cover changes in the EP region. The strong dependence of these cloud types with the temperature is consistent with Kiehl [225], but here we also assess to what extent SST contributes to the cloudiness anomalies. Note that humid-

ity and SST variations are highly coupled, especially at the surface. Warm SSTs favor convection and lead to a moister atmosphere, which promotes more cloudiness. As a result both are similarly related to C. Conversely, SST- and q-EFCs are very small in the WP region (Tab. 3.2, second rows), owing to the very weak interannual variation of SST.

An important role is also played by the total cloud fraction (A_t), whose EFCs often describe more than two thirds of $\overline{\delta \mathrm{LWCRE}}$ and $\overline{\delta \mathrm{SWCRE}}$. It is not the case of $\overline{\delta \mathrm{N}}$, the ratio of SW to LW CREs, for which the A_t-EFC contribution is almost zero. The invariance of N to the cloud cover is consistent with Kiehl [225]. Moreover, Cess et al. [46] argued that much of the interannual variability of N is related to the interannual variability of tropopause temperature (TT) in the Pacific warm pool. The values reported in italics in Tab. 3.2 for the WP region indicate that there is no space-time correlation between the two fields. In this case, the EFCs method cannot be used to calculate the relationships in Tab. 3.2 (see section 3.4.1). However, when simply correlating in time N and TT, no significant interannual correlation is found. The origin for this discrepancy with Cess et al.'s results [46] will be discussed in the next section. The N-TT relationship is also shown for the EP region, an area which is not characterized by deep convective clouds and where this relationship is not expected to be statistically significant. However, for the sake of completeness our results are shown for this region as well.

In the WP region, ω_{500}-EFC does not describe much of the variations in N between 1985 and 2001, which is in agreement with Yuan et al. [114], but our analysis indicates this result is also valid for the other cloud-related quantities investigated here. Although the ω_{500}-EFC is often very well correlated with $\overline{\delta C}$, it often contributes to less than half of the interannual variability in C in these areas. This stems from the fact that the PDF of ω_{500} does not change much at the interannual scale and that considering ω only at 500 hPa does not capture fully the variability of the ω profile associated with cloud changes [115].

The heat fluxes have been observed to play a role in the evolution of the clouds [e.g. 33]. The SE-EFCs in Tab. 3.2 are well correlated to cloud variations in the EP region and describe a sizeable amount of $\overline{\delta C}$, especially when SWCRE is considered. On the other hand, the space-time correlation between LA and C is very weak, as highlighted by the values in italics in Tab. 3.2. As described in section 3.4.1, when the space-time correlation is not strong, the EFCs method cannot be used to calculate the relationships in Tab. 3.2. Heat fluxes are primarily driven by SST and surface winds. Indeed SE-EFCs covariate with $\overline{\delta C}$ with the same sign of SST-EFCs (first rows in Tab. 3.2). Regarding the other EFCs, most of them are not statistically significant, so they have not been considered in our analysis.

In conclusion, we have shown that the results found in this novel framework of analysis can be related to previous studies and illustrated the validity of the technique. The methodology proposed here allows to quantify the contribution of the regional meteorological conditions to the observed cloud property changes. In addition, the contribution of the EFCs to $\overline{\delta C}$ takes into account the spatial and possible nonlinear dependence between C and γ. These features make the EFCs technique unique and different with respect to other previous methodologies, such as those shown in Clement et al. [28] and in Bony et al. [200].

3.5 Discussion on the relationship between the tropopause temperature and N

[225] argued that the near cancellation between the LW and the SW CREs, i.e. $N \approx 1$, in the tropical deep convective regions is dominated by the tropical tropopause height. If it is the case, the interannual variability of TT should control the interannual variability of N. In the previous section we found that the space-time relationship between TT and N is very weak. When spatially and yearly averaged marine N is correlated with TT in the Pacific Warm pool [5 °N - 5 °S, 140 °E - 165 °E; (PW)], the same region selected by Cess et al. [46], the interannual correlation is not statistically significant as well. This seems in contrast with Cess et al.'s findings [46]. The correlation coefficient ranges from 0.4 to 0.5 for SRB and ISCCP-FD data, respectively, which is consistent with the "null" hypothesis of no relationship ($\rho = 0$) in both the data sets at the confidence level $\alpha \leq 5\%$. The same relationship increases when a smaller sample in time is considered. When only the five years from 1985 to 1989 are taken into account, as in Cess et al. [46], this relationship is high: the correlation coefficient ranges between 0.8 and 0.7 for ISCCP-FD and SRB data, respectively (Fig. 3.5a). In addition, Cess et al. [46] admitted that the correlation they found cannot explain the anomalous value of N for the year 1998, for which TT does not appreciably differ from the climatological mean. The fact that N should be related to TT is based on the key assumption that the CRE in the PW region is controlled by just one cloud type (cirrostratus). Conversely, the CRE arises from the averaged contribution of different cloud types [134], whose tops are not necessarily near the tropopause. Indeed, interannual changes in the cloud types match fairly well the changes in N in Fig. 3.5b.

The fraction of high-clouds is anomalously low in 1998 and is partly compensated by an unusual occurrence of low-clouds. This may be the result of the influence of the atmospheric dynamics on the cloudiness. However, we showed in Tab. 3.2 that the ω_{500}-EFC does not capture much of the N

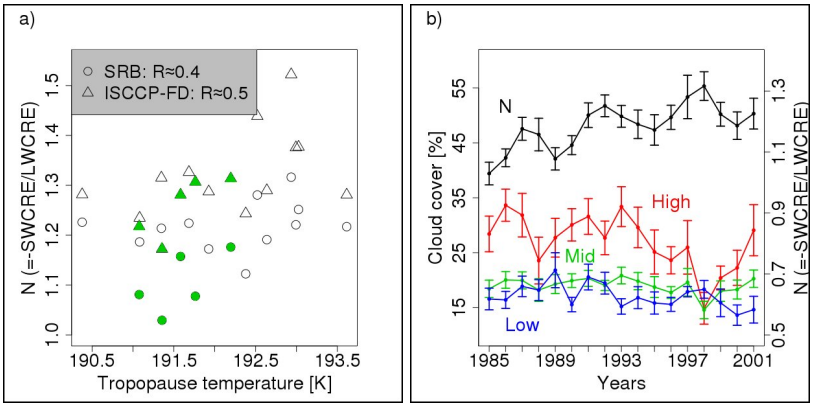

Figure 3.5: Annual mean values of meteorological quantities are averaged over the Pacific Warm pool (5 °N - 5 °S, 140 °E - 165 °E). a) Scatter plot of marine N versus tropopause temperature. The years from 1985 to 1989, the same period analyzed in Cess et al. [46], are highlighted in green. b) Time series of marine ISCCP high-level, mid-level and adjusted low-level cloud cover and SRB N. Error bars are 95% ranges of monthly variability.

anomalies, symptomatic of the weak climatological relationship between ω_{500} and N. Allan et al. [174] argued that changes in N and in the cloud types cannot be explained solely by changes in the large-scale dynamics, but can be related to tropics-wide long-term changes in the spatial-mean cloud forcing. Fig. 3.5b shows the tendency of N to increase on the decadal scale. Hartmann et al. [134] explained the near cancellation between the LW and the SW CREs with an alternative hypothesis. They argued that the net radiation at TOA in convective areas is required to be close to that of nonconvective areas by complex feedback processes. These feedbacks arise from the sensitivity of the tropical circulation to SST gradients and the sensitivity of the cloud albedo to the vertical motion. The interaction between convective and subsiding regions, through the large-scale circulation, controls the value of N for tropical convective clouds. Including these feedbacks in a simple model, Hartmann et al. [134] showed that the net radiation in convective areas approaches that in adjacent nonconvective areas, almost independently of the mean-cloud top temperature assumed for the convective clouds.

A deeper discussion on this topic lies outside the scope of this paper, which is intended to show an alternative method to relate cloud properties to environmental conditions. However, we showed the topic is still an open question and is potentially tied to remote-controlling factors as well as linked to long-term climate oscillations. We conclude the interannual variability of N does not (strongly) depend on the interannual variability of TT, but is

controlled, to a first approximation, by the different cloud types present over the tropical warm pool.

3.6 The seasonal cycle of low-level clouds

The applicability of the environmental forcing components (EFCs) method is now shown on a different time-scale. Since subtropical stratocumulus exhibit a strong seasonal cycle, it is interesting to explore this variability from the novel perspective of the EFCs. The seasonal cycle of the low-clouds is analysed in the Californian region (20 °N - 30 °N, 120 °W - 130 °W), following Klein and Hartmann [7]. They noticed that the season of maximum stratocumulus cover, i.e. of maximum low-level cloudiness, corresponds to the season of greatest lower-tropospheric stability (LTS) or of estimated inversion strength (EIS). This latter is a more refined measure of LTS and is a more regime-independent predictor of stratus cloud amount than LTS, according to Wood and Bretherton [194]. The scatterplot of low-level cloudiness versus LTS or EIS, averaged over a more extended range of years (1985-2001), leads to the same result (Fig. 3.6): maximum low-cloud amount during the JJA season coincides with the maximum mean values of LTS or EIS in the Californian region. However, these relationships change if, instead of regional mean values, the values for each of the 25 grid points off the California coast for each season are considered (Fig. 3.6). It suggests that the relationship between low-cloud cover and LTS (EIS) depends on the season. The slope of the correlation changes from season to season and the same local LTS (EIS) value is associated with different cloud fractions in different seasons. For instance, the cloudiness correlates negatively to LTS (EIS) during the DJF season, which is opposite with respect to the sign of the correlation for the overall seasonal cycle. Similar results are found for other subtropical stratocumulus regions (not shown). We conclude that on the seasonal time scale, the low-cloud amount scales linearly with LTS (EIS), in accord to Klein and Hartmann [7] and to Wood and Bretherton [194]; whereas the co-variation in space, within a season, is different and depends on the season.

We also note that EIS has a much smaller seasonal variation than LTS and, at least off the coast of California, it is not a more effective predictor of low-cloud cover than LTS. A considerable range of low-cloud amount is found for a given value of EIS. For instance, for EIS = 4K the cloudiness ranges from 30 to more than 70 % (Fig. 3.6b). To some extent, the nonlinear relationship between LTS and low-cloud amount (for brevity referred to as C here) can be described by the nonlinear function given by C composited with respect to LTS (C_{LTS}, purple line in Fig. 3.6a). C_{LTS} can be used to calculate the EFCs and to investigate the cloud variability with the EFCs

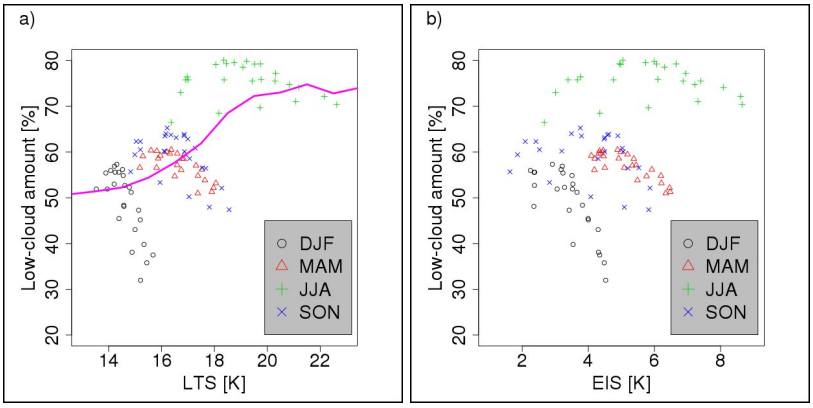

Figure 3.6: Scatter plot of seasonally averaged adjusted low-level cloud amount (C) versus LTS (a) and EIS (b) for the 25 grid points in the Californian region (20 °N - 30 °N, 120 °W - 130 °W) stratified by season. ERA-40, ERSST, ISCCP data are used for the period 1985-2001. The purple line in (a) represents C composited on LTS (C_{LTS}, average of monthly composites).

method.

We now quantify to what extent the two indicators of the MBL inversion strength (LTS and EIS) and other meteorological variables are able to describe the observed low-cloud fraction seasonal cycle. We address this question using the EFCs in a similar approach as for the interannual variability in the previous sections. In this case the mean-state P_γ and C_γ are given by the annual mean of monthly P_γ^m and C_γ^m for each year between 1985 and 2001. Then, the mean-state P_γ of a specific year is subtracted from each of the 4 seasonal γ-PDFs (3-mo mean of monthly P_γ^m for each season) of the same year, to get the seasonal anomaly δP_γ. The integral of δP_γ C_γ is referred to as γ-EFC. The EFCs are then correlated to $\overline{\delta C}$, which now represents the spatially and seasonally averaged low-cloud cover of a specific year (1985 to 2001) when the annual mean is removed. The results could be shown in a table structured as Tab. 3.2, but, for display purpose, they are shown in a plot similar to a Taylor diagram. In Fig. 3.7 the radial axis denotes the slope of the linear regression between each EFC and $\overline{\delta C}$ and the azimuthal axis the correlation coefficient between these two signals. Perfect agreement corresponds to a point at correlation ± 1 and regression coefficient one.

Fig. 3.7 shows that the role of LTS is dominant in the seasonal low cloudiness variability compared to other meteorological quantities (compare regression coefficients). LTS and EIS are proxies of the temperature stratification in the lower troposphere, which influences both the surface fluxes and the entrainment of warm and dry free-tropospheric air into the cloudy

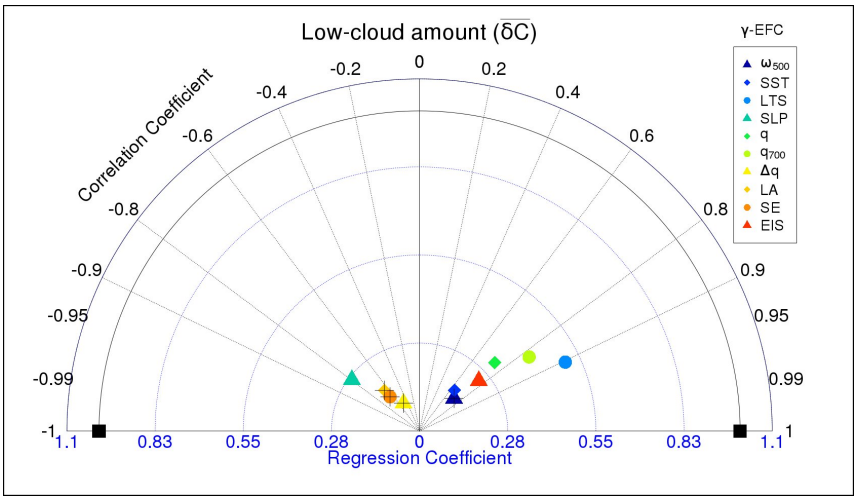

Figure 3.7: "Taylor" diagram showing the relationship between seasonally averaged adjusted low-level cloud amount ($\overline{\delta C}$, annual mean removed) and the contribution of γ-EFC for the different environmental factors indicated in the legend. The relationship is characterized in terms of correlation and slope of the regression between the two signals, as in Tab. 3.2, but for the Californian region (20 °N - 30 °N, 120 °W - 130 °W). ERA-40, ERSST, ISCCP and OAFlux data are used for the period 1985-2001. When the annual mean composite C_γ describes less than 10% of the C variation, a cross overlaps the points (see section 3.4.1).

MBL, that both play a role in the stratocumulus evolution [206]. Although EIS-EFC is very well correlated with the low-clouds (correlation coefficient $\rho \approx 0.8$), it describes not much of the seasonal variability (regression coefficient less than 0.3). This is mainly due to the much smaller seasonal variation of EIS relative to that of LTS (Fig. 3.6). The main difference between these two proxies stems from the fact that the former does not include variations of the free-tropospheric temperature, which has a significant seasonal cycle off the coast of California (see Lin et al. [243] for a discussion on that matter).

A crucial first step in the transition between a deck of stratiform low-clouds to scattered cumulus is the decoupling. This defines a situation where the MBL is decoupled into two turbulent layers, which implies significant differentiation between the cloud and subcloud thermodynamic properties. As a consequence, the transport of moisture-laden parcels toward the cloud base is inhibited. Decoupling is often driven by the increase of SST [206], which leads to a reduction of the temperature inversion between the MBL and the free-troposphere and an increase of the entrainment rate of warm, dry air from above the inversion into the cloud layer. The reduction of moisture

provided from the surface, together with more entrainment and the deepening of the MBL, are fundamental mechanisms leading to a reduction of the cloud cover. Therefore, warmer SSTs should favor less stratocumulus-like conditions. However, Klein and Hartmann [7] have found that, off the California coasts, SSTs are seasonally not anti-correlated with the low-cloud amount. They showed that 700 hPa temperature has a larger seasonal variability than SST, hence the former is more important than the latter in determining LTS in this region. Consistently, SST-EFC correlates positively with the low-cloud anomalies and LTS-EFC correlation and regression coefficients are larger than SST-EFC correlation and regression coefficients (Fig. 3.7). Using a mixed-layer model, Bretherton and Wyant [206] showed that the surface latent heat fluxes increase during decoupling processes, but in Fig. 3.7 the LA-EFC does not describe much of the changes of the seasonal low-cloud amount in the Californian region, although it is highly correlated to it ($\rho \approx -0.7$). It is also true that decoupling does not immediately lead to a drop in stratocumulus cloud amount [171] and the mixed-layer theory does not hold in cases of shallow convection regimes. However, since no space-time correlation can be found between LA, SE and $\overline{\delta C}$, as highlighted by the black cross points in Fig. 3.7, the relationships found using the EFCs method need to be interpreted with caution (see section 3.4.1).

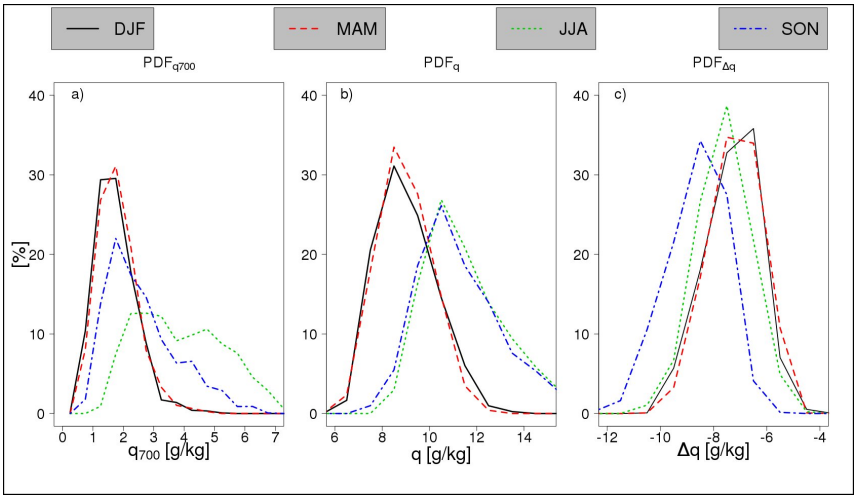

Figure 3.8: Seasonal PDFs of q_{700} (a), of q (b) and of Δq (c), expressed in percentages. ERA-40 reanalysis data are used for the period 1985-2001 in the Californian region (20 °N - 30 °N, 120 °W - 130 °W).

Regarding the humidity field, Fig. 3.7 shows that q_{700}- and, to a lesser extent, q-EFCs contribute to a sizeable part of $\overline{\delta C}$. The moistening of the

MBL favors more condensation and hence cloudiness, all things being equal. The humidification of the free-troposphere can have two opposing effects, as explained in Sandu et al. [95]. An increase of moisture above the boundary layer reduces the drying effect of the entrained air into the cloud layer, which would promote more cloud cover. On the other hand, more water vapor in the free-troposphere enhances the downwelling longwave radiation, which reduces the radiative cooling at cloud top. As a consequence, the production of turbulence in the MBL is reduced and this would favor more decoupling-like conditions. The high values of the correlation and regression coefficients between q_{700}-EFC and $\overline{\delta C}$ as compared to the other environmental factors, reveal that the humidification of the free-troposphere plays an important role in controlling the low-cloud amount variability. Fig. 3.8a shows that the largest values of q_{700} occur during JJA, which coincides with the season of the largest low-cloud cover (Fig. 3.6). Therefore, the net effect of the free-tropospheric moistening seems to promote more stratocumulus-like conditions. Finally, we also note that Δq contributes less to $\overline{\delta C}$ than q and q_{700} separately. The reason for that is shown in Fig. 3.8. q exhibits the maximum from June to November and the minimum from December to May. q_{700} peaks only during JJA, the season of maximum cloudiness (Fig. 3.6). As a result, q_{700}-EFC tracks the low-cloud amount anomalies better than q-EFC (Fig. 3.7). When q and q_{700} are combined into Δq, this latter peaks during SON, which does not coincide with the season of maximum cloudiness. Because of this, q and q_{700} separately correlate better with the low-cloud cover than Δq.

In conclusion, although LTS and, to a lesser extent, q_{700} are the best predictors of low-cloud amount in the Californian region, we stress that none of the EFCs alone can describe the seasonal cycle of the low-level cloudiness fully. This imply that the interaction of multiple meteorological parameters plays a role.

3.7 Summary and discussion

Different environmental factors were evaluated in order to quantify their effect on interannual and seasonal variation in clouds and their radiative impact. For this purpose an extension of the Bony et al.'s method [200] is applied using different meteorological variables as a proxy instead of ω_{500}. Various cloud properties exhibit consistent relationships with LTS, SLP, humidity fields and other environmental factors determined on a local basis in different studies, such as [7, 28, 90] and others. These relationships can be combined with the changes in the PDF of the respective proxy (EFC) to assess its main impact. This novel approach has been explored throughout the paper, showing its

validity and advantages at different time-scales.

In this analysis framework the effect of the large-scale vertical velocity on CRE and cloud amount interannual variability is smaller than the SST effect, at least in the eastern equatorial Pacific. The changes of the PDFs of the humidity at surface and SST in the eastern equatorial Pacific and SLP in the western side capture most of the interannual variability of CREs and cloud cover. Since SST and SLP changes are striking features of the ENSO variability in the respective tropical Pacific areas, these relationships give a measure of the contribution of ENSO to the observed anomalies of the tropical cloudiness and radiative balance at the TOA. Furthermore, some of the properties of N (=-SWCRE/LWCRE) have been analysed. It is invariant to the cloud cover, consistent with Kiehl [225], and to the tropopause temperature changes, which seems to be in contrast with Cess et al. [46]. The contrast arises because their analyses consider a too short period and N is assumed to be controlled by just one (high) cloud type, while it arises from the averaged contribution of different cloud types [e.g. 134], whose tops are not necessarily near the tropopause.

Moreover, the seasonal cycle of the low-clouds has been evaluated with the aim of understanding the factors responsible for the presence of these clouds in specific subtropical locations, where marine stratocumulus are dominant. We conclude that in time (seasonally), the low-cloud amount scales linearly with LTS and EIS, in accord to Klein and Hartmann [7] and to Wood and Bretherton [194]; whereas the co-variation in space, within a season, is different and depends on the season.

In the Californian area the seasonal cycle of the low-clouds has been assessed from the original perspective of the EFCs method. We find that the role of LTS and, to a lesser extent, of the humidity field is dominant in the seasonal cycle of the low-clouds compared to other environmental factors. An additional result is that LTS is a more effective predictor of the low-cloud amount than EIS off coasts of California. This is mainly due to the larger seasonal variation of the former relative to that of the latter. Surprisingly, the specific humidity in the MBL and in the free-troposphere combined are a less effective predictor of low-cloud cover than the same quantities considered separately. However, since none of the analysed environmental conditions can fully account for the seasonal low-cloud amount evolution, the interaction of multiple meteorological parameters plays a role.

From a parameterization perspective, cloud properties must be represented in terms of environmental conditions computed by GCMs at each time step [116]. Thus, models should be able to accurately represent the relationships between meteorological parameters and cloud-related variables. Assessing the model performance in the framework of the EFCs might shed

light on the origin of differences in cloud fields between models and observations and allows to relate these discrepancies to specific aspects of the physical parameterizations used in the models. The GCMs can be ranked according to the sign of the simulated correlation coefficient compared to the observations, as in Clement et al. [28], and whether they can faithfully replicate to what extent an environmental parameter contributes to the observed cloud changes (EFC). In this sense, the method shown may be used as a more constraining test to assess GCMs' cloud performance with respect to Clement et al. [28]. In addition, a striking feature of the novel methodology proposed in this study is the fact that it takes into account the spatial distribution and possible nonlinear relationships between cloud changes and environmental conditions. These relationships can be synthesized in a single plot (Fig. 3.7), that can be used as a simple tool for cloud modeling evaluation.

Finally, the few variables analysed do not represent all possible meteorological conditions which influence the development and properties of the clouds. Other factors, such as the vertical wind shear, the temperature lapse rate, the aerosol effects, entrainment rate, drizzle, vertical distribution of radiative cooling in the cloud may also influence the cloud properties. The combined effect is difficult to quantify from observations alone. High resolution numerical simulations may aid to further explore and assess the role of these factors.

Acknowledgments

The research leading to these results has received funding from the European Union's Seventh Framework Program (FP7/2007-2013) under grant agreement n° 244067.
The authors thank Eveline van der Linden and the three anonymous reviewers for their constructive comments that have helped the improvement of this paper. SRB data were obtained from the National Aeronautics and Space Administration (NASA) Langley Research Center Atmospheric Science Data Center (ASDC).

Chapter 4

Evaluation of clouds and radiative fluxes in the EC-Earth general circulation model

Observations, mostly from the International Satellite Cloud Climatology (ISCCP), are used to assess clouds and radiative fluxes in the EC-Earth general circulation model, when forced by prescribed observed sea surface temperatures. An ISCCP instrument simulator is employed to consistently compare model outputs with satellite observations. The use of a satellite simulator is shown to be imperative for model evaluation. EC-Earth exhibits the largest cloud biases in the tropics. It generally underestimates the total cloud cover but overestimates the optically thick clouds, with the net result that clouds exert an overly strong cooling effect in the model. Every cloud type has its own source of bias. The magnitude of the cooling due to the shortwave cloud radiative effect (|SWCRE|) is underestimated for the stratiform low-clouds, because the model simulates too few of them. In contrast, |SWCRE| is overestimated for trade wind cumulus clouds, because in the model these are too thick. The clouds in the deep convection regions also lead to overestimate the |SWCRE|. These clouds are generally too thick and there are too few mid and high thin clouds. These biases are consistent with the positive precipitation bias and the overly strong mass flux for deep convective plumes. Potential sources for the various cloud biases in the model are discussed.

This chapter has been published as: *Lacagnina C. and F. Selten. Evaluation of clouds and radiative fluxes in the EC-Earth general circulation model. Climate Dynamics, in press, 2014.*

4.1 Introduction

Clouds strongly interact with the solar and thermal radiation [e.g. 74, 204]; changes in this interaction in response to an external perturbation are known as cloud feedbacks [e.g. 232]. These cloud feedbacks contribute to the earth's climate sensitivity. Despite the importance of clouds, their representation in general circulation models (GCMs) continues to account for much of the uncertainties in climate projections [43, 216, 235]. The global cloud feedback is positive in all models [107], but the spread associated with intermodel differences is roughly three times larger than that associated with the other main feedbacks [118].

The spread among the models in representing cloud feedbacks is present at all latitudes, but it tends to be larger in the tropics [113, 198], with a sizeable contribution from marine boundary layer (MBL) clouds [199]. An example of MBL clouds are the stratocumulus. These are stratiform low-clouds particularly persistent over the eastern basins of the subtropical oceans. The amount of this cloud type is usually underpredicted by the GCMs, even when the observed sea surface temperatures (SSTs) are prescribed [21]. Stratocumuli primarily contribute to the earth's radiation budget by enhancing the surface albedo. The underprediction of these clouds can lead to positive SST biases of about 5 K in coupled GCMs [38]. The misrepresentation of the subgrid cloud structure affects the radiation budget [e.g. 16] and so model biases in clouds can stem either from their representation in the cloud scheme, the convective mixing scheme or the representation of their microphysics or a combination of any of those.

The interaction of the clouds with a wide range of climate processes critically depends on both the amount and type of cloud present [e.g. 131], which is intimately coupled to the large-scale atmospheric circulation [127, 169, 200] and to many other factors, such as sea surface temperature (SST) [201], lower-tropospheric stability (LTS) [7], sea level pressure (SLP), etc. [28, 31]. Understanding both how clouds may change in the future and, by implication, the whole climate system is still an open question [26]. Climate models represent invaluable tools for addressing this issue but, as mentioned above, GCMs still generally disagree in simulating clouds [2, 111]. A practical method to acquire greater confidence in cloud changes for future climate predictions is to assess the realism of the cloud simulation of present-day conditions. Williams et al. [129] have argued that at least part of the local cloud anomalies in the current variability can be attributed to the cloud response to climate change. Since global observation of clouds are only possible from space, satellite observations are a particularly relevant source of information to judge models in the current climate.

Data products from the International Satellite Cloud Climatology Project

(ISCCP) [246] provide retrievals of various cloud-related variables for a long period of time (1983 to present). We will mainly take advantage of this data set to evaluate cloud biases in the EC-Earth atmospheric GCM [242]. Because of the significant differences between the ways clouds are simulated and the ways they are observed, an ISCCP satellite simulator [8, 170] is employed. This approach allows a more consistent comparison between model clouds and the ISCCP products by using common definitions of clouds. Therefore, a satellite simulator is a convenient tool to evaluate models' performance.

The aim of this study is to investigate the capability of the EC-Earth model to faithfully reproduce the observed cloud radiative effects (CREs), cloud-related variables and precipitation in the recent decades, when it is forced by prescribed observed SST. Our main objective is to establish common features and highlight differences between model simulations and observations in terms of reproducing specific cloud regimes and the relationships between cloud properties and environmental conditions. The link between model biases and the parameterizations employed will also be discussed by identifying processes that either help or hinder the simulation of clouds. The model analyzed is an earth system model based on the integrated forecast system (IFS) of the European Centre for Medium-Range Weather Forecasts (ECMWF). The general strategy of employing a weather forecasting model for climate studies has been laid out by Hazeleger et al. [241]. The IFS model has been optimized for surface variables such as temperature and pressure, while EC-Earth, based on IFS, has been optimized for top-of-atmosphere (TOA) fluxes. Since misrepresentation of the cloud structure influences the energy budget of a climate model [22], it is therefore of particular interest to evaluate the cloud biases in EC-Earth.

A detailed evaluation of the cloud simulation is presented here, mainly focusing on the tropical belt where, as will be shown, the cloud biases tend to be the largest. The strategy is to investigate the model biases from the global to the regional spatial scale and from the multidecadal to the seasonal time scale. This will be accomplished by taking advantage of compositing techniques. In section 4.2 the model, the simulation, the observational data and the methods used to compare both are described. The cloud biases are assessed globally in section 4.3 and with more detail over the tropical belt in section 4.4. We also evaluate the ability of EC-Earth to reproduce the relationships between meteorological conditions and seasonal stratocumulus variability (section 4.5). Finally, in section 4.6 the results of the previous sections are summarized and possible directions on how to improve the representation of the cloud field in EC-Earth are discussed.

4.2 Data

4.2.1 Observations

We use monthly mean observations from different sources for the years 1984 to 2007, gridded at $2.5^\circ \times 2.5^\circ$ resolution.

Cloud properties are determined using the simulator-oriented ISCCP product [193] available at http://climserv.ipsl.polytechnique.fr/cfmip-obs/. This dataset contains cloud albedo, cloud amount, cloud-top pressure (P_c) and cloud optical depth (τ) retrieved from satellite measurements of infrared and visible radiances. Cloud amount is categorized into six τ bins ($\tau \leq 1.3$, $1.3 < \tau \leq 3.6$, $3.6 < \tau \leq 9.4$, $9.4 < \tau \leq 23$, $23 < \tau \leq 60$, and $60 < \tau$). Cloud amount is further categorized based on P_c (in hPa): high, middle and low clouds are defined as $P_c \leq 440$, $440 < P_c \leq 680$ and $P_c > 680$, respectively.

Two complementary sources of data, based on different sensors, are used to characterize the cloud microphysics properties.
First: MODIS [215] is a Moderate Resolution Imaging Spectrometer instrument aboard the Terra (EOS AM) and Aqua (EOS PM) sun-synchronous satellites. MODIS uses visible and near-infrared (VIS/NIR) radiances techniques to retrieve cloud properties and provides a wider range of observations than ISCCP, in particular the liquid water path (LWP) and the particle size of the cloud droplets. We use monthly averages of diurnal retrievals from both platforms combined.
Second: PATMOS-x [18] is a Pathfinder Atmosphere's Extended dataset based on the Advanced Very High Resolution Radiometer (AVHRR) located on the National Oceanic and Atmospheric Administration (NOAA) polar-orbiting satellites. Emissivity and P_c are retrieved using infrared channels. Effective particle radius and τ are obtained from solar channels and the cloud water path is derived from these.

Radiation budget quantities at TOA are retrieved from Global Energy and Water Cycle Experiment (GEWEX) Surface Radiation Budget (SRB) Release-3.0 data [121]. The same quantities are also obtained from Clouds and the Earth's Radiant Energy System (CERES) Energy Balanced and Filled (EBAF) TOA Ed2.7 [81], for the period 2001-2007. For SST we use the Extended Reconstructed Sea Surface Temperature (ERSST) data [164]. The precipitation field is documented with the Global Precipitation Climatology Project (GPCP) product [195] and the Tropical Rainfall Measuring Mission (TRMM) data product 3B43 [105]. GPCP gives a global overview of the earth precipitation budget, whereas TRMM documents earth precipitation mainly focused on the tropical belt, beginning in 1998.

ERA-Interim reanalysis of the ECMWF [15] are used to provide various

atmospheric variables: the specific humidity at surface (q) and just above the boundary layer at 700 hPa (q_{700}), the sea level pressure (SLP) and the potential temperature at 700 hPa. The combination of the latter with SST gives a measure of the marine LTS [7]. A refinement of LTS, known as estimated inversion strength (EIS), was proposed by Wood and Bretherton [194] and is calculated as follows:

$$EIS = LTS - (z_{700} - LCL)\Gamma_m^{850} \tag{4.1}$$

where Γ_m^{850} is the moist-adiabatic potential temperature gradient at 850 hPa, z_{700} is the height of the $p = 700$ hPa surface and LCL is the lifting condensation level. All these quantities are obtained from ERA-Interim data. Finally, the vertical pressure velocity field at 500 hPa (ω_{500}) is characterized using ERA-Interim reanalysis and NCEP-DOE reanalysis [154] products. The latent (LA) and sensible (SE) heat fluxes are taken from the Objectively Analyzed Air-Sea Fluxes (OAFlux) data [146].

4.2.2 Model and simulation description

This study uses the EC-Earth model version 2.3, which is based on cycle 31r1 of the ECMWF IFS model. It is coupled to an ocean GCM that is based on version 2 of the Nucleus for European Modeling of the Ocean (NEMO) [82]. The ocean/ice and atmosphere/land components communicate through the OASIS 3 coupler [219]. The atmosphere GCM is run at a horizontal spectral resolution of T159 (triangular truncation at wavenumber 159, roughly equivalent to 125 km) and has 62 levels in the vertical. The distance between levels increases gradually with height with typically about 20 levels to resolve the boundary layer. More information can be found at the website: http://ecEarth.knmi.nl.

Clouds are described by prognostic equations for cloud water content and cloud fraction and are distinguished in convective and stratiform clouds [167]. The parameterization of the former is based on the bulk mass flux approach [166], whereas the formation of the latter is based on nonconvective processes, such as large-scale lifting and/or diabatic cooling [30]. Tab. 4.1 provides a summary of the physical parameterizations used in the model, which are relevant to the cloud simulation.

EC-Earth was integrated for the period from 1984 to 2007 with prescribed observed SST and sea ice, supplied by the Atmospheric Model Intercomparison Project (AMIP). The atmospheric component of the coupled ocean-atmosphere model is used in isolation, such that the simulation can be considered an atmosphere-only experiment. This configuration follows the protocol of the Coupled Model Intercomparison Project (CMIP5) experiment #3.3[1].

[1] http://cmip-pcmdi.llnl.gov/cmip5/docs/Taylor_CMIP5_22Jan11_marked.pdf

Physical component	EC-EARTH cycle 31r1 [242]
Radiation	• Rapid Radiative Transfer Scheme (RRTM) for longwave radiation [102] • Shortwave radiation scheme [79]
Deep convection	Mass flux scheme [166] with convective available potential energy (CAPE) closure [234]
Shallow convection	Mass flux at cloud base estimated based on the moist static energy budget in the sub-cloud layer [166]
Mid-level convection	Activated if there is a large-scale ascent and a sufficiently moist layer. Mass flux at cloud base related to the large-scale vertical velocity [166]
Boundary layer and turbulence	Eddy diffusivity with different closures depending on the stability regimes and on the vertical location above the surface: • Eddy-diffusivity mass flux in the mixed layer [155, 184] • Revised version of the Louis scheme [148, 182] • Local diffusion with Monin-Obukhov functions [159]
Entrainment and Detrainment	• For the updraught: fixed values of turbulent entrainment/detrainment for shallow convection [230] and penetrative/mid-level convection [104]. Organized entrainment directly proportional to the large-scale moisture convergence. Organized detrainment estimated from the updraught kinetic energy [176] • For the downdraught: turbulent entrainment/detrainment set to a constant value. Organized entrainment tied to the vertical velocity in the downdraught [234]. Organized detrainment activated if either the downdraught becomes positively buoyant or reaches the surface.
Cloud microphysics and macrophysics	• Prognostic cloud fraction scheme [167] • Effective radius of the liquid water cloud particles based on Martin et al.'s parameterization [157] • Effective dimension of the ice water cloud particles diagnosed from temperature [34] • Distinction between liquid and ice phase made as a function of temperature • Conversion from cloud water/ice to rain/snow treated following Sundqvist [91] • Fallout of rain water/snow parametrized as in Kuo and Raymond [138] • Evaporation rate of convective rain below cloud base parametrized following Kessler [66]
Overlap	Maximum-random [117]

Table 4.1: Cloud-related physical parameterizations in EC-Earth.

Finally, the aerosol and CO_2 concentrations from observations were supplied by AMIP and included in the model. They interact with the radiation scheme, but aerosols do not interact with the cloud parameterizations, hence their indirect effects are not considered in this experiment.

For the first time, an ISCCP satellite simulator has been embedded in EC-Earth. The simulator used is part of the Cloud Feedback Model Intercomparison Project (CFMIP) Observation Simulator Package (COSP) version 1.3 (http://cfmip.metoffice.com/COSP.html). COSP [2] is a software tool that provides convenient means to mimic satellite retrievals, by using model outputs to define quantities actually observed, rather than inferred, from satellites (e.g. visible/infrared radiances). In this way, simulated clouds can be directly compared with the observations. The advantage of the simulator approach is that it accounts for effects at the pixel scale, such as the screening of clouds low in the atmosphere by clouds above them and the fact that satellite retrievals assume clouds are single layered, while they often occur in multiple layers, both in reality and in the model.

4.2.3 Computation of grid box values

Only monthly means of three hourly model outputs are used in our analysis, gridded at $2.5^\circ \times 2.5^\circ$ resolution. Outputs from the ISCCP simulator require caution at the stage of time averaging. Variables (e.g. cloud albedo) need to be averaged only over daytime and in-cloud points and weighted by the grid box cloud fraction. This produces cloud area weighted in-cloud values. Monthly averages comply with the indications from the CFMIP project (http://cfmip.metoffice.com/README).

Grid box values of cloud droplet effective radius (r_{eff}) and convective mass flux (M_c) are calculated as follows. Model r_{eff} is a multilevel variable. Following Greuell et al. [247], grid box values are obtained averaging r_{eff} over all the model layers, weighing each layer contribution by its LWP at that level. LWP values for each vertical level are computed as the product of the mass fraction of cloud liquid water and the pressure difference between two levels divided by the gravity constant. r_{eff} will be used to investigate boundary layer clouds, for which it is almost constant within a cumulus and increases with height within a stratocumulus [e.g. 143]. This averaging method assigns more weight to the upper layers of the stratocumulus, since the mass fraction of liquid water increases toward the cloud top. The satellite-retrieved r_{eff} is also more representative of the upper portion of the clouds. Finally, LWP, r_{eff} and the mass fraction of cloud liquid and ice water averages are for the cloudy portion only and daylight conditions. This to make a fair comparison with the satellite products.

The convective mass flux, M_c, is a quantity not directly observed, we

retrieve it following Held and Soden [153]. As a first order of approximation, M_c can be derived as $M_c = P/r$, where P is the mean precipitation from satellite retrievals (GPCP or TRMM) and r is the water vapor mixing ratio at the surface from ERA-Interim reanalysis. This approximation assumes that air from the boundary layer is transported into the free-troposphere where most of the water vapor condenses and falls down as precipitation. At the level of detrainment r is at least one order of magnitude lower than at the surface, hence the return flow of vapor into the boundary layer by large-scale subsidence is negligible [17]. Although the convective mass flux is a standard output of EC-Earth, we computed it in the same way from the simulation, in order to make a fair comparison with the observations.

Finally, the longwave and shortwave components of the CRE at the TOA, introduced in Charlock and Ramanathan [177], are defined as:

$$LWCRE = OLR_{clear} - OLR \tag{4.2}$$

$$SWCRE = TRS_{clear} - TRS \tag{4.3}$$

$$NetCRE = LWCRE + SWCRE \tag{4.4}$$

where OLR, TRS, OLR_{clear} and TRS_{clear} refer to the Outgoing Longwave Radiation and the Total Reflected Solar radiation, at the TOA in actual and clear-sky conditions, respectively. The sign convention for the quantities used to define CRE is such that the upward radiative fluxes are positive.

4.3 Global evaluation

Global maps of NetCRE, total cloud cover and precipitation from observations and EC-Earth are shown in Fig. 4.1. EC-Earth reproduces the broad structure of the general circulation, such as the tropical convergence zones, where the precipitation is maximum and the distribution of the low and upper (mid+high) clouds, consistent with the position of the Hadley Circulation and the midlatitude storm tracks. Globally averaged from 1984 to 2007, |NetCRE| is overestimated by about 5 W/m^2 in our model: the cooling effect of the clouds is too strong (Figs. 4.1a-b). Most of this bias arises from the tropical belt, both over land and over ocean and it is partly offset in the midlatitudes (Fig. 4.1c). Along with the SRB radiative data set, Fig. 4.1c also shows the zonal average of the NetCRE bias derived from CERES. This demonstrates that the departures of the simulation from the observations generally exceed the uncertainty in the satellite-based products, so these differences are significant and can be referred to model biases.

In order to distinguish which cloud type is responsible for this bias, cloud cover has been stratified based on the cloud top pressure (P_c). Global maps

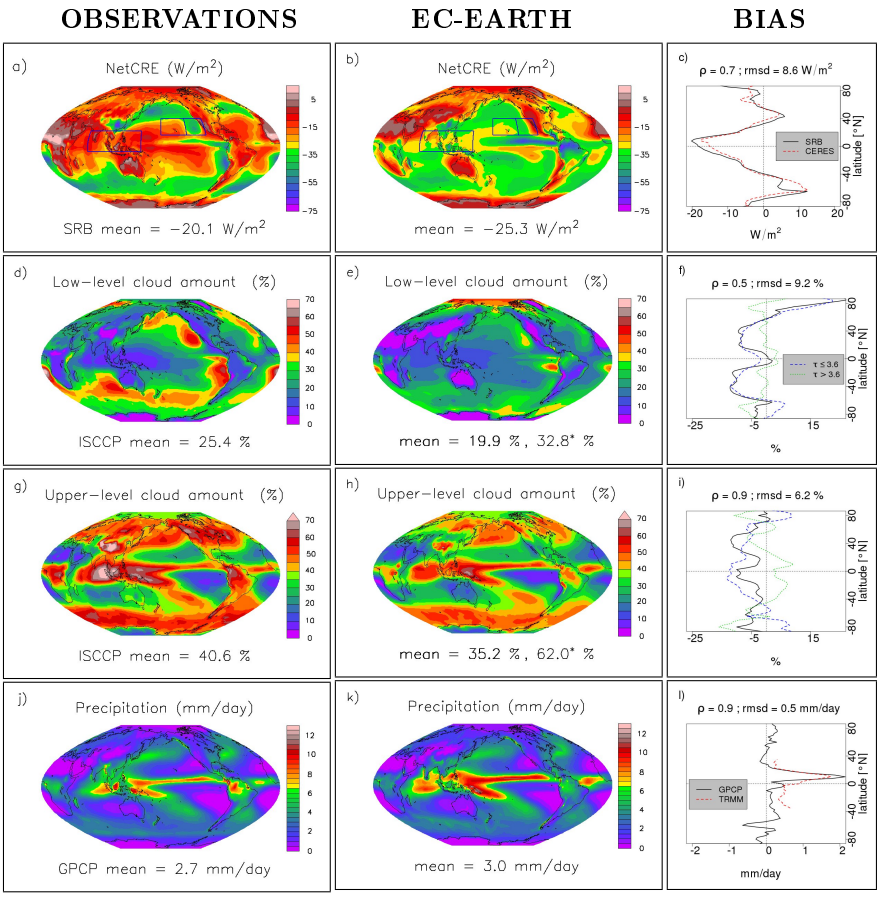

Figure 4.1: Global maps for 1984-2007, a)-c) NetCRE, d)-f) Low-level cloud amount, g)-i) Upper-level (mid+high) cloud amount, j)-l) Precipitation. Left: SRB, ISCCP and GPCP observational data; middle: EC-Earth model simulation; right, black solid lines: zonal mean differences between model and observation (model minus observation), with related correlation coefficient (ρ) and root-mean-square deviation (rmsd). Dashed lines in f) and i) represent zonal mean biases when cloud amount is stratified into ranges of optical thickness (blue lines: $\tau \leq 3.6$, green lines: $\tau > 3.6$). Dashed lines in c) and l) are the zonal mean biases when CERES is used instead of SRB and TRMM instead of GPCP data, respectively. The numbers with asterisk in e) and h) are the global mean cloud amounts computed directly from the GCM and not passed through the ISCCP simulator. Trapeziums in a)-b) delimit regions on which some evaluations presented in this paper focus.

of low-level ($P_c > 680$ hPa) and upper-level cloudiness ($P_c \leq 680$ hPa) from observations and model are shown in Figs. 4.1d-e-g-h. Global means are

reported at the bottom of each figure, both for the clouds from the ISCCP simulator and for the model clouds (with asterisk). The model cloud cover is higher than the cloud cover from the ISCCP simulator and from the ISCCP observations. EC-Earth has too few clouds according to the values from the ISCCP simulator but too many when the model clouds are evaluated. This highlights the importance of using an ISCCP simulator in the models to avoid reaching diametrically opposed conclusions.
The discrepancy between the simulated cloud cover with and without satellite simulator stems from three main assumptions, that are applied in the first case. First: modeled cloud amounts with optical thickness below 0.3 are not considered to make a fair comparison with the observations. ISCCP has difficulties to detect clouds with optical thickness less than about 0.3 [246]. Second: some cloud layers might not be observed from space when shielded by higher clouds. Third: only day-time data are considered, leaving out the diurnal cloud cycle. In the remainder of this study, only cloud values from the ISCCP simulator are considered.

Globally averaged EC-Earth predicts roughly 5% less low-level cloud area fraction. The situation is particularly striking in the subtropics off the west coasts of America, Australia and Africa, where stratocumuli are dominant. These regions coincide with the surface air temperature warm bias noted by Hazeleger et al. [242]. Here it is shown to be related to the underestimated stratocumulus cloud cover and it emphasizes the role of the MBL clouds as a source of bias for the SST bias. Furthermore, the model often fails to capture the local contrasts between adjacent cloud regimes, such as trade cumulus and stratocumulus, both in terms of cloud cover (Figs. 4.1d-e) and radiative fluxes (Figs. 4.1a-b). The two adjacent boxed regions denote areas for which this situation is examined in more detail in section 4.4.1. We also note that the regions mentioned above are next to broad deserts. The soil-dust aerosols from these deserts can alter the cloud properties, in particular their amount [11] and their albedo [162], especially in shallow marine cloud systems [192]. Since the indirect aerosol effects are not explicitly modeled in this simulation, this might be an additional source for the biases detected over these areas.
Low-clouds are also underestimated in the storm tracks of the Northern Hemisphere and over the midlatitude oceans of the Southern Hemisphere (Figs. 4.1d-e-f). Along with Figs. 4.1a-b-c, this is consistent with the 2-m temperature warm bias found in the coupled version of EC-Earth [242], especially for the latter region. The Arctic is the only area where the low-clouds are overpredicted (Fig. 4.1f). This is a typical bias for the EC-Earth model, which affects future climate scenario simulations as well [227]. However, observational errors should also be taken into account: in polar regions, ISCCP cloud amounts are too low by about 15% [246].

The mid and high level clouds are analysed together, following Marchand and Ackerman [188], in order to minimize the effects of retrieval errors in ISCCP. ISCCP tends to detect spurious middle clouds if higher thin clouds overlay the lower clouds and the thermal-infrared method used can detect a lower fraction of high-clouds by underestimating their altitude [e.g. 78, 249]. The ISCCP simulator is designed to imitate these errors; however, if the model has the correct amount of high-level cloud *but* the wrong distribution of high-cloud emissivities, then the simulator will still produce a seemingly incorrect amount of high and middle clouds [Marchand (2012), personal communication]. Therefore, the choice of looking at the combined mid and high level clouds is justified.
Mid+high cloud amount is generally underestimated by about 5% at all latitudes (Figs. 4.1g-h-i). In the midlatitudes the clouds are particularly underpredicted along the storm tracks. Ryan et al. [77] argued that this is likely due to deficiencies in the Tiedtke's parameterization [167]. This scheme predicts clouds in frontal regions using the large-scale vertical velocity (ω), without any information on the subgrid distribution of ω. It is possible that half of the grid box experiences strong upward motion while the other half experiences strong downward motion, as a result the total grid box "large-scale" ω is zero. In this case the Tiedtke's parameterization [167] predicts no condensation, leading to an underestimation of the cloudiness in frontal regions. Using both large-scale ω and the subgrid-scale ω distribution may improve this situation [77].
Fig. 4.1i shows that the model produces too many optically thick ($\tau > 3.6$) upper-level clouds (e.g. cumulonimbus) and too few thin ($\tau < 3.6$) upper-level clouds (e.g. altocumulus), over the tropical belt. Thin (thick) mid and high clouds have a strong warming (cooling) effect on the net radiation [137]. The lack (abundance) of thin (thick) upper-clouds in EC-Earth contributes to the overly negative NetCRE in the tropics (Fig. 4.1c). Too many thick upper-level clouds are consistent with the overestimation of precipitation in the deep tropics (Figs. 4.1j-k-l). The precipitation budget has also been retrieved using another data set (TRMM) to demonstrate that the model biases are generally larger than the uncertainty between the observational estimates (Fig. 4.1l).

The overestimation of thick upper-level clouds in the model can be associated to different reasons. In this study we focus on two important factors. The first stems from the fact that vertical transport of moisture in EC-Earth is mainly due to convection, which points to deficiencies in the convective scheme. The second factor is related to the detrainment of moist convection, an important term for the prognostic equations of the cloud fraction and water content in the cloud scheme (Tab. 4.1). One possibility is that EC-Earth

does not predict enough detrainment at the mid-levels, which allows convection and water vapor to penetrate more deeply in the upper troposphere. As a consequence the formation of towering clouds is favored. Both factors will be discussed in section 4.4.2.

4.4 Tropical performance

The tropical belt (35 °N - 35 °S) is the largest climate region of the world, roughly 50% of the earth's surface, and is the region where EC-Earth exhibits the largest cloud biases (see previous section). For these reasons we focus our analysis on this area.

Fig. 2 shows various cloud-related variables in a ω_{500}-SST phase-space. This compositing technique has been found particularly useful to study the different cloud regimes in the tropical region [39, 128]. The Hadley-Walker circulation is decomposed into a set of dynamical and thermodynamical regimes defined by the monthly means of ω_{500} and SST. These are partitioned into 10 hPa/day and 1 °C wide bins. Monthly means of cloud amounts and radiative fluxes are averaged over the grid boxes associated with the same ω_{500}-SST values. Within this framework, thick low-clouds are mostly found over relatively cold pools with large-scale sinking ($\omega_{500} > 0$) motion, namely the eastern basins of the tropical oceans, while upper-level clouds are mainly expected over warmer SSTs with large-scale rising ($\omega_{500} < 0$) motion, coinciding with the convergence zones. Finally, areas of subsidence and warm SSTs are associated with trade cumulus or mostly clear sky regimes, which are found at the edge of the tropical convergence zones [39].

The contour lines in Fig. 4.2a represent the Probability Density Function (PDF) of ω_{500} and SST as depicted by reanalyses and observations (similar in EC-Earth, not shown). It shows the statistical weight of each bin of the ω_{500}-SST phase-space. The shadings in Fig. 4.2a represent the biases (model minus observation) in the total cloud cover. This is too low, in particular for bins associated with cold and subsidence conditions, namely the stratocumulus region. This is consistent with the underestimation of low-clouds over the eastern basins of the tropical oceans in Fig. 4.1e. The shortage of stratocumulus in EC-Earth is consistent with the negative bias in |SWCRE| over the cold subsident region in Fig. 4.2b (shadings). In contrast, |SWCRE| is overestimated for warmer SSTs, in particular where ω_{500} is positive (trade cumulus region). The magnitude of the biases in SWCRE is far larger than in LWCRE (Fig. 4.2c). This demonstrates that the large bias in NetCRE (Fig. 4.1c) is primarily due to the misrepresentation of SWCRE.

SWCRE accounts for the interaction between solar radiation and clouds. This interaction can be further investigated with the ISCCP cloud albedo

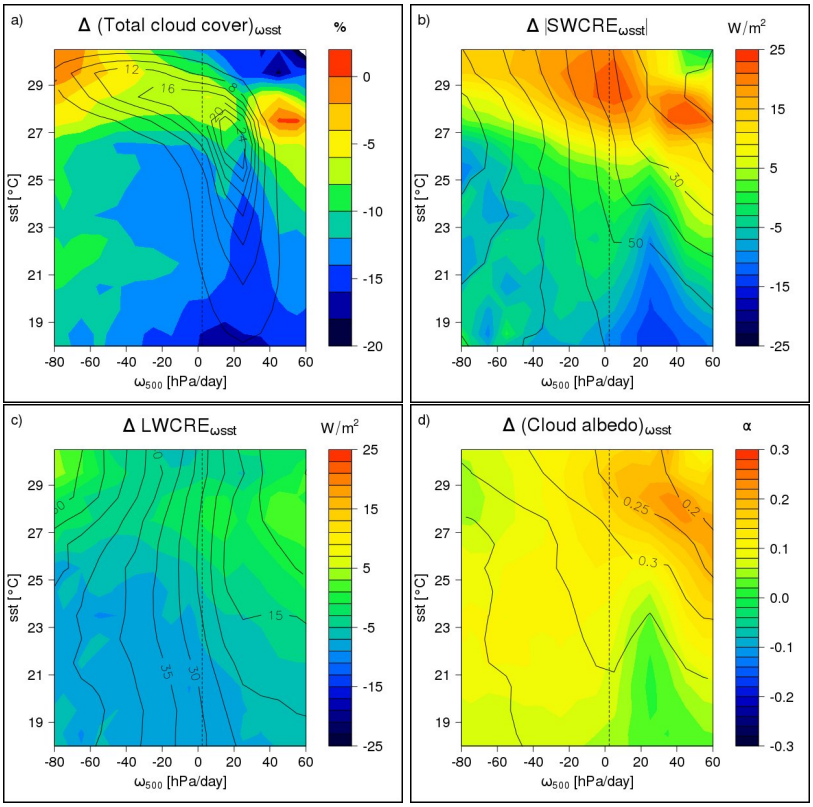

Figure 4.2: Cloud-related variables composited with respect to ω_{500} and SST over the tropical oceans (35 °N - 35 °S) during 1984-2007. a) Total cloud cover, b) |SWCRE|, c) LWCRE, d) Cloud albedo (α). Shadings represent the bias (model minus observation), contours the climatological field from observations, except for a) where contours are the frequency of occurrence of ω_{500} and SST from observations expressed in percentage. Analysis is based on ERA-Interim, ERSST, ISCCP, SRB and EC-Earth data.

(Fig. 4.2d), which is an in-cloud property independent of the cloud amount[2], unlike SWCRE. The model cloud albedo is about right for the stratocumulus region, while the |SWCRE| and the cloud cover are too low for the same area. Therefore, the negative bias in |SWCRE| is primarily due to the shortage of stratocumuli rather than due to the misrepresentation of the microphysical cloud properties. In contrast, EC-Earth overestimates the cloud albedo and the |SWCRE| in areas of warmer SSTs, along with an underestimation of

[2]In the ISCCP simulator, the cloud albedo is the average over cloudy areas and thus is not a function of the cloud amount.

the cloud cover (Fig. 4.2). This implies that the overprediction of the cloud albedo, and by implication of the optical depth, overcompensates the underprediction of the trade cumulus cloud cover and, to a lesser extent, of the upper-level cloud cover. This points to a misrepresentation of the microphysical cloud properties, such as liquid water path, effective radius, etc. These hypotheses are further investigated in the next sections.

4.4.1 Marine boundary layer clouds

MBL cloud simulation in GCMs is by no means trivial and only a few models can predict the extent of these clouds and their CREs realistically [19, 36, 180]. Also the EC-Earth model exhibits large biases when it comes to simulate MBL clouds. In the previous sections we showed that EC-Earth cannot well reproduce regional contrasts in CRE and cloudiness in the subtropics (Figs. 4.1a-b-d-e), mainly due to biases in the SWCRE in subsidence regimes (Figs. 4.2b-c). |SWCRE| is underestimated for stratocumulus dominated areas and overestimated for cumulus-topped boundary layer regions. This can be the result of either too few (high) cloud fraction, too small (large) cloud water contents, too large (small) particle sizes or a combination of any of those. We now investigate which of these gives the largest contribution to the SWCRE bias.

The focus is on the Hawaiian Trade Cumulus [15 °N - 35 °N, 180 °E - 220 °E; (HT)] and Californian Stratocumulus [15 °N - 35 °N, 220 °E - 250 °E; (CS)] regions, as defined in Webb et al. [170], for the years 2003 to 2007. The observations are in broad agreement with the partitioning of the cloud types into these two regimes. Indeed, |SWCRE| (Fig. 4.3a) and cloud cover (Fig. 4.1d) are maximal within the first kilometers off coasts of California and then gradually decrease toward the west. Simulation of these regimes with EC-Earth is poor. |SWCRE| is too low in the CS region and too high in the HT region (Fig. 4.3a), while cloud cover is definitely too low (Fig. 4.1e). Fig. 4.3b shows that the cloud albedo is about right (or slightly underestimated) on average for the CS region and too high for the HT region. These deficiencies are consistent with the findings in the previous section and also representative of other subtropical regions, as demonstrated in Figs. 4.2a-b-d. What was observed at the large-scale can also be found at the regional scale and for a shorter time sampling (1984-2007 and 2003-2007, respectively).

Figs. 4.3c-d show the cloud-top pressure (P_c) and optical thickness (τ) joint histograms for the HT and CS regions, respectively. The shadings represent the mean cloud fraction distribution in EC-Earth, while the contour lines are the biases with respect to the ISCCP observations. The most common cloud type has τ in the mid range, with cloud tops in the lower troposphere,

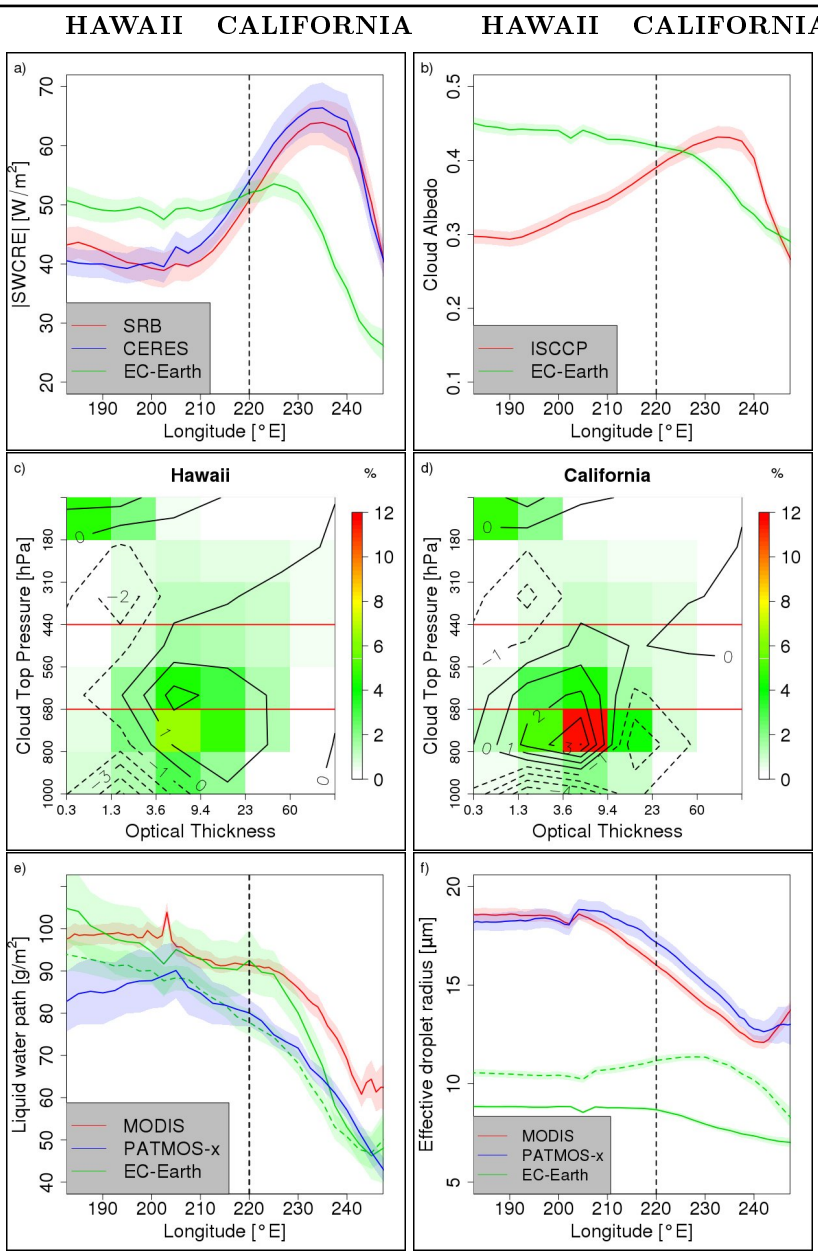

Figure 4.3: Various quantities averaged from 2003 to 2007 over the Hawaiian Trade Cumulus (HT) and the Californian Stratocumulus (CS) regions. Results obtained from EC-Earth are in green. Shadings are the 95% ranges of monthly variability. Meridional averages of SWCRE (a) and cloud albedo (b). Joint histograms of P_c and τ for the HT (c) and CS (d) regions. Colored areas are results from EC-Earth, black contours are model minus observations (solid lines when positive bias, dashed lines when negative). Meridional averages of LWP (e) and r_{eff} (f), dashed lines when the MODIS simulator is used.

for both model and satellite-retrievals. In the HT region EC-Earth simulates too few thin clouds ($\tau < 3.6$) and too many thick clouds ($\tau > 3.6$). Since the cloud albedo is primarily governed by the optical depth, this explains the excessive albedo of the trade cumulus regimes in EC-Earth. Regarding the CS region, the largest biases arise at τ values between 1.3 and 9.4, but compensating errors occur at different altitudes. Overall, the model predicts slightly too few thin and slightly too few thick clouds, which results in a cloud albedo about right or slightly underestimated compared with the observations (Fig. 4.3b).

The inconsistency between satellite-retrieved and simulated visible optical thickness is further investigated by looking separately at the biases in the liquid water path (LWP) and the liquid droplets effective radius (r_{eff}), which are related to τ through the following relationship [140]:

$$\tau = \frac{3}{2} \cdot \frac{LWP}{r_{eff} \cdot \rho_l} \tag{4.5}$$

where ρ_l is the density of liquid water. LWP and r_{eff} are not retrieved by ISCCP, hence MODIS is used as a complementary source of data. The quantity τ somewhat differs between ISCCP and MODIS, but the signs of the biases with respect to EC-Earth are the same and qualitatively comparable (not shown). In order to estimate the uncertainties in the observations, Figs. 4.3e-f also show quantities from PATMOS-x, available in the GEWEX Cloud Assessment Database [110]. The EC-Earth LWP is well simulated: it falls in between the two observational data sets for both the CS and HT regions (solid line in Fig. 4.3e). On the other hand, the EC-Earth r_{eff} is underestimated when compared with MODIS and PATMOS-x, notably for the trade cumulus area (solid line in Fig. 4.3f). The modeled r_{eff} is the vertical mean of the droplet size in each model box, weighted by the liquid water content at each layer (more details in section 4.2.3). This averaging method is somewhat different from how the satellites retrieve r_{eff}. Indeed, it does not take into account that satellite-retrieved r_{eff} depends on the wavelength (λ) used for the observation. MODIS retrieves r_{eff} using a combination of three different λ [186], the main difference being that absorption by liquid water decreases with decreasing λ. That means that the vertical sampling of droplets becomes progressively deeper when λ reduces, so it can include contributions from drizzle [214]. Differences in the retrieved r_{eff} using different λ can exceed 10 μm [252]. This then implies that r_{eff} from MODIS can be higher than r_{eff} simulated by EC-Earth in part because of the different vertical average assumptions. This issue is addressed by passing the necessary input profiles to the MODIS simulator included in COSP version 1.3. The r_{eff} bias is now smaller but still considerable for the HT region (dashed line in Fig. 4.3f). On the other hand, the LWP calculated using the MODIS simulator

reduces, but agrees fairly well with the observations (dashed line in Fig. 4.3e). Therefore, the underestimation of r_{eff} appears to be the main reason for the overestimation of τ and hence of the cloud brightness in EC-Earth.

Droplet sizes in EC-Earth are simulated based on Martin et al.'s parameterization [157]. Given a constant droplet concentration (51 cm^{-3} over ocean; 313 cm^{-3} over land), r_{eff} is parametrized using the liquid water content. Several studies showed that the droplet concentration is not constant and depends on the availability of cloud condensation nuclei (CCN), their size distribution and chemical composition, as well as on the intensity of convective updrafts at the cloud base [e.g. 185]. Moreover, Martin et al.'s parameterization [157] has been devised for steady warm stratocumulus, homogeneous clouds where entrainment processes and penetration by cumulus clouds are negligible. Martin et al. [157] have shown that the same parameterization is far less reliable in other circumstances, for instance when cumulus clouds affect a stratocumulus layer. The HT region is an example of such a case and in this region the simulated r_{eff} exhibits the largest departures from the observations (Fig. 4.3f). Therefore, a more refined parameterization of the effective droplet radius is desirable to reduce the bias in the cloud albedo.

To summarize, |SWCRE| in the stratocumulus regions is underestimated, but τ is about right. This leaves underestimation of cloud amount by the model as the most important cause for the SWCRE bias in this region. On the other hand, |SWCRE| in the cumulus-topped MBL regions is overestimated, along with τ, while the cloud fraction is too low, but not as much as for the stratocumuli. This leaves misrepresentation of cloud microphysics as the main source of the SWCRE bias for the trade cumulus clouds. In particular, EC-Earth simulates a realistic LWP for MBL clouds, but r_{eff} is too low compared with observations.

4.4.2 Deep tropics

Fig. 4.4a is similar to Figs. 4.3c-d, but for the tropical western Pacific [5 °S - 20 °N, 70 °E - 150 °E; (WP)]. This region was selected by Webb et al. [170] as representative of a typical deep convective area in the tropics. The most common clouds are the highest and thinnest (shadings in Fig. 4.4a), corresponding to ice clouds near the tropopause. This cloud type occurs too often ($P_c < 180$ hPa) in EC-Earth compared with the ISCCP observations (contour lines in Fig. 4.4a). Below this level, the model underestimates the amount of thin clouds ($\tau < 3.6$) and, to a lesser extend, overestimates the amount of thick clouds ($\tau > 3.6$). This is summarized in Fig. 4.4b, which compares profiles of cloud cover with height. The profiles are obtained by summing the values of the joint histogram in Fig. 4.4a in the six columns

(τ) along each row (P_c). EC-Earth predicts a larger fraction of clouds with cloud top above 12 km ($P_c < 180$ hPa), while produces too few clouds below, in the mid and high troposphere, compared with the satellite retrievals. In the mid and high troposphere ($550 < P_c < 200$ hPa) the temperature ranges between 0 °C and −50 °C (blue line in Fig. 4.4b), where supercooled liquid water can coexist with ice. In this range of temperatures, EC-Earth exhibits the largest biases in cloud cover, which points to deficiencies of the model in dealing with mixed-phase clouds.

Fig. 4.4c shows the cloud cover as a function of τ (sum of all the P_c layers for each τ bin of the joint histogram in Fig. 4.4a). For comparison, we also show observations from MODIS and MISR (Multiangle Imaging SpectroRadiometer; [189]). The latter instrument employs retrieval techniques of optical depth quite similar to that of ISCCP. Indeed, the two observational estimates agree very well. On the other hand, MODIS retrieves a higher amount of optically thick clouds compared with the other two instruments. This appears to be a systematic overestimation due to imperfect ice models used in MODIS retrievals [193]. The largest differences among the observational estimates of the cloud cover are for $\tau < 3.6$. This is mainly due to the way these satellite instruments treat partly cloudy pixels [189, 193]. The simulators do not actually account for these features that cause differences in the retrieved optical depth [193]. Bearing in mind the observational uncertainties, EC-Earth appears to have too many optically thick clouds and not enough optically thin clouds, resulting in a flatter τ distribution than observed. The overestimation of the optical thickness leads to overestimation of |SWCRE| in this and other warm convective regions (Fig. 4.2b). In contrast, no appreciable disagreement is found for the LWCRE, consistent with the good overlap between simulated and observed P_c in Fig. 4.4d. For the whole region the agreement is even better due to compensating errors at different longitudes. The LWCRE is underestimated around 100 °E and overestimated at longitudes greater than 130 °E. Consistently, P_c is too large west of 110 °E and too small to the east. Despite biases in the profile of the cloud cover with height (Fig. 4.4b), the mean P_c is well reproduced, indicating that the correct prediction of LWCRE arises from compensating errors in the cloud vertical and horizontal distribution rather than a correct profile of P_c.

The cloud misrepresentation in the deep tropics could be due to deficiencies in the parameterization of various physical processes and their interactions. We focus now on the convective scheme, since the vertical transport of moisture in EC-Earth is mainly due to convection. In such a scheme the strength of the updrafts in a cumulus ensemble is characterized by the mass flux, which quantifies the amount of mass transported in the vertical. The convective mass flux (M_c) has been derived as explained in section 4.2.3. The

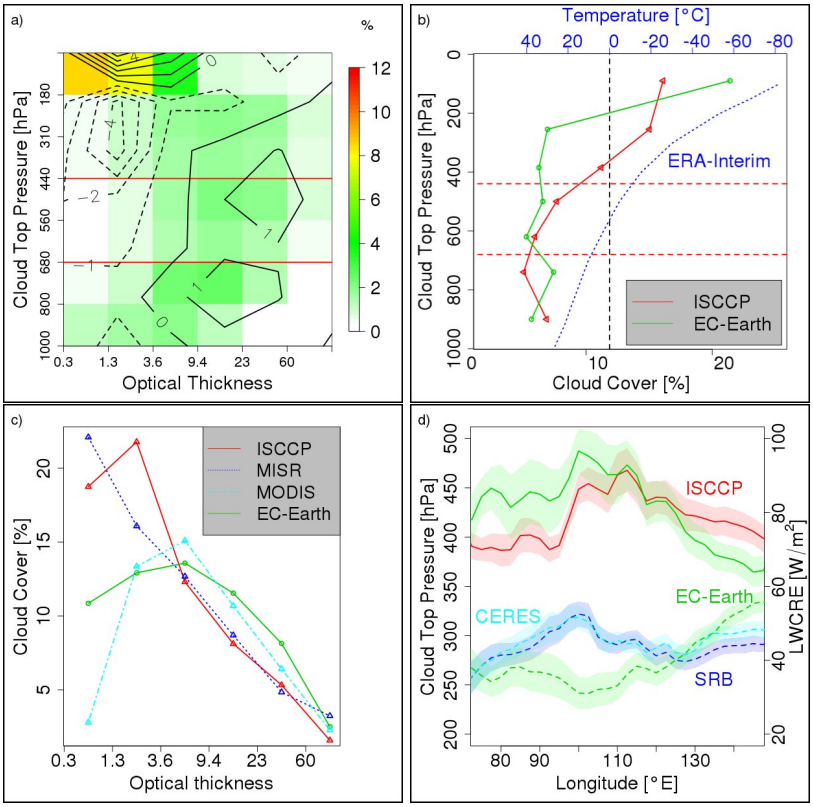

Figure 4.4: a) As in Figs. 4.3c-d, but for the tropical western Pacific region [5 °S - 20 °N, 70 °E - 150 °E; (WP)]. b) Cloud cover as a function of the cloud-top pressure (P_c), equal to the sum of all the optical thickness (τ) bins for each P_c layer in a); air temperature profile is also shown (blue line); the black vertical line indicates the 0 °C temperature. c) Cloud cover as a function of τ, equal to the sum of all the P_c layers for each τ bin in a), along with MODIS and MISR observations. d) P_c (solid lines) and LWCRE (dashed lines) meridionally averaged over the WP region. Shadings indicate the 95% ranges of monthly variability. Monthly values of ERA-Interim, ISCCP, MODIS, MISR, SRB, CERES and EC-Earth data are used for the period 2003-2007.

range of negative ω_{500} values (representative of upward motion) is binned and monthly mean values of M_c are averaged over the grid boxes associated with the same monthly mean ω_{500} bin, in order to get $M_{c\omega}$. The mean of the 60 monthly composites from 2003 to 2007 accounts for the mean relationship between M_c and ω_{500} and is shown in Fig. 4.5. For the composite, the grid points over ocean and the grid points over land have been considered sepa-

rately.
Fig. 4.5 shows that the mass flux in the model is overestimated[3], notably over the ocean basins associated with extremely negative values of ω_{500}. The stronger convective activity in our model is also confirmed by the higher occurrence of the ω_{500} extremes than depicted by the reanalyses (Fig. 4.5b). We show this by binning the Hadley-Walker circulation into a series of dynamical regimes defined by values of ω_{500}. The statistical weight of each dynamical regime, i.e. the PDF of ω_{500} (P_ω), from ERA-Interim or NCEP-DOE reanalyses is then subtracted from the EC-Earth P_ω. The moderate values of ω_{500} occur less frequently in EC-Earth with respect to what is "observed", but the extremes of P_ω are more populated in our model. This implies an overall strong vertical motion in EC-Earth, in agreement with the picture of too strong mass flux drawn above.
Further evidence was presented as part of the European Cloud Systems study (EUROCS), where Derbyshire et al. [221] have shown that the mass flux in the ECMWF Tiedtke parameterization of convection [166] is unrealistically high compared with Cloud Resolving Models (CRMs). Since the development of thick anvil clouds is favored in areas of intense convection ([119], chapter 9), we interpret the tendency of EC-Earth to overestimate the thick clouds in the deep tropics as due, at least in part, to the excessive mass flux computed in the Tiedtke's convective scheme [166].

The mass flux is very sensitive to mixing between clouds and their environment by the so-called entrainment and detrainment processes, which describe the intrusion of dry environmental air into the cloud and the outflow of cloudy air into the environment, respectively [e.g. 103]. Focusing on the latter, too weak detrainment would lengthen the lifetime of the convective thick clouds, which in turn persist too long in the same area, contributing to the positive bias in the precipitation budget, larger over the Inter Tropical Convergence Zone (ITCZ; Figs. 4.1j-k-l). The detrainment modulates the mass flux profile [e.g. 49] and an underestimation of detrainment causes the updrafts to extend higher into the atmosphere reaching the tropopause. At this level the anvil clouds are forced to stretch and generate cirrus, which are too many in EC-Earth (Fig. 4.4a). Moreover, too weak detrainment in the mid-troposphere is consistent with the underestimation of thin clouds at this level (Fig. 4.4b). These are typically mixed-phase clouds associated with deep convection (Fig. 4.4b, [98]) and usually form when ice crystals are surrounded by sufficient water vapor [160]. The vapor in the mid and high tropical troposphere is supplied by the detrainment in deep convective clouds [245].

[3]We have also compared the standard output updraft M_c in mid-troposphere from the model with the observations and the overestimation is even larger (not shown).

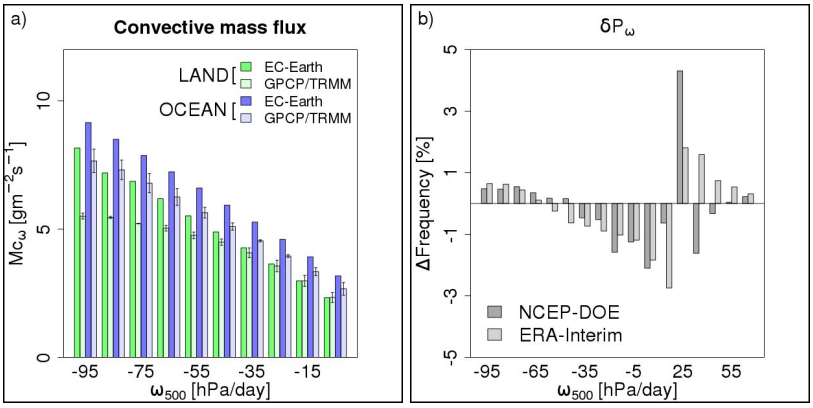

Figure 4.5: a) Convective mass flux ($M_{c\omega}$) composited with respect to ω_{500} over land and over ocean in the tropics (35 °N - 35 °S). Dark-colored bars: EC-Earth outputs are used. Light-colored bars: ERA-Interim, GPCP and TRMM data are used. Vertical error bars represent the standard deviation of the retrieved $M_{c\omega}$ that results from differences between the two precipitation data sets (GPCP and TRMM). b) Model PDF minus reanalysis PDF of marine ω_{500} (δP_ω) derived from EC-Earth and two independent meteorological reanalyses: NCEP-DOE and ERA-Interim. The difference is expressed in percentage. Monthly values for the period 2003 to 2007 are used.

The strong underestimation of thin mixed-phase clouds in mid-troposphere could also be due to the treatment of liquid and ice water phases in the model. We show this by considering vertical profiles of temperature and mass fractions of liquid and ice water[4] in the troposphere, meridionally averaged over the WP region. The range of temperature in this height-longitudinal plane is binned into intervals of 2 °C. Then, monthly mean values of mass fraction of liquid/ice water are averaged over the grid boxes with the same temperature-binned values. The mean of the 60 monthly composites from 2003 to 2007 represents the mean relationship between the liquid/ice water and the temperature in the troposphere.

In Fig. 4.6, the frequency distribution of the temperature bins (PDF_T) shows that freezing temperatures are not rare in the deep tropics. The distinction between ice and liquid water phases in EC-Earth is a function of temperature: in the model all the liquid water present below a certain temperature threshold is converted into ice. Because of this parameterization the mass fraction of cloud liquid water drops to zero below -23 °C (Fig. 4.6), whereas observational evidences show that supercooled liquid can occur till temperatures approaching -40 °C [e.g. 248]. Also the ECMWF IFS model

[4] Mass of cloud liquid (or ice) water in the grid cell divided by the mass of moist air.

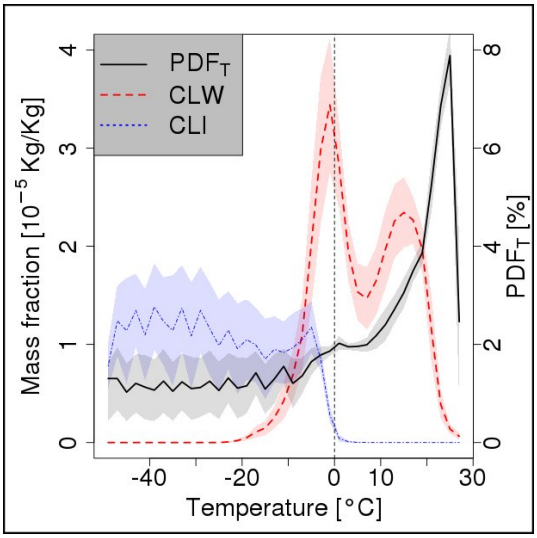

Figure 4.6: Mass fraction of cloud liquid (CLW) and ice (CLI) water composited on temperature in the longitude-height plane meridionally averaged over the tropical western Pacific region (5 °S - 20 °N, 70 °E - 150 °E). In addition, the frequency distribution of the temperature bins (PDF$_T$), expressed in percentage, is plotted (black solid line). Shadings represent the standard deviation of the monthly variations. Monthly values of EC-Earth simulation outputs are used for the period 2003-2007.

used the same parameterization to distinguish between liquid and ice water phases, and indeed it used to underestimate the liquid phase at very low temperatures considerably [41]. This bias has been reduced in later versions of the IFS model using separate prognostic variables for liquid and ice [150]. Since supercooled water is necessary for the ice crystals to form and grow mixed-phase clouds [10], the lack of liquid water in mid-troposphere may be an additional reason for the shortage of mid-tropospheric thin clouds in EC-Earth.

In conclusion, deficiencies in the convective scheme and in the detrainment parameterization are likely key sources for the biases in precipitation and CREs in the deep tropics (Fig. 4.1). An additional source of bias is likely related to the temperature-dependent function which partitions the water condensate into ice and liquid, leading to underestimate the formation of mixed-phase clouds.

4.5 Relationships between meteorological conditions and seasonal cloud variability

We now evaluate EC-Earth at the seasonal time scale by analysing the seasonal variability of the low-cloud amount in the subtropical oceans. The regions selected are identical to those in Klein and Hartmann [7] and the results are plotted in Fig. 4.7. In the Peruvian (10 °S - 20 °S, 80 °W - 90 °W) and Californian (20 °N - 30 °N, 120 °W - 130 °W) regions, the peak of the low-cloud amount occurs in JJA at nearly 75%, with the minimum in DJF at about 40% (Fig. 4.7 red lines). The Canary Islands region (15 °N - 25 °N, 25 °W - 35 °W) also experiences the peak of cloudiness during the Northern Hemisphere summer, but with only 45% of cloud cover. The minimum cloud amount for this region occurs in SON, which coincides with the season of maximum cloud cover for the Namibian region (10 °S - 20 °S, 0 °E - 10 °E) at 70%.
The seasonal cycle of the low-level clouds is associated with the seasonal variation of the environmental conditions and resembles the stratocumulus-to-cumulus transition [147, 243]. The mechanisms involved in such a transition are associated with changes in the environmental conditions and are described in several studies [7, 116, 206].

EC-Earth reproduces the seasonal cycle of the low-clouds in the subtropics well, but, as expected from the analyses in the previous sections, the cloud cover is systematically underestimated in every season (green lines in Fig. 4.7). The model predicts peaks of cloudiness in agreement with ISCCP observations in all the stratocumulus dominated areas, although the minima of the cloud amount not always coincide with the observations. The Canary Islands region has the lowest cloudiness in DJF for EC-Earth and not in SON, as for ISCCP. In the Namibian region, the cloud cover remains nearly constant from December to May, whereas the simulation predicts a minimum in MAM.

Errors in the representation of the relationships between meteorological conditions and clouds can be a potential source for such biases. From a parameterization perspective, cloud properties must be represented in terms of environmental conditions computed by GCMs at each time step [116]. The ability of EC-Earth to replicate the relationships between environmental factors and MBL cloud amount in the observations is evaluated at the seasonal scale in the Namibian region. We address this issue by following the method proposed in Lacagnina and Selten [31]. This is a diagnostic technique where several atmospheric properties are used to define regimes, in which cloud-related variables are composited. This framework is employed to identify and synthesize cloud deficiencies in the simulation and to connect those to

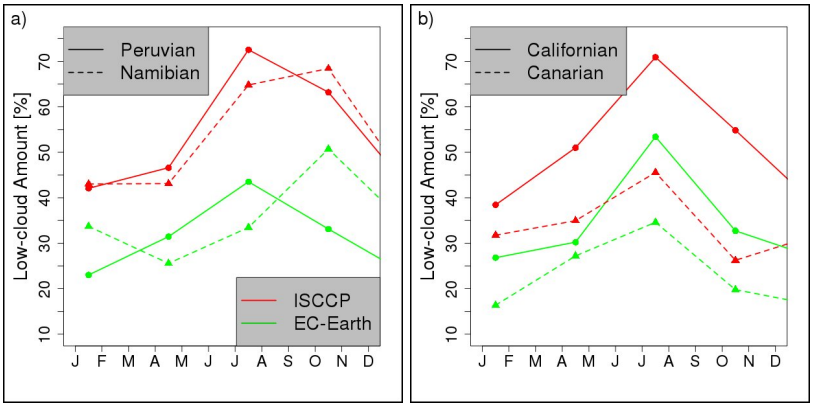

Figure 4.7: Seasonally averaged low-level cloud amounts for the Peruvian (10 °S - 20 °S, 80 °W - 90 °W) and Namibian (10 °S - 20 °S, 0 °E - 10 °E) regions in a) and for the Californian (20 °N - 30 °N, 120 °W - 130 °W) and Canarian (15 °N - 25 °N, 25 °W - 35 °W) regions in b). Green lines indicate EC-Earth simulations and red lines ISCCP satellite observations for the period 1984-2007.

specific physical processes that are dominant in that regime definition. Monthly mean cloud amount (C) is composited by different meteorological variables (γ). If C_γ is a composite of C in a bin defined by the value of γ, and P_γ the frequency of this bin, the area-averaged C ($\overline{C}$) may then be defined as: $\overline{C} = \int_\gamma P_\gamma C_\gamma \, d\gamma$. Hence, the temporal change in $\overline{C}$ ($\overline{\delta C}$) can be expressed as:

$$\overline{\delta C} = \underbrace{\int_\gamma \delta P_\gamma C_\gamma \, d\gamma}_{\text{environmental forcing}} + \underbrace{\int_\gamma P_\gamma \delta C_\gamma \, d\gamma}_{\text{residual forcing}} + \underbrace{\int_\gamma \delta P_\gamma \delta C_\gamma \, d\gamma}_{\text{co-variation}} \tag{4.6}$$

The rhs of Eq. 4.6 is the sum of a term arising from a temporal change in P_γ (δP_γ), called the *environmental forcing component* (hereafter EFC), a term arising from a temporal change in C for a given γ regime (δC_γ), called the *residual forcing component* and a co-variation term. The γ-EFC isolates the effect of a γ environmental condition on the cloud change, whereas the residual forcing component contains the effects of other environmental factors on the clouds, which are not captured by γ.

Here we apply this technique on the seasonal time-scale. The 4 seasonal γ-PDFs (3-mo mean of monthly P_γ for each season) of a specific year have been computed and from each the annual γ-PDF for that year (12-mo mean of monthly P_γ) is subtracted (δP_γ). The integral of δP_γ multiplied by the annual mean of monthly C_γ will be referred to as the EFC. The EFCs are then correlated to $\overline{\delta C}$, which in this case is the seasonal anomaly of C with respect

to the annual mean [spatially and seasonally averaged low-cloud cover of a specific year (between 1984 and 2007) when the annual mean is removed]. $\overline{\delta C}$ and γ-EFC can be correlated to quantify to what extent the seasonal changes in C are tracked by the seasonal changes in the environmental conditions (γ). The higher the correlation coefficient[5], the more similar the frequency and the phase of the two quantities ($\overline{\delta C}$ and γ-EFC, with a total of 96 relations for 1984-2007). Furthermore, using the EFCs method, it is possible to quantify the relative contribution of a γ factor to the seasonal cloud amount anomalies. The slope of the linear regression between $\overline{\delta C}$ and γ-EFC quantifies to what extent a γ environmental factor describes the seasonal change in C. The closer to 1 the slope, the closer the amplitudes of the two quantities.

The results are displayed in a plot similar to a Taylor diagram (Fig. 4.8). The radial axis denotes the slope of the regression coefficient between each EFC and $\overline{\delta C}$ and the azimuthal axis the correlation coefficient between these two quantities. Perfect agreement corresponds to a point at correlation ± 1 and regression coefficient one. The points are derived from ISCCP low-level clouds combined with observations and reanalyses, while the triangles are derived from EC-Earth outputs. Using this approach the observations exhibit well-known dependencies, such as the negative correlation between low-clouds and SST and the positive correlation between low-clouds and LTS.

The signs of the correlation between EFCs and $\overline{\delta C}$ are consistent between simulations and observations (Fig. 4.8), except for q_{700}-EFC. q_{700} is the specific humidity in the free-troposphere just above the boundary layer and affects the moisture exchange at the top of the MBL. Moistening of the free-troposphere has two opposing effects. More water vapor just above the boundary layer enhances the downwelling longwave radiation, which reduces the radiative cooling at the cloud top. As a result, the MBL turbulence production is reduced, which promotes decoupling-like conditions. On the other hand, more free-tropospheric moisture reduces the drying effect of the entrained air into the cloud layer, which favors more cloud cover [95]. The negative correlation coefficient between q_{700}-EFC and $\overline{\delta C}$ suggests that the former effect prevails on the latter in this region. Misrepresentation of the role of q_{700} points to deficiencies in the parameterization of the entrainment and/or in the turbulence scheme in EC-Earth and can be an additional cause for the lack of stratocumulus in the model. Fig. 4.8 shows that the regression coefficients between the EFCs and $\overline{\delta C}$, which quantify the relative importance of γ in determining the cloud regime, are always underestimated in EC-Earth, compared with the observations. The model is thus not able to

[5]When statistically significant, the correlation coefficient between γ-EFC and $\overline{\delta C}$is always positive by construction. We adjust it with the sign of the correlation between spatially and seasonally averaged C and γ, to make this relationship visible, as in Lacagnina and Selten [31].

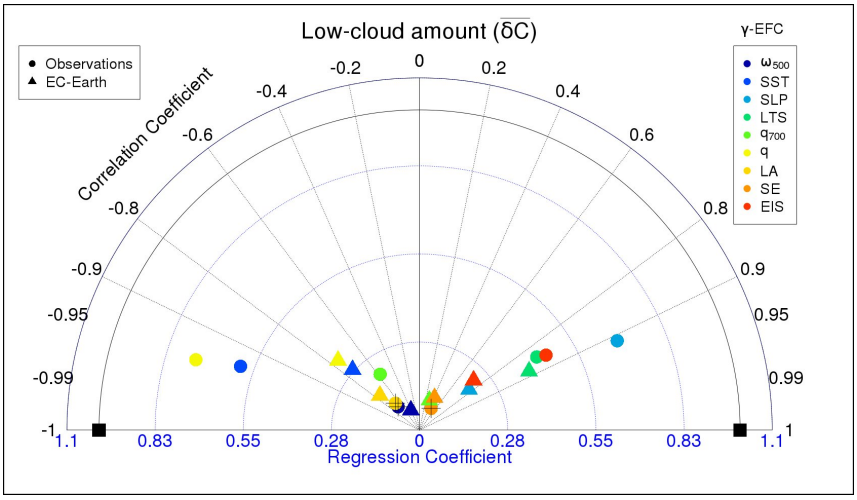

Figure 4.8: "Taylor" diagram showing the relationship between the seasonal variation of low-level cloud amount ($\overline{\delta C}$, annual mean removed) and the contribution of the different environmental factors (γ-EFC) to this seasonal variation (see legend). The relationship is characterized in terms of the correlation coefficient and the slope of the linear regression between the two quantities ($\overline{\delta C}$ and γ-EFC) for the Namibian region (10 °S - 20 °S, 0 °E - 10 °E). ω_{500} represents the pressure vertical velocity at 500 hPa, SST the sea surface temperature, SLP the sea level pressure, LTS the lower-tropospheric stability, q_{700} and q are the specific humidity at 700 hPa and at the surface respectively, LA and SE are the latent and sensible heat fluxes respectively, EIS is the estimated inversion strength. ERA-Interim, ERSST, ISCCP, OAFlux and EC-Earth data are used for the period 1984-2007. When the annual mean composite C_γ describes less than 10% of the C variation in the observations, a cross overlaps the points.

simulate the proper impact of the changing environmental conditions on the clouds. It is also worth noting that, despite the model having been forced with observed SSTs, the correlation and the regression coefficients between $\overline{\delta C}$ and SST-EFC are lower in EC-Earth. This weaker sensitivity of the simulated low-clouds to the SST changes in the current climate, casts doubts on the reliability of our model to reproduce properly stratocumulus amount changes in a scenario simulation of a warmer climate. Nevertheless, the gross relationships between γ factors and cloud cover (Fig. 4.8) are reasonably well reproduced and lead to a quite realistic simulation of the seasonal cycle of the MBL clouds (Fig. 4.7).

4.6 Summary and discussion

This study presents the first detailed evaluation of the cloud biases in EC-Earth using the ISCCP simulator and the observational ISCCP data set. Using satellite simulators in the models is important to avoid reaching diametrically opposite conclusions at the stage of the output evaluation. The cloud amounts in EC-Earth are too high when the ISCCP simulator is not active and too low when it is active. This is due to specific assumptions made in the latter case, which are discussed in the text. The satellite simulator strategy consistently defines the cloud quantities to be compared with the observations, which removes much of the ambiguity when it comes to evaluating cloud simulations with satellite retrievals.

Model biases were evaluated from the global to the regional space scales and from the multidecadal to the seasonal time scales. Despite the generally good agreement, notable biases do exist between EC-Earth and observations. Globally averaged from 1984 to 2007, the model overestimates the cooling effect of the clouds, in particular over the tropical belt. Stratifying the clouds based on their height and their thickness helped to suggest possible reasons for errors in NetCRE.
EC-Earth frequently underestimates the cloud cover at all latitudes relative to the ISCCP observations. The situation is particularly striking for the low-clouds in the subtropical regions, where stratocumulus are dominant. The upper-clouds (mid+high) are underestimated at every latitude, but two opposing biases are present in the tropical belt, where the model predicts too few thin upper-clouds and too many thick upper-clouds. The overestimation of the cloud optical depth overcompensates the underprediction of the total cloud cover, giving rise to an overly negative NetCRE, i.e. a too strong cloud cooling effect in EC-Earth. Furthermore, the abundance of thick upper-clouds is also reflected in the overestimation of the total precipitation in the deep tropics.

Underestimation of total cloud cover and overestimation of optically thick clouds is common in many climate models [65, 180], with some recent GCMs having reduced the latter [9]. It is shown that the largest biases in EC-Earth, in terms of radiative fluxes, cloud amount and precipitation, come from the tropical belt, which is the main focus of this study. The biases in NetCRE are driven by its shortwave component. |SWCRE| is underestimated for stratocumulus regimes and overestimated for cumulus-topped boundary layers and deep convective cloud regimes. We investigated this point further at the regional scale.

The |SWCRE| in the stratocumulus regions is underestimated, but the optical thickness is about right. This leaves underestimation of cloud amount by the model as the most plausible cause for the SWCRE bias in this region. On

the other hand, the |SWCRE| in the trade cumulus regions is overestimated, along with the optical thickness, while the cloud fraction is too low, but not as much as for the stratocumulus. This leaves misrepresentation of cumulus microphysics as the main source of the SWCRE bias for the trade cumulus clouds. We took one step further by analysing the MBL cloud microphysics in more detail using MODIS and PATMOS-x observations as complementary sources of data. We found that the LWP is well simulated in our model, but the liquid droplet size is underestimated, notably for trade cumuli. This latter appears to be the main reason for the excessive cloud brightness in EC-Earth. We suggest that a more refined parameterization of the effective droplet radius is desirable. Nevertheless, because of uncertainties in the observations and in the comparison between model and observations this conclusion demands further investigation. These problems also highlight the need for more independent cloud data sets with suitable satellite simulators embedded in the model code. This approach has turned out fruitful in a number of studies [2, 188, 244] and it is advisable for future EC-Earth cloud evaluations.

Departures from observations are also found in the deep tropics. Similarly to other models [e.g. 170, 188], EC-Earth has too many optically thick clouds and not enough optically thin clouds. The overall overestimation of the optical thickness leads to the overestimation of |SWCRE|. Analysis of the cloud amount as a function of the height, revealed that EC-Earth predicts a larger fraction of thin clouds with cloud top above 12 km (i.e. cirrus) compared with the ISCCP retrievals. In the mid and high troposphere, where supercooled liquid water can coexist with ice, the underestimation of the cloud cover is particularly noteworthy. This points to difficulties of the model in dealing with mixed-phase clouds, that we linked to the temperature-dependent parameterization that distinguishes between ice and liquid water phases. The ECMWF IFS model used to suffer the same bias, where it has been reduced by employing a new cloud scheme with separate prognostic variables for liquid and ice water, allowing a wide range of supercooled liquid water for a given temperature [150]. Despite biases in the profile of the cloud cover with height, the mean cloud top pressure is fairly well reproduced, indicating that the correct prediction of LWCRE arises from compensating errors in the vertical distribution of the clouds. Therefore, the positive bias in |SWCRE| is not offset by a similar bias in LWCRE, which is the reason for the overly strong cooling effect of the clouds in EC-Earth.

The overestimation of anvil clouds in the deep tropics can be linked, at least in part, to the excessive mass flux computed in the Tiedtke's convective scheme [166]. The mass flux and the large-scale circulation in the model are too strong, in particular over the oceans. Guilyardi et al. [64] claimed that using a different convective scheme (Kerry-Emanuel [5]), with a more com-

plex representation of downdrafts, helps to reduce an otherwise overactive convection, notably over the oceans. The role of the detrainment has also been discussed and we conclude that deficiencies in the detrainment parameterization and in the convection scheme may be key sources for the biases in precipitation and CREs in the deep tropics for EC-Earth.

Finally, the model was evaluated at the seasonal time scale, analysing various cloud-controlling factors responsible for the seasonal variability of the low-clouds in the subtropics. The realistic simulation of the seasonal cycle of MBL clouds is attributed to the model skill in reproducing the relationships between meteorological conditions and cloud cover, albeit some departures from observations do exist. Of particular concern is the wrong sign of the correlation between specific humidity in the free-troposphere and low-cloud amount. We link this to deficiencies in the parameterization of the entrainments and in the turbulence scheme in EC-Earth. This can be an additional reason for the underestimation of the stratocumulus cover at the seasonal and multidecadal time scales. We stress that it is important to evaluate the ability of GCMs in reproducing the observed covariation between clouds and environmental conditions, since systematic errors in these relationships cast doubts on the ability of the model to represent realistically the cloud changes in a changing climate.

Nevertheless, in view of the wide range of sources for cloud biases in a GCM, we do not claim to give a complete explanation for all the biases found in this study. The cloud misrepresentation is arguably due to deficiencies in different parameterizations of the model and their interactions. For instance, the plane-parallel representation of the clouds with maximum-random overlap, used in several models and also in EC-Earth (Tab. 4.1), can lead to biases in the cloud amount and CREs [94]. Shonk et al. [179] have recently demonstrated that representing the horizontal cloud inhomogeneity and assuming exponential-random overlap helps to reduce SWCRE biases, in particular in marine stratocumulus regions. Furthermore, increasing the vertical resolution can sometimes help. Indeed, accurate simulation of LWP for boundary layer clouds requires vertical grid spacing below 100 m [27, 203], which is not currently feasible for a GCM. One possibility to overcome the issue has been proposed by Marchand and Ackerman [196]. They show that models can successfully be modified to support an adaptive vertical grid (i.e. a model that is able to add vertical layers where and when needed) rather than trying to use a fixed grid with high vertical resolution.

Although EC-Earth exhibits reasonably good skill in simulating clouds, the model weaknesses discussed above indicate that more effort is needed to improve the physical parameterizations employed. In this study the general problem areas were identified, with the goal of giving some guidance on where

the emphasis for future development in cloud parameterizations should be. A number of parameters and processes to adopt have been suggested and these require further investigation. Development focused on those areas, together with dedicated sensitivity experiments, can likely reduce the uncertainties in the cloud representation. Clouds affect the radiation budget, the hydrological cycle, temperature and the general circulation. Thus, reduction of cloud biases is central to improve the model as a whole. Sensitivity experiments motivated by the findings in this study are underway and the results will be reported separately.

Acknowledgments

The research leading to these results has received funding from the European Union's Seventh Framework Program (FP7/2007-2013) under grant agreement n° 244067.
The authors thank Pier Siebesma and Jelle van den Berk for the useful suggestions on the presentation. We are also grateful to the three anonymous reviewers for their constructive comments that have helped the improvement of this paper. SRB data were obtained from the NASA Langley Research Center Atmospheric Science Data Center. COSP was obtained from the CFMIP website. ISCCP, MODIS and PATMOS-x data were obtained from the ClimServ Data Center of IPSL/CNRS.

Chapter 5

Impact of changes in the formulation of cloud-related processes on model biases and climate feedbacks

To test the impact of modeling uncertainties and biases on the simulation of cloud feedbacks, several configurations of the EC-Earth climate model are built altering physical parameterizations. An overview of the various radiative feedbacks diagnosed from the reference EC-Earth configuration is documented for the first time. The cloud feedback is positive and small. While the total feedback parameter is almost insensitive to model configuration, the cloud feedback, in particular its shortwave (SW) component, can vary considerably depending on the model settings. The lateral mass exchange rate of penetrative convection and the conversion rate from condensed water to precipitation are leading uncertain parameters affecting the radiative feedbacks diagnosed. Their impacts offset each other. Consistent with other studies, we find a strong correlation between low-cloud model fidelity and low-cloud response under global warming. It is shown that this relationship holds only for stratocumulus regimes and is contributed by low-cloud cover, rather than low-cloud microphysics. Model configurations simulating higher stratocumulus cover, that is closer to the observations, exhibit a stronger positive SW cloud feedback. This feedback is likely underestimated in the reference EC-Earth configuration, over the eastern basins of the tropical oceans. In addition, connections between simulated high-cloud altitude in present-day climate and longwave cloud feedback are discussed.

This chapter is under review for publication in Journal of Advances in Modeling Earth Systems as: *Lacagnina C., F. Selten and A. P. Siebesma. Impact of changes in the formulation of cloud-related processes on model biases and climate feedbacks. JAMES, 2014.*

5.1 Introduction

Clouds represent a key challenge for climate modeling and substantial disagreement between general circulation models (GCMs) and observations still exists [2, 21]. Clouds are particularly difficult to simulate in GCMs, because they result from an intricate balance between dynamical, thermodynamical and microphysical processes, that are often treated by means of parameterizations.

Due to the broad impact of clouds on the way energy and water are cycled through the atmosphere, even small changes in cloud properties can have a dramatic impact on climate [e.g. 132]. Therefore, poor simulation of present-day clouds casts doubts on the reliability of GCMs in representing cloud feedback processes in climate change projections. It is a matter of fact that cloud feedbacks constitute the primary source of uncertainty in GCMs estimates of climate sensitivity [198, 223]. The implicit assumption is that our confidence in model simulation of cloud feedbacks under climate change is proportional to how well a GCM represents the current climate [31, 170].

The effect of clouds on the sensitivity of GCMs to external perturbations is a long standing issue in climate research and has received a major boost since the study by Cess et al. [44]. Their analyses were centered around idealized experiments, where the sea surface temperature (SST) was uniformly perturbed by ± 2 K. The resulting imbalance in the radiation budget at the top-of-atmosphere (TOA) was used to evaluate the climate sensitivity of each model.

These types of intercomparisons are useful to identify the general problem areas responsible for the model disagreement, but do not give more in depth insights into the causes for such a disagreement. Indeed, differences in cloud feedbacks among the models can be due to differences in the cloud parameterizations or due to substantial differences in model structure formulation [4]. Using the same model with different parameterizations might help to unravel this issue.

Typical parameterizations include determining the fraction of the grid-box that a cloud occupies, representing convective processes and estimating the size and the number of the cloud droplets. Each of those represents a crucial challenge for climate modeling and can be identified as primary source of model biases [e.g. 32]. It has been argued that the value of the cloud feedbacks, and thus of the climate sensitivity, in the model is influenced by the details of the physical parameterizations chosen [14, 158, 233]. Therefore, parameterizations impact both climate sensitivity estimates of future climate and systematic errors of current climate simulations. Every parameterization contains one or more adjustable parameters to relate sub-grid processes to large-scale variables explicitly calculated at the grid-box scale. These param-

eters cannot often be determined on the basis of fundamental principles, but rather are carefully calibrated (tuned) to optimise the agreement between observations and simulations (e.g. ensuring the global earth's radiation balance at TOA). Tuning is part of the model developing process and arises by an inadequate representation of some climate features, in particular of clouds [229]. During the model developing process, the impact of the choice of tunable parameters on the model climate sensitivity is often not explored [e.g. 75]. However, intriguing questions arise from understanding how model shortcomings impact climate projections and to what extent radiative feedbacks are sensitive to fairly small changes in model formulation.

We aim to investigate the consequences of the cloud-related uncertainties on model biases and climate feedbacks in the EC-Earth GCM [242]. These analyses intend to make a hierarchy among the different processes contributing to the uncertainty of future climate projections, thereby providing guidance regarding necessary model developments. The dependence of various physical processes on the model formulation is assessed by analysing the response of the cloud field to an idealized climate change, simulated by different configurations of EC-Earth. Each configuration is built varying one uncertain parameter or parameterization. This type of approach is sometimes referred to as "perturbed physics ensembles" [113, 161]. Such a framework allows the physical feedback processes to be related with the parameter perturbations made within the ensemble [161]. It is the first time that analyses focus on the sensitivity of the EC-Earth model to the structure and parameter settings.

Using feedbacks as a diagnostic tool has been recognized as an essential step in understanding and constraining the future climate system response [198]. The methodology employed to estimate those is presented in section 5.2. In section 5.3 the model and the sensitivity experiments carried out are explained, along with the impact of the tunable parameters on the present-day climate simulation. Two additional sensitivity experiments, where the parameterization structure of the model is partly revised, are performed. These aim to reduce some EC-Earth biases found by Lacagnina and Selten [32]. Their effects are compared with observations in section 5.3.1. Moreover, for the first time the various radiative feedback factors in the EC-Earth model are documented (section 5.4). The physical parameterizations and regions that determine shifts in these feedbacks are identified in section 5.5. The relationship between the cloud feedback processes and the current climate states is investigated as well (section 5.5.1). Finally, we present our concluding remarks in section 5.6.

5.2 Methodology for the feedback analysis

Let Q and F be the TOA absorbed shortwave (SW) and outgoing longwave (LW) radiative fluxes, respectively, depending on a certain number of climate variables, so that $Q = Q(X)$ and $F = F(X)$. Where X represents a set of n climate variables, which may affect the radiative fluxes, such as temperature, water vapor, cloud properties and surface albedo. Suppose there are two climate states: A and B, where B is a perturbation from A obtained by changing SST. Typically, changes in SST induce changes in the other climate variables. The difference in the radiative fluxes between the two climate states may be written as:

$$\Delta Q = Q(X^B) - Q(X^A) \tag{5.1a}$$
$$\Delta F = F(X^B) - F(X^A) \tag{5.1b}$$

The radiative imbalance at TOA can be related to the change in global mean surface-air temperature (ΔT_s) through a total feedback parameter (λ):

$$\lambda = \frac{\partial(Q-F)}{\partial T_s} = \sum_{i=1}^{n} \frac{\partial(Q-F)}{\partial X_i}\frac{dX_i}{dT_s} \tag{5.2}$$

At first order, by neglecting interactions among variables, λ is commonly split as the sum of the Planck (λ_P), lapse rate (λ_l), water vapor (λ_w), surface albedo (λ_α) and cloud (λ_c) feedback parameters, plus a residual term (Re) [93]. The latter accounts for nonlinearities in the relationship between TOA radiation imbalance and ΔT_s.

Various methodologies have been proposed to separate feedbacks in climate models. Here we follow the computationally efficient radiative kernel technique [107]. In such a framework climate feedbacks are computed as products of two terms: one dependent on the climate response of a specific climate variable and the other one on the radiative transfer algorithm (kernel), which acts as a weighting function. In this framework of analysis, all clear- and all-sky feedbacks (except clouds) are derived as follows:

$$\lambda_{Xi} = \frac{\partial(Q-F)}{\partial X_i}\frac{dX_i}{dT_s} \approx K_{Xi}\frac{\Delta X_i}{\Delta T_s} \tag{5.3}$$

Each kernel (K_{Xi}) is obtained by perturbing the variable X_i by a small amount δX_i and by measuring the TOA flux response (δQ, δF). ΔX_i represents the difference in the variable X_i between two climate states, similar to Eq. 5.1. Here the two climate states are referred to as the 10-yr model predicted climate for present-day SST (A) and the 10-yr climate for SST uniformly warmer by 4 K (B). Monthly means of 3-hr data are used. As in

Soden et al. [108], tropospheric averages of the water vapor and temperature feedbacks are obtained by integrating vertically from the surface up to the tropopause, defined at 100 hPa at the equator and decreasing linearly with latitude to 300 hPa at the poles. Moreover, the employed kernels in this study are the same as in Block and Mauritsen [124][1]. The question, whether using radiative kernels from other models is appropriate, has been addressed by Soden et al. [108]. They have shown globally that the radiative kernels calculated with different models produce similar results.

Cloud feedbacks cannot be evaluated directly using the kernels approach, because of strong nonlinearities arising from the vertical overlap of clouds. A possible solution is estimating the changes in the cloud radiative effect (CRE), calculated as the difference between the clear-sky and the all-sky fluxes at TOA, normalized by ΔT_s. However, ΔCRE itself should not be interpreted as being due to changes in cloud properties alone, since it depends also on changes in the environment (water vapor, surface albedo, temperature) [93, 106]. Following Soden et al. [108], we adjust ΔCRE by correcting for non-cloud feedbacks:

$$\lambda_c = \frac{\Delta CRE}{\Delta T_s} - (\lambda_P - \lambda_P^0) - (\lambda_l - \lambda_l^0) - (\lambda_w - \lambda_w^0) - (\lambda_\alpha - \lambda_\alpha^0) \qquad (5.4)$$

where the exponent ^{0} denotes feedbacks calculated using the clear-sky kernels.

5.3 Model and simulations

The atmospheric component of the coupled ocean-atmosphere EC-Earth model version 2.3 [242] is used in isolation, such that the simulations can be considered atmosphere-only experiments. The atmosphere GCM is based on cycle 31r1 of the European Centre for Medium-Range Weather Forecasts (ECMWF) integrated forecast system (IFS) and is run at a horizontal spectral resolution of T159, with 62 levels in the vertical. More information can be found at the website: `http://ecEarth.knmi.nl`.

An International Satellite Cloud Climatology Project (ISCCP) simulator [8, 170] is employed, which outputs modeled cloud quantities using common definitions with the ISCCP observations. This removes much of the ambiguity when it comes to evaluating cloud simulations with satellite retrievals. The simulator used is part of the Cloud Feedback Model Intercomparison Project (CFMIP) Observation Simulator Package (COSP; [2]) version 1.3 (http://cfmip.metoffice.com/COSP.html). The outputs from the simulator used in this study are the following: cloud-top pressure (P_c), cloud optical

[1] Available at: `http://www.mpimet.mpg.de/en/mitarbeiter/thorsten-mauritsen.html?tx_wecstaffdirectory_pi1[curstaff]=48`.

depth (τ), high, middle and low cloud cover (defined based on P_c in hPa: $P_c \leq 440$, $440 < P_c \leq 680$ and $P_c > 680$, respectively). In addition, the Moderate Resolution Imaging Spectrometer (MODIS) simulator included in COSP is used to compare cloud droplet size with MODIS observations [215]. All these are in-cloud fraction-weighted outputs in daylight conditions only.

EC-Earth was integrated for the period from 1999 to 2008 with prescribed observed SST and sea ice, supplied by the Atmospheric Model Intercomparison Project (AMIP). We will refer to this simulation as "AMIPCTL". An additional simulation with SSTs uniformly increased by 4 K is performed for the same period and the same sea ice extent (named "AMIP4K"). These experiments follow the protocol of the Coupled Model Intercomparison Project (CMIP5; [130]). Such experiments are not intended to be representative of realistic climate change scenarios, but yet retain salient characteristics of more complex climate perturbations [37]. They have the advantage of providing a simple and computationally inexpensive framework to assess the impact of developments on the main cloud processes under climate change. In addition, a uniform SST increase ensures a large-scale forcing virtually[2] identical for every simulation [44].

Furthermore, sensitivity experiments are carried out by perturbing each time the value of one single tunable parameter in the EC-Earth reference configuration (named "REF"). This yields new EC-Earth configurations, two for each tunable parameter in Tab. 5.1 (one for increased and one for decreased value of the tunable parameter), that are integrated for the "AMIPCTL" and "AMIP4K" simulations. In the rest of the paper, a plus (minus) next to the name of the sensitivity experiment indicates increased (decreased) absolute value of the related tunable parameter. All parameters are varied within reasonable limits of physical uncertainty [e.g. 49]. These parameters are particularly interesting, because they have been used to tune this and many other GCMs [229] and have the potential to control important aspects of the cloud simulation.

In the EC-Earth model, clouds are described by prognostic equations for cloud water content and cloud fraction and are distinguished as convective or stratiform clouds [167]. The parameterization of the former is tied to the mass flux [166]. In essence, a cloud ensemble within a grid-box is approximated by one effective cloud (bulk approach), where upward-moving air is compensated by subsiding air in the cloud-free portion of the grid-box. Upward air is controlled by the mass flux, whose vertical profile depends on tunable values of the lateral mass exchange between the cloud and the environment, known as entrainment and detrainment. Indeed, the free tropospheric mois-

[2] For technical reasons, land surface temperatures are not held constant, but are allowed to change, leading to a slightly different forcing for each simulation.

Label	Parameter description	Values
ENTRPEN	Entrainment rate for penetrative and midlevel convection	[0.2,**0.8**,4.0] x 10^{-4} m^{-1}
ENTRSCV	Entrainment rate for shallow convection	[2,**3**,9] x 10^{-4} m^{-1}
RTICE	Temperature range where mixed phase is allowed to exist	[15,**23**,34.5] K
RVICE	Ice sedimentation fall speed	[0.05,**0.15**,0.45] m s^{-1}
CLCRIT[(a)]	Condensed water content threshold above which precipitation starts (for stratiform and convective clouds, respectively)	[1.5,**3**,6] x 10^{-4} kg kg^{-1} [2.5,**5**,10] x 10^{-4} kg kg^{-1}
CON[(b)]	Conversion rate from condensed water to precipitation (for stratiform and convective clouds, respectively)	[0.7,**1.4**,2.8] x 10^{-4} s^{-1} [0.7,**1.4**,2.8] x 10^{-3} s^{-1}

Table 5.1: List of perturbed parameters used in this study, where label represents the name given in the model's code. Default values for EC-Earth version 2.3 are in bold. [(a)] In the model's code labeled as: RCLCRIT for stratiform clouds and Z_CLCRIT for convective clouds. These parameters are perturbed together. [(b)] In the model's code labeled as: RKCONV for stratiform clouds and RPRCON for convective clouds. These parameters are perturbed together.

ture affects the rate at which clouds lose buoyancy through entrainment of unsaturated air into the convective column [220]. Increased lateral mass exchange reduces the buoyancy of the updraft, leading to weaker convection (Fig. 5.1a). The Tiedtke's scheme [166] distinguishes between deep, mid and shallow convection. Weaker shallow convection leads to increased amount of moisture retained in the boundary layer and so more low-clouds (Fig. 5.1b) and, by implication, stronger SWCRE. Weaker penetrative convection implies a less efficient vertical transport of heat and moisture throughout the tropical atmosphere, that manifests in a cooler and drier troposphere (Fig. 5.1c), with less high-clouds.

An additional tunable parameter involves the mixed-phase clouds. The distinction between ice and liquid water phases in EC-Earth is a function of temperature: all the liquid water present below a certain negative temperature threshold is converted into ice. Lowering the negative temperature threshold, closer to observations, leads to a drier and cooler troposphere (Fig. 5.1c), partly because of the reduced release of latent heat, and can impact the precipitation efficiency through the Bergeron-Findeisen effect. Furthermore, more supercooled water implies higher concentrations of liquid droplets, all things being equal; given the smaller size of liquid droplets relative to ice crystals, this tends to enhance cloud reflectivity, particularly at the high latitudes (Fig. 5.1d).

Two other model configurations are built varying the fall speed of the ice crystals. The rate at which ice crystals fall depends on their mass, size and shape; in EC-Earth their velocity is simply set to a constant value. Previous

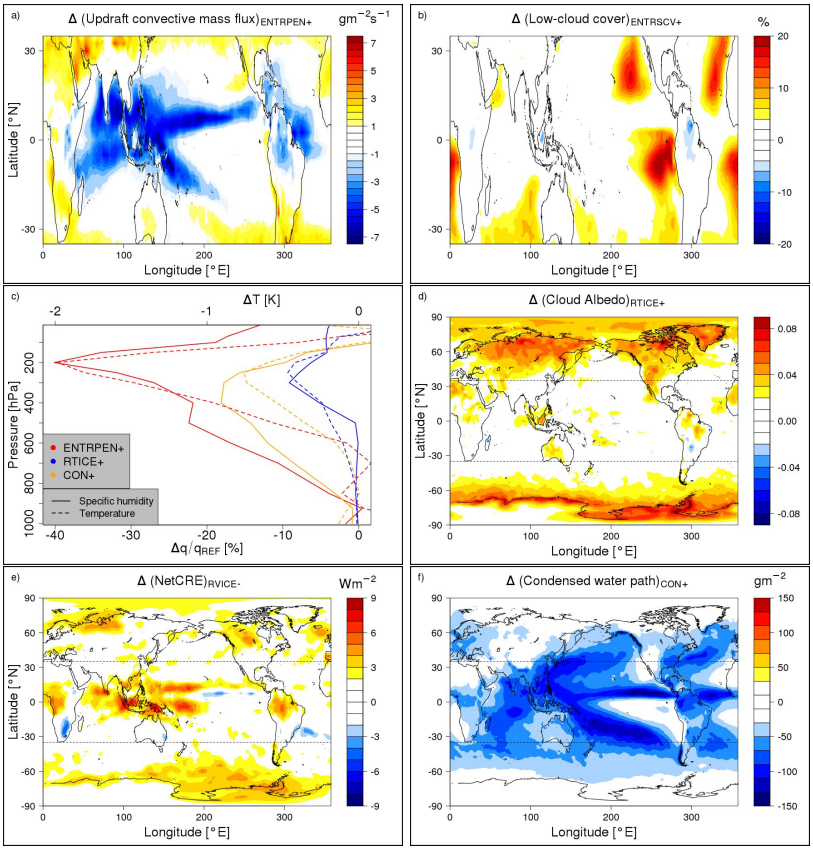

Figure 5.1: AMIPCTL experiments, period 1999-2008: absolute difference in various climate variables between sensitivity experiment outputs and reference configuration (REF) results. A plus (minus) next to the name of the sensitivity experiment indicates increased (decreased) absolute value of the related tunable parameter. a) updraft convective mass flux at 500 hPa from ENTREPEN+, b) low-level cloud cover ($P_c > 680$ hPa) from ENTRSCV+, c) vertical profiles of temperature (dashed) and specific humidity (solid) over the tropics (35 °N - 35 °S) from ENTREPEN+, RTICE+ and CON+, note that the specific humidity is plotted as fractional change expressed in percentage, d) cloud albedo from RTICE+, e) NetCRE from RVICE-, f) condensed (liquid + ice) water path from CON+. The dashed lines are ±35 ° latitude lines marking the tropical belt.

studies [139, 240] have shown that this parameter affects significantly the radiation budget of the planet. Reduced ice fall speed in our model promotes more cirrus, resulting in a less negative NetCRE, especially in the tropics (Fig. 5.1e).

Finally, the generation of precipitation (G) in EC-Earth follows the Sundqvist's parameterization [91]:

$$G \propto c_0 \left[1 - \mathrm{e}^{-\left(\frac{q_{cld}}{q_{crit}}\right)^2}\right] \tag{5.5}$$

where c_0 represents the conversion rate of condensed water (q_{cld}) to precipitation and q_{crit} is the threshold value of q_{cld} above which precipitation starts to occur. Increasing the former leads to lower cloud water content (Fig. 5.1f), less high-clouds and weaker SWCRE. Increasing the latter leads to opposite changes (not shown), but we noticed that changes in c_0 have a much broader impact on the climatology than q_{crit}, by modifying the profiles of temperature and humidity (Fig. 5.1c), hardly changed for q_{crit} experiments.

5.3.1 Revised physics experiments

Two additional EC-Earth configurations are obtained by revising the parameterization structure of the turbulent mixing and of the liquid droplet effective radius (r_{eff}). These two configurations are integrated for the "AMIPCTL" and "AMIP4K" experiments and aim to reduce biases typical of EC-Earth: too few stratocumulus and too small liquid droplets [32].

The diffusive turbulent flux of a quantity ϕ at a given model level z may be written as:

$$\overline{w'\phi'} = -K_\phi \frac{\partial \overline{\phi}}{\partial z} \tag{5.6}$$

where w is the vertical velocity. For statically stable regimes, the exchange coefficients K_ϕ in EC-Earth are computed using a revised Louis et al. [76] K-diffusion scheme. As a consequence, K_ϕ are unrealistic above the boundary layer and the turbulent mixing is too strong, promoting the erosion of stratocumulus layers from the top [176]. Recent versions of the ECMWF IFS model (Cy32r3) have reduced this bias by using Monin-Obukhov functional dependencies for K_ϕ in the free-troposphere [176]. We follow the same approach by performing a sensitivity experiment (named "TURB") with EC-Earth.

For present-day conditions (AMIPCTL), low-cloud amount from the TURB experiment agrees better with the observations, especially over the eastern basins of the tropical oceans (Figs. 5.2a-b-c). On the other hand, the positive biases get slightly larger over landmasses and Southern Hemisphere (SH) oceans with respect to the REF simulation. Increased low-cloud amount and liquid water path (not shown) reduce the model bias in SWCRE (Figs. 5.2d-e-f).

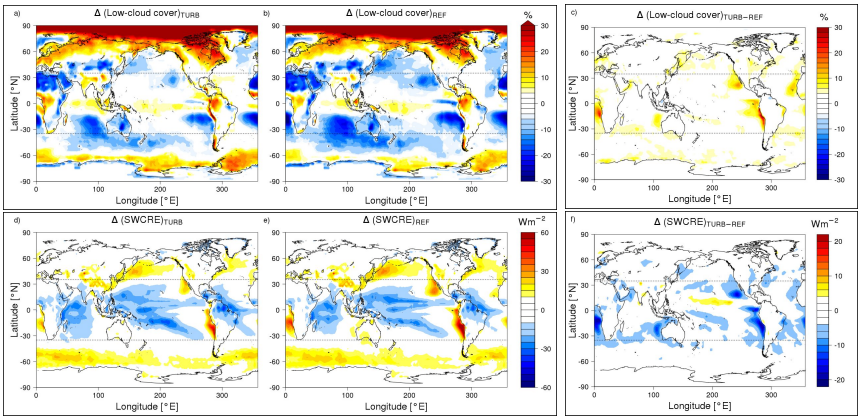

Figure 5.2: AMIPCTL experiments: difference between model and observations for 2003-2007 (positive when the EC-Earth value is higher than the satellite retrieval). (upper) Low-level cloud cover (C_{low}), (lower) SWCRE. (left) Outputs from the EC-Earth configuration with revised physics for turbulent mixing (TURB), (middle) outputs from the reference EC-Earth configuration (REF), (right) TURB-REF. Observational datasets used: ISCCP (simulator-oriented ISCCP product; [193]) and CERES (Clouds and the Earth's Radiant Energy System Energy Balanced and Filled (EBAF) TOA Ed2.7; [81]). Note that modeled cloud amounts with optical thickness below 0.3 are not considered to make a fair comparison with ISCCP retrievals.

As far as the droplet size is concerned, it is computed based on Martin et al.'s parameterization [157]. Given a constant aerosol concentration (50 cm^{-3} over ocean; 900 cm^{-3} over land), the droplet number concentration (N) is computed and then used together with the liquid water content to calculate r_{eff}. Employing constant aerosol concentration values is an oversimplification and does not account for the first aerosol indirect effect [217]. We carry out a sensitivity experiment (named "INDIRECT"), where N is related to the observed aerosol mass distributions, provided by CMIP5, through the Menon et al.'s parameterization [212] and then passed to the Martin et al.'s parameterization [157] to compute r_{eff}.

The impact of a more realistic N distribution is manifest as richer spatial structure of r_{eff} over land and as smaller r_{eff}, i.e. larger negative bias (Figs. 5.3a-b), except over the landmasses of SH (Fig. 5.3c). This implies that the aerosol concentration is tuned too high for these areas in the REF configuration. It is well-known that aerosol concentrations are much lower in the SH than in the Northern Hemisphere [e.g. 212]. Thus, assuming a constant aerosol concentration for every land areas is far from being realistic. Smaller r_{eff} translates into brighter clouds and hence stronger SWCRE (Figs. 5.3d).

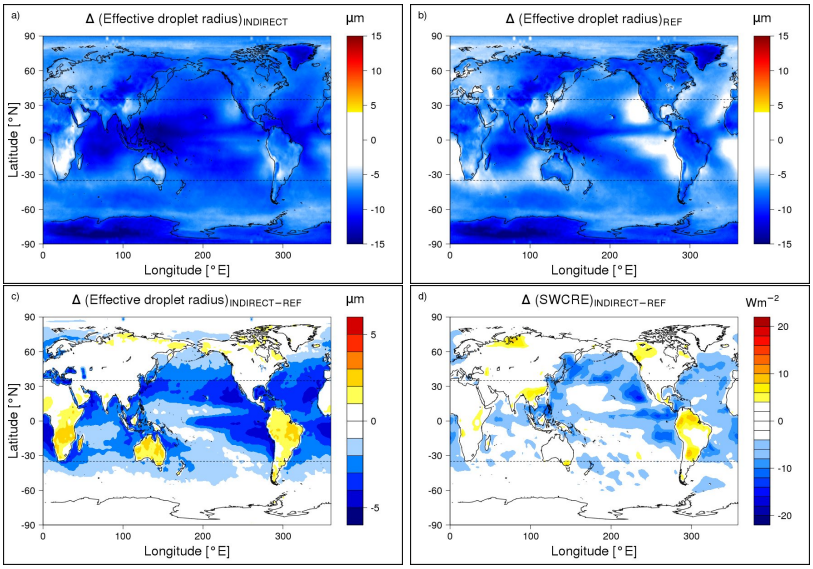

Figure 5.3: AMIPCTL experiments, period 2003-2007: model outputs are from the EC-Earth configuration with revised physics for aerosol indirect effect (INDIRECT) and from the reference EC-Earth configuration (REF). (upper) Difference between model and observations, (lower) difference between INDIRECT and REF model configurations. a)-b)-c) Effective radius of liquid droplets (r_{eff}), d) SWCRE. MODIS and CERES observations are used.

Lacagnina and Selten [32] have shown that clouds exert an overly strong cooling effect in the REF configuration. Therefore, including only these changes to account for the aerosol indirect effect degrades the radiative balance in the model. However, it is still interesting exploring the impact of this and of the other changes on the EC-Earth climate feedbacks. This is the subject of the next sections.

5.4 Radiative feedbacks in EC-Earth

Fig. 5.4 shows radiative feedbacks derived from the EC-Earth REF configuration. The effective feedback factor (λ_{eff}) is calculated using the TOA fluxes imbalance:

$$\lambda_{eff} = \frac{\Delta(Q - F)}{\Delta T_s} \tag{5.7}$$

The difference between λ^0_{eff} (as in Eq. 5.7 but for clear-sky conditions) and the total feedback factor, calculated based on clear-sky kernels, can be used

to measure the accuracy of the kernel approach [6]:

$$Re_{\%} = \left| \frac{\lambda^0_{eff} - \sum_{i=1}^{n} \frac{\partial (Q-F)^0}{\partial X_i} \frac{dX_i}{dT_s}}{\lambda^0_{eff}} \right| \cdot 100 \tag{5.8}$$

where n is the total number of kernels. The small value $Re_{\%} = 5\%$ indicates that the kernel linear approximation is reasonable for AMIP4K experiments.

High latitudes poleward of 65° are not shown in Fig. 5.4, since these regions depend strongly on surface properties and the AMIP4K runs have prescribed sea ice, that cannot respond to the warming. Because of the design of this idealized experiment, the globally averaged surface albedo feedback is quite small ($\lambda_\alpha = 0.08\ \mathrm{Wm}^{-2}/\mathrm{K}$). The only regions contributing significantly to this feedback are in the Northern Hemisphere, due to the snow melt on land.

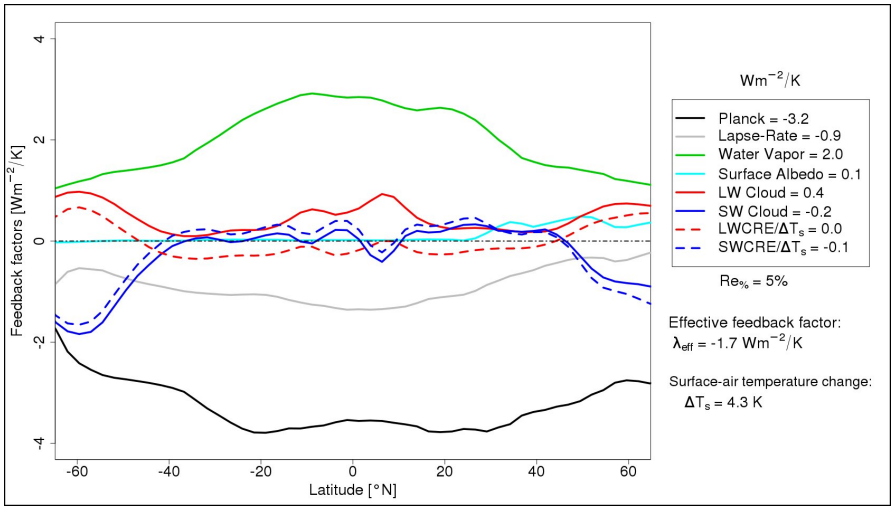

Figure 5.4: AMIP4K-AMIPCTL experiments, REF configuration: mean zonally averaged feedbacks. Global mean values are reported next to the legend, along with $Re_{\%}$, λ_{eff} and ΔT_s.

The strongest radiative feedback is associated with the Planck response (λ_P) to the warming. This is a negative feedback, since the increase in T_s implies larger amounts of outgoing longwave radiation (OLR). λ_P is the largest in the tropics owing to the great sensitivity of the Stefan-Boltzmann law to temperature.

The largest positive feedback is due to water vapor increase (λ_w) and peaks in the tropics, where the troposphere is close to saturation and temperatures are higher. The upper troposphere experiences the largest fractional

change increase in water vapor, because this region warms at a larger rate than the surface, especially in the tropics (not shown). Since the radiative effect of absorption by water vapor is roughly proportional to the logarithm of its concentration [152], the upper troposphere dominates the strength of λ_w. This connects λ_w to the lapse-rate feedback (λ_l). Indeed, λ_l tends to mirror λ_w, with the former offsetting only half of the latter in Fig. 5.4. It is worth noting that land temperatures are not constrained by a uniform increase of 4 K in this experiment and can adjust to achieve a new energy balance. The result is that landmasses warm more than oceans. Because of the different land distribution on the earth, λ_l is not symmetric between the two hemispheres.

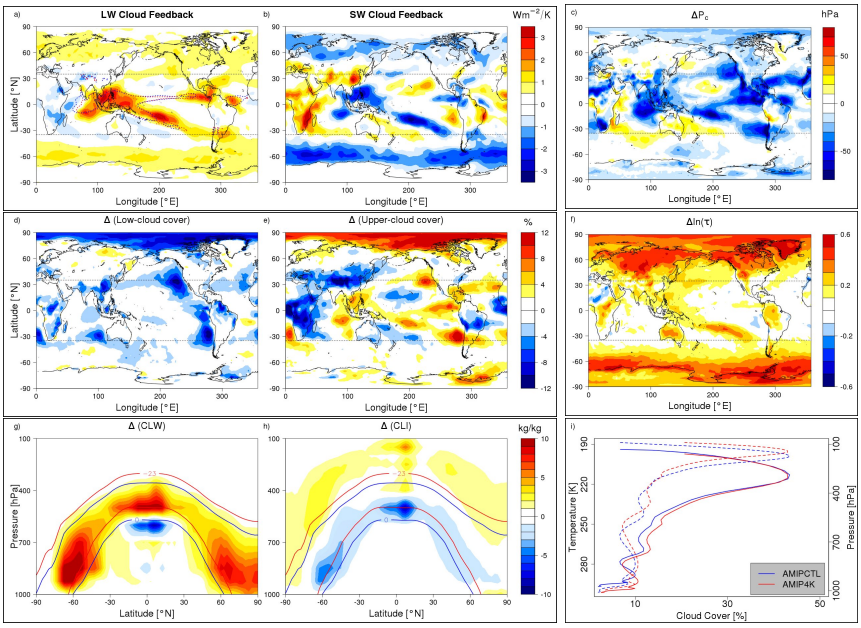

Figure 5.5: AMIP4K-AMIPCTL experiments, REF configuration: global maps of LW (a) and SW (b) cloud feedback factors. Positive values indicate energy input in the climate system. Global maps of mean change (AMIP4K-AMIPCTL) in cloud-top pressure (c), low-level cloud cover ($P_c \geq 680$ hPa) (d), upper-level cloud cover ($P_c < 680$ hPa) (e), natural logarithm of optical depth (f). Zonal mean changes in cloud liquid (g) and ice (h) water. Contour lines indicate the isotherm of 0 °C and −23 °C for current climate AMIPCTL runs (blue) and perturbed climate AMIP4K runs (red). i) Mean vertical profiles of cloud cover versus temperature (solid) and cloud cover versus pressure levels (dashed) over the tropical belt (35 °N - 35 °S) in regimes of strong convection ($\omega_{500} < -30$ hPa/day) for AMIPCTL (blue) and AMIP4K (red). These regimes are indicated by dashed lines in a).

The cloud feedback is positive in EC-Earth ($\lambda_c = 0.24$ Wm^{-2}/K) and is dominated by its LW component. Fig. 5.4 shows that correcting ΔCRE for the environmental masking effects (Eq. 5.4) enhances the cloud feedback signal, in particular its LW component. Despite λ_c and $\Delta\text{CRE}/\Delta\text{T}_s$ exhibiting similar longitudinal dependence, the global averages change sign and magnitude ($\Delta\text{CRE}/\Delta\text{T}_s = -0.05$ Wm^{-2}/K). This emphasizes that a correction for non-cloud feedbacks is relevant when studying the global cloud feedback, hence this approach is adopted in the rest of our analyses.

Spatial structure of the λ_c components is displayed in Figs. 5.5a-b. The LW λ_c is mainly positive, peaking in the west tropical Pacific. This feature is consistent with the fixed anvil temperature (FAT) hypothesis of Hartmann and Larson [133]. In the present-day climate, high-clouds enhance the natural greenhouse effect of the planet emitting less thermal radiation to space than the surface-atmosphere column would under clear-sky conditions. The reason is that these clouds radiate at a much lower temperature than the surface. The larger the temperature difference, the stronger the warming effect. According to the FAT hypothesis, deep convective clouds rise to a higher altitude in a warmer climate in such a way that the emission temperature remains nearly constant, thus LWCRE becomes stronger, hence LW λ_c is positive. The FAT hypothesis is confirmed in Fig. 5.5i for tropical regions (35 °N - 35 °S) characterized by strong convection [vertical pressure velocity at 500 hPa (ω_{500}) < -30 hPa/day, contour lines in Fig. 5.5a].

The positive LW λ_c is offset by the negative SW λ_c in deep convective areas (Fig. 5.5b). This is due to a slight increase in cloud amount (Figs. 5.5d-e) and in the natural logarithm of optical depth (Fig. 5.5f). It should be noted that $\ln(\tau)$ is linearly proportional to the cloud albedo [218]. The SW λ_c is positive over land, in particular over Africa, because of the strong decrease of the cloud amount (Figs. 5.5d-e). In contrast, the LW λ_c is negative for the same areas, but the magnitude is less than its SW counterpart. This is in agreement with the findings of Zelinka et al. [55]: changes in cloud amount have a larger impact on SW λ_c than on LW λ_c. The latter is dominated by changes in P_c (particularly for high-clouds), that are negative almost everywhere (Fig. 5.5c). Over the tropical western side of the continents, a decrease in P_c reflects cloud regime changes from low-cloud to more mid-level clouds. In these regions, the total cloudiness decreases slightly leading to a weak positive SW λ_c (Fig. 5.5b), with similar or weaker $\ln(\tau)$ (Fig. 5.5f).

The $\ln(\tau)$ exhibits the largest increase in the extra-tropics (poleward of 35 °). This feature is robust among GCMs [250] and is due to the increase in high-latitude cloud water content, dominated by the liquid phase (Figs. 5.5g-h). This model result is supported by observational [109] and analytical evidence [123]. Figs. 5.5g-h also show that the largest changes arise from

mixed-phase clouds, in regions where the temperature ranges from 0 °C to −23 °C and supercooled water is allowed to exist in the EC-Earth parameterization.

These results show that the feedback values (Fig. 5.4) derived from EC-Earth fall within the range of the feedback strengths diagnosed in the other CMIP5 models [145]. Moreover, the spatial structure of the changes in the AMIP4K experiment (Fig. 5.5) is comparable to the analysed changes in the other CMIP5 scenario simulations of Tomassini et al. [145], which supplies the argument that AMIP4K simulations are in general suitable for investigating radiative feedbacks. In order to ensure the robustness of these calculations, we have repeated them using the whole AMIP run (30-yr), instead of just the last 10 years and obtained consistent results. For instance, globally averaged for 30 years, λ_{eff} equals $-1.75\text{Wm}^{-2}/\text{K}$, while λ_{eff} is $-1.72\text{Wm}^{-2}/\text{K}$, when only the last 10 years of run are retained. This indicates that the number of years used does not materially affect our evaluation. For practical reasons only results from the last 10 years of the AMIP runs are considered in the rest of the study.

5.5 Dependence of feedbacks upon model formulation

Fig. 5.6 shows the fractional change between feedback parameters derived from the different EC-Earth configurations and the REF configuration (see section 5.3 for a detailed description of the experiments). First, note that the change in the radiative feedbacks in response to the parameter perturbations does not scale linearly with the perturbation. An extreme case regards the LW and SW λ_c in the CON experiment (Figs. 5.6d-e). An increase or decrease of the conversion rate both lead to a weakening of both the cloud feedbacks.

The total feedback parameter (Fig. 5.6a) exhibits small variations within 10%, apparently λ is fairly robust in EC-Earth. However, it is immediately clear that some tunable parameters change significantly the feedback response in the model. The impact of a decreased entrainment rate for penetrative convection (ENTREPEN-) and an increased conversion rate from condensed water to precipitation (CON+) are the most striking. Their effects on the climate feedbacks are opposite. The impact of ENTREPEN- and CON+ is relevant in every component of the total feedback, but it is relatively the largest for SW λ_c (Fig. 5.6e, note the different scales).

To understand where these large feedback differences originate, we inspect the spatial structure of the changes. As expected, ENTREPEN- has the largest impact in the deep tropics (Figs. 5.7a-b), mainly due to the stronger

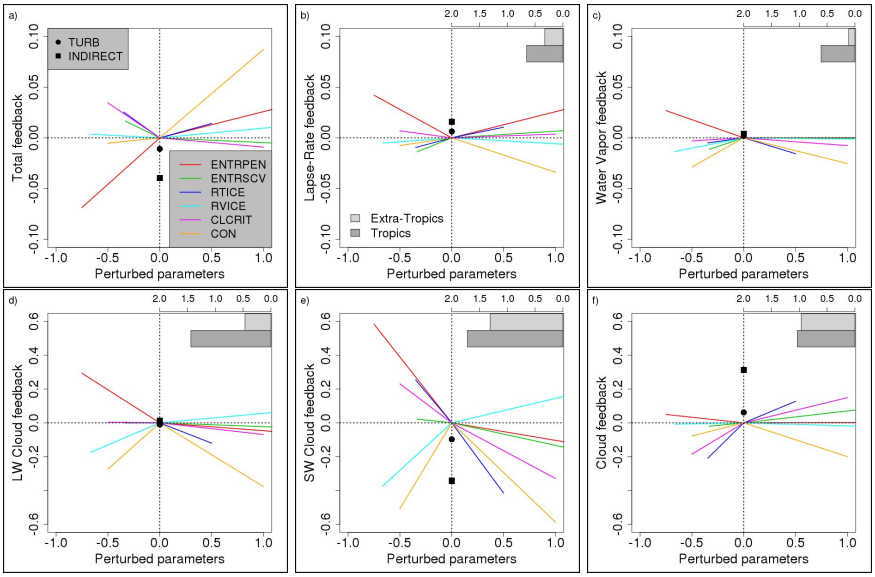

Figure 5.6: AMIP4K-AMIPCTL experiments: fractional change of perturbed parameters between different configurations of EC-Earth (indicated in the legend) and the REF configuration versus fractional change of feedback parameters between different configurations of EC-Earth and REF. The global mean feedback parameters are: effective total (a), lapse-rate (b), water vapor (c), LW cloud (d), SW cloud (e), cloud (f). On the top right of b)-c)-d)-e)-f) the inter-configuration standard deviation of the respective feedback is reported, normalized by the inter-configuration standard deviation of the effective total feedback in a) [no units]. It is separated into regional contributions from the tropics (35 °N - 35 °S) and the extra-tropics (poleward of 35 °). Feedbacks can be either positive or negative (as shown in Fig. 5.4), in any case negative (positive) values on the y-axis indicate weaker (stronger) feedback strength.

increase of upper-clouds compared to the REF configuration (Fig. 5.7c). On the other hand, $\ln(\tau)$ does not change significantly (Fig. 5.7d). The LW and the SW components of the cloud feedback tend to be anti-correlated, leading to a modest increase of λ_c (Fig. 5.6f). Similarly to ENTREPEN-, the CON+ experiment most affects the convective regions, with more emphasis on the South Pacific convergence zone (Figs. 5.8a-b). The weakening of the cloud feedbacks is mostly due to the decrease of the upper-level cloud amount in this area (Fig. 5.8c), along with the decrease of $\ln(\tau)$ (Fig. 5.8d).

The tropics contribute most to the inter-configuration standard deviation in the feedback changes, with the LW and SW λ_c exhibiting the largest spread (gray bars in Fig. 5.6). However, their combined effect, i.e. λ_c, only varies

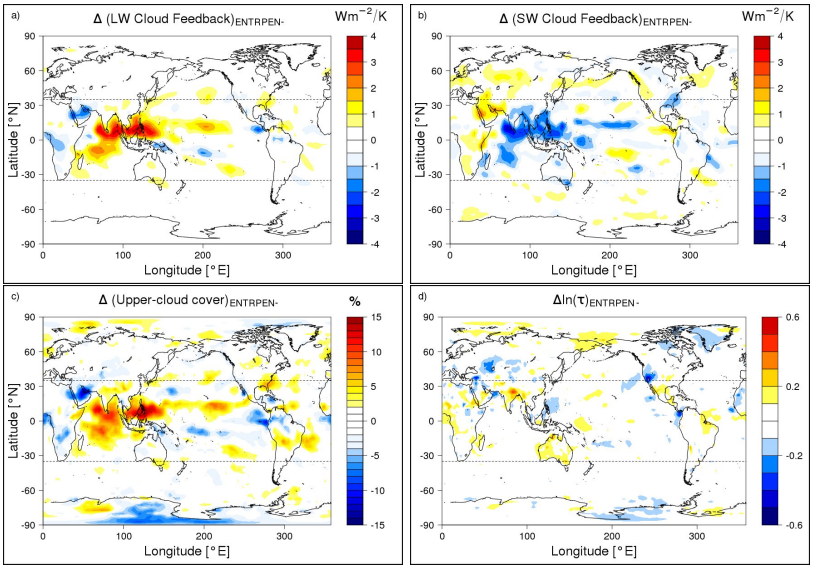

Figure 5.7: Difference between changes in AMIP4K-AMIPCTL experiments for ENTREPEN- and REF in various cloud-related variables: LW cloud feedback (a), SW cloud feedback (b), upper-level cloud cover (c), natural logarithm of optical depth (d).

within 20% and the inter-configuration standard deviation reduces, which is an indication of sizable compensating effects. An exception is the INDIRECT experiment, where λ_c increases by roughly 40%, owing to the weakening of the SW component not offset by the LW counterpart (squares in Figs. 5.6d-e-f). When AMIPCTL simulations are considered, SWCRE is more negative over the tropics and mid-latitudes in the INDIRECT configuration than in the REF configuration (Fig. 5.3d). In the AMIP4K simulations, SWCRE is less negative, as manifested in the weakening of the SW λ_c (Fig. 5.6e). The other EC-Earth configuration where the parameterization structure has been revised, namely the TURB experiment, exhibits the same shifts on the global climate feedbacks, but less pronounced. Unlike the INDIRECT configuration, SWCRE strengthens almost exclusively in the subtropical stratocumulus regions in TURB compared to REF (Fig. 5.2f), in the AMIPCTL simulations. A possible explanation is that starting with more SWCRE in present-day conditions, a reduction of cloudiness due to external forcings has a stronger impact on the SWCRE response than in a model simulating weaker SWCRE in the current climate. Therefore, regions experiencing positive SW λ_c (e.g. stratocumulus regimes in Fig. 5.5b) give rise to a stronger local SW λ_c, leading to a less negative (weaker) global SW λ_c. This hypothesis is investigated

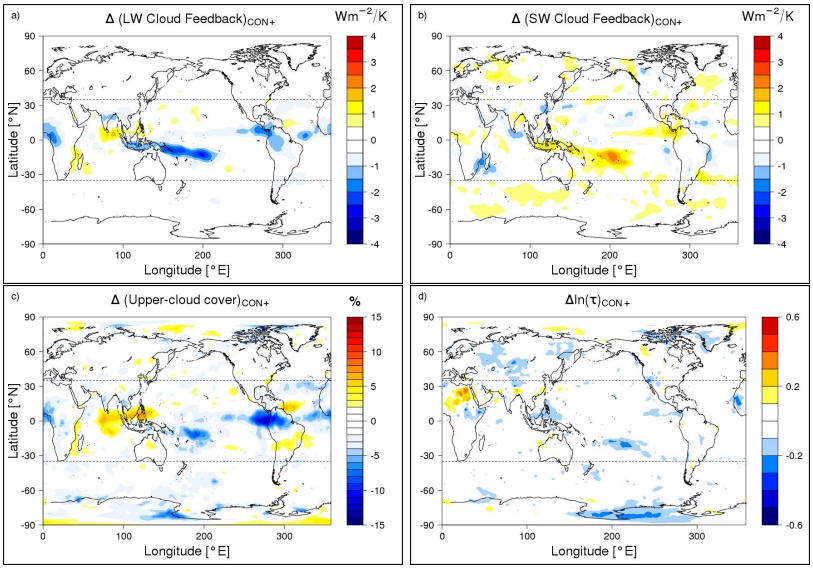

Figure 5.8: The same as in Fig. 5.7, but for the CON+ configuration instead of ENTREPEN-.

in the next subsection.

5.5.1 Any link between model bias and cloud feedbacks?

Here we analyse the response of the sensitivity experiments carried out for this study over the tropical belt (35 °N - 35 °S). This is the largest climate region of the world, roughly 50% of the earth's surface, and is the region where most of the variability in radiative feedbacks arises among the different EC-Earth configurations (gray bars in Fig. 5.6). A compositing technique centered around the ω_{500}-SST phase-space is used, following Lacagnina and Selten [39]. Monthly means of cloud-related variables are composited into different dynamical and thermodynamical regimes, defined by ω_{500} and SST. Within this framework, thick low-clouds are mostly found over relatively cold pools with large-scale sinking ($\omega_{500} > 0$) motion, while upper-level clouds are mainly expected over warmer SSTs with large-scale rising ($\omega_{500} < 0$) motion. Finally, areas of subsidence and warm SSTs are associated with trade cumulus or mostly clear sky regimes [39]. Monthly mean values of SWCRE, from the various model configurations for the AMIPCTL and AMIP4K simulations, have been composited using monthly mean values of ω_{500} and SST from the related configuration. We stress that SST is the same in every experiment, shifted back by 4 K for the AMIP4K simulations. Such a diagnostic tech-

nique is particularly convenient for AMIP experiments, since SSTs remain geographically the same and the large-scale circulation is not dramatically altered, because closely related to the spatial distribution of SST [197]. Furthermore, the information from the different cloud regimes is aggregated and the relative contribution of these regimes to the tropics-wide climate is easy to quantify.

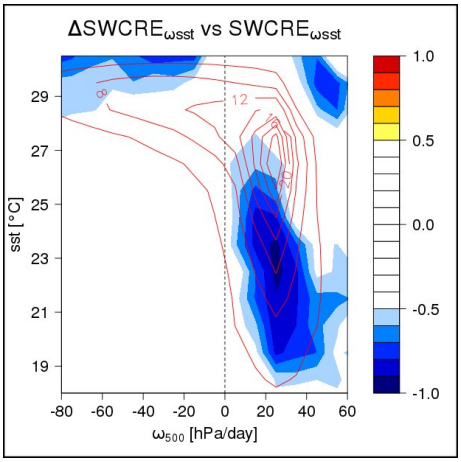

Figure 5.9: Correlation coefficient between SWCRE for AMIPCTL and its response for AMIP4K (ΔSWCRE) derived from an ensemble of model configurations described in section 5.3. The SWCRE was previously composited with respect to ω_{500} and SST over the tropical oceans (35 °N - 35 °S) derived from the related configuration. When AMIP4K runs are considered, SSTs are shifted back by 4 K to make them coincide with SSTs from AMIPCTL. Red contour lines represent the frequency of occurrence of ω_{500} and SST from the REF configuration for the AMIPCTL simulation, expressed in percentage.

Fig. 5.9 shows the correlation coefficient between SWCRE in the AMIPCTL climate and its response in the AMIP4K simulations, derived from the ensemble of sensitivity experiments described in section 5.3. The subsidence cold pool is the only region with strong correlation and high statistical frequency of occurrence. The strength of the SWCRE response to climate change is strongly correlated with the strength of the SWCRE simulated in the current climate. A possible explanation of the processes leading to such a relationship is given in Brient and Bony [73]. Simply put, low-cloud decreasing weakens the cloud-radiative cooling within the marine boundary layer (MBL), promoting less MBL relative humidity and hence amplifies the decrease of MBL low-clouds. Weaker CRE for present-day climate weakens this feedback loop, leading to a less pronounced decrease of low-clouds in a

warmer climate and thus a less pronounced weakening of CRE. Here we show that the strong correlation between the simulation of SWCRE in the current climate and its response to climate warming arises only from stratocumulus or stratocumulus to cumulus transition regimes. Other cloud regimes do not exhibit an obvious link between model simulation of present climate and future climate change. It is important to note that ΔSWCRE is fairly similar to SW λ_c in the tropics (Fig. 5.4). The former can thus be used as a surrogate of the latter for this type of analysis.

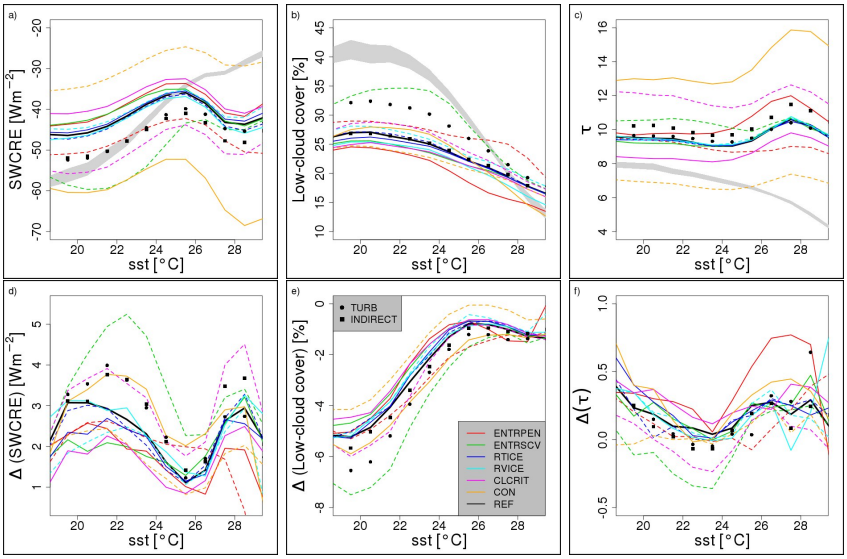

Figure 5.10: SWCRE (a and d), low-level cloud cover (b and e), optical thickness of low-clouds only (c and f), predicted by different EC-Earth configurations (reported in the legend) for the AMIPCTL simulations (upper) and their response in AMIP4K simulations (lower). Solid (dashed) lines for decreased (increased) values of the related tunable parameter. Cloud-related variables in subsidence regions ($\omega_{500} > 0$) are composited with respect to SST from AMIPCTL runs over the tropical oceans (35 °N - 35 °S). When AMIP4K runs are considered, SSTs are shifted back by 4 K to make them coincide with SSTs from AMIPCTL. Shadings represent the 95% ranges of monthly variability of observational estimates derived by CERES and ISCCP datasets. Modeled cloud amounts with optical thickness below 0.3 are not considered to make a fair comparison with the ISCCP retrievals.

We take a step further by investigating which component of the SW cloud feedback contributes to the aforementioned relationship. We use the same diagnostic technique, but compositing over subsidence regimes only. Fig. 5.10a shows SWCRE derived from AMIPCTL experiments compared with

observations (shadings). The relationship between SWCRE and SST, which is particularly strong using observations, is simulated in EC-Earth for stratocumulus regimes (lower SSTs), but breaks down for trade cumulus regions (higher SSTs). Moreover, the relationship between SWCRE and ΔSWCRE emerges notably for lower SSTs (Figs. 5.10a-d). For instance, the green dashed line, corresponding to the ENTRSCV+ configuration, exhibits much stronger SWCRE for present climate conditions than its counterpart from the REF configuration (black line in Fig. 5.10a). This corresponds to a much stronger reduction in SWCRE for AMIP4K simulations (Fig. 5.10d). Such a systematic link is more appreciable when the low-level cloud cover is considered (Figs. 5.10b-e). Model runs with higher low-cloud amount for AMIPCTL simulate larger reduction in low-clouds for AMIP4K experiments. Notably, the closer to the observations, the stronger the model sensitivity in this region. On the other hand, τ does not show a strong relationship between AMIPCTL and AMIP4K simulations (Figs. 5.10c-f). Considering the green dashed line, it falls in the middle of Fig. 5.10c, whereas it exhibits the largest decrease in τ in Fig. 5.10f. When a relationship between how model simulates current climate and how it simulates future cloud feedbacks is sought, the cloud amount and τ changes components of the SW cloud feedback behave in different ways, with the former contributing the most to this relationship. This is consistent with the hypothesis proposed by Brient and Bony [73], which is not concerned with changes in the microphysical structure of the low-clouds.

These results suggest that processes underlying the SW stratocumulus feedback are affected by the state of the model present-day climate. This implies that any model development aiming to improve the representation of stratocumulus, likely affects the SW low-cloud feedback by a factor that is proportional to the change in the stratocumulus biases. Let us consider the ENTRSCV+ experiment (green dashed line), since it exhibits the closest agreement with observations in terms of cloud cover and SWCRE. For lower SST regimes, it predicts $\Delta\text{SWCRE}/\Delta\text{T}_s \approx 1.2$ Wm^{-2}/K, implying that the reference configuration (black line) underestimates $\Delta\text{SWCRE}/\Delta\text{T}_s$ by about 30%, over the eastern basins of the tropical oceans. However, this relationship occurs in a relatively small region of the globe and contributes to, but does not dominate, the global mean SW λ_c (Fig. 5.6e).

As far as the LW λ_c is concerned, we find a relationship between high-cloud top altitude simulated in AMIPCTL and high-cloud top altitude change in AMIP4K, in deep convective regions (Fig. 5.11a). We analyse this by calculating the high-cloud top pressure as the average of the pressure values at each level weighted by the cloud amount at that level, following Zelinka and Hartmann [53]. They assumed that this high-cloud weighted pressure

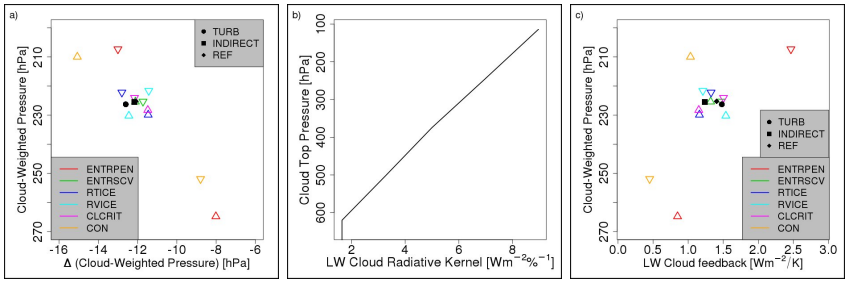

Figure 5.11: (a) Cloud-weighted pressure in present-day climate (AMIPCTL simulations) versus difference between cloud-weighted pressure in warmer climate (AMIP4K simulations) and in AMIPCTL; (b) global and annual mean LW cloud radiative kernel as a function of the cloud top pressure (CTP), equal to the sum of all the τ bins in each CTP layer in Fig. 1a of Zelinka et al. (2012a); (c) cloud-weighted pressure in AMIPCTL versus LW λ_c. Outputs in a) and c) are from the different EC-Earth model configurations reported in the legend in regimes of strong convection ($\omega_{500} < -30$ hPa/day) over the tropical belt (35 °N - 35 °S), as in Fig. 5.5i. Triangles pointing up (down) indicate increased (decreased) value of the related tunable parameter.

is a reasonable estimate of the level of the high-cloud emission temperature. Fig. 5.11a shows that the higher the clouds in the AMIPCTL experiment, the larger the rise in AMIP4K. This is relevant to the LW λ_c, because the sensitivity of OLR to a given cloud fraction increases with increasing cloud altitude [54]. If high-cloud tops were to shift toward lower pressures by the same amount for every model configuration, one would expect LW λ_c being smaller for model configurations with high-cloud tops lower in altitude in current climate. This interpretation is misleading. Indeed, summing all the τ columns along each cloud-top-pressure row of the joint histogram in figure 1a of Zelinka et al. [54], it can be shown that the LW cloud radiative kernel scales linearly with the pressure, notably below 440 hPa (Fig. 5.11b). As a consequence, given a certain cloud amount change, the same shift of high-cloud tops toward lower pressures results virtually in the same positive LW λ_c, independently of the level at which high-cloud tops are simulated in AMIPCTL.

Fig. 5.11a does not only show that different model configurations simulate high-cloud tops at different pressures in AMIPCTL, but it also shows that model configurations with high-cloud tops lower in altitude in AMIPCTL, project high-cloud top pressure changes that are systematically smaller than the other configurations. This can have an effect on LW λ_c and indeed Fig. 5.11c shows a correlation between cloud-weighted pressure in AMIPCTL and LW λ_c. However, this relationship is not as systematic as in Fig. 5.11a.

For instance, LW λ_c in the CON+ experiment (orange triangle pointing up in Fig. 5.11c) is smaller than in REF (black diamond), despite simulating high-cloud tops higher in altitude in AMIPCTL and an upward shift higher in AMIP4K with respect to REF. This implies that both the different shifts in altitude among the experiments might be too small to impact LW λ_c, and cloud amount and τ changes are not negligible in determining this feedback. These results suggest that a correlation exists between high-cloud top pressure in present-day climate and LW λ_c and more in depth investigation is needed in future studies. A compelling framework of analysis to disentangle these different influences is the compositing technique proposed in Zelinka et al. [55], where the altitude component of the LW λ_c can be investigated in isolation with respect to the cloud cover and τ changes.

5.6 Summary and discussion

Radiative feedbacks were analysed for the EC-Earth atmospheric GCM, applying the kernel approach for a 4 K uniform SST perturbation experiment (AMIP4K). We find that the kernel linear approximation can be used for such AMIP simulations, because the errors are small (roughly 5%). For the first time the various radiative feedbacks are estimated for EC-Earth. It is shown that this model predicts feedbacks in quantitative agreement with those diagnosed in the other CMIP5 models. The cloud feedback (λ_c) is calculated correcting ΔCRE for non-cloud atmospheric changes using the radiative kernels. With this method, λ_c is positive and small in EC-Earth ($\lambda_c = 0.24$ Wm^{-2}/K), with positive LW and negative SW components. When $\Delta\mathrm{CRE}/\Delta\mathrm{T}_s$ is used as a surrogate of the cloud feedback itself, it reverses the sign. Both $\Delta\mathrm{LWCRE}/\Delta\mathrm{T}_s$ and $\Delta\mathrm{SWCRE}/\Delta\mathrm{T}_s$ are smaller, but more so for $\Delta\mathrm{LWCRE}/\Delta\mathrm{T}_s$. This emphasizes that a correction for environmental masking effects is relevant, when the global cloud feedback is investigated.

We identify the nature of the cloud changes giving rise to λ_c in our model. The spatial pattern of the LW λ_c is generally positive, peaking in the west tropical Pacific. It is dominated by the general increase of the cloud-top height. The SW λ_c is generally negative and tends to offset its LW counterpart, except for the subtropical oceans, where it is positive. These regions experience moderate decrease in low-cloud amount (5% to 10%), whereas the in-cloud albedo tends to remain constant. On the other hand, the largest increase in cloud albedo stems from the extra-tropics, mainly due to increased cloud liquid water content.

These results are then compared to various EC-Earth configurations, built revising various parameterizations that impact the cloud field. These represent sensitivity experiments whose impact on the present-day and warmer cli-

mate conditions is assessed. Two sensitivity experiments concern structural changes: the reduction of the vertical diffusion in free-troposphere and the introduction of the first aerosol indirect effect in the model. Only the former leads EC-Earth to perform better compared to the observations. Stratocumulus cover increases and the SWCRE bias reduces, notably over the eastern basins of the tropical oceans. The rest of the sensitivity experiments concerns tunable parameter perturbations.

Regarding the sensitivity of the climate feedbacks in EC-Earth to the model parameter settings, we identify a number of physical processes that play a dominant role in the way clouds are simulated. Specifically, the decreased lateral mass exchange rate of penetrative convection and the increased conversion rate from condensed water to precipitation are leading parameters affecting the radiative feedbacks in EC-Earth. This supports the findings of Sanderson et al. [161], who found a strong impact of the entrainment rate in deep convection on the climate sensitivity. Here we show that the effects on the feedbacks of a decrease of the entrainment parameter are systematically offset by an increase in the conversion rate. Cloud feedbacks can clearly be identified as the main source of the inter-configuration spread in climate feedbacks, especially in the tropics. The SW component of λ_c makes a larger contribution to this spread than its LW counterpart. Perturbation, within physical uncertainties, of a number of tunable parameters can alter the SW λ_c by 60%, pointing to the existence of many degrees of freedom in this feedback.

A surprising result is that the change in the radiative feedbacks in response to the parameter perturbations does not scale linearly with the perturbation, whereas it leads to similar opposing changes in the climatology for present-day conditions. This highlights the importance of nonlinear interactions between the different processes determining the response of the climate to an external forcing. Furthermore, the total feedback parameter (λ) exhibits small variations within 10% of its reference value, indicative of its robustness in EC-Earth. This is a relatively modest change compared to the CMIP5 intermodel differences [223] and to studies centered around perturbed physics ensembles in a single GCM [49, 161]. These are based on future climate projections with changing concentrations of greenhouse gases in coupled GCMs, unlike the AMIP4K simulations considered here. When SSTs are allowed to adjust to the model settings, more degrees of freedom can affect λ. Therefore, AMIP4K sensitivity experiments are likely to underestimate the spread in the diagnosed feedback parameters. Sensitivity experiments with the fully coupled EC-Earth model and different warming scenarios should be carried out in future to unravel this discrepancy.

Moreover, it should be noticed that feedbacks calculated in this study for

AMIP4K experiments can be different in magnitude with respect to feedbacks diagnosed with other types of climate perturbations. We have performed two additional simulations with the fully coupled EC-Earth reference configuration forced once with pre-industrial levels of CO_2 and once with an abrupt quadrupling of atmospheric CO_2. These experiments are run for 150 years and global-annual means of TOA fluxes and surface-air temperatures are used to derive the climate sensitivity, similarly to Andrews et al. [223]. The equilibrium climate sensitivity is 3.4 K and $\lambda \approx -1.1$ Wm^{-2}/K in EC-Earth, values that are similar to the multimodel average (see Andrews et al. [223] for a comparison). In contrast, $\lambda \approx -1.7$ Wm^{-2}/K in the AMIP4K experiments used in this study. This supports the findings of Block and Mauritsen [124], who have shown that λ depends on the type and strength of the forcings applied to the model climate.

Finally, an important question that is relevant in tuning models to observations is whether a systematic link exists between how models perform in present-day climate and the strength of the cloud feedbacks. One might expect that with the continuing improvement of GCMs over time, models would converge in the simulation of the various climate feedbacks, but this has not proved true yet [49]. However, consistent with Brient and Bony [73], we find that the strength of the SWCRE response to climate change is strongly correlated with the strength of the SWCRE simulated in the current climate, but only in stratocumulus dominated regions. Much of this correlation for stratocumulus regimes is contributed by reduction in the low-cloud amount, rather than changes in the cloud microphysics, such as liquid water path and droplet size. These results suggest that any model development aiming to improve the representation of stratocumulus in the current climate, affects the SW low-cloud feedback by a factor that is proportional to the change in the stratocumulus biases. The reference EC-Earth configuration underestimates the SWCRE response by about 30% in these cloud regimes, compared to configurations closer to the observations.

An additional link between model bias and cloud feedbacks is also discussed. We find that certain sensitivity experiments simulate high-clouds lower in altitude in present-day conditions compared to the other experiments and this altitude difference increases in a warmer climate. This can impact the LW cloud feedback, since the sensitivity of OLR to a given cloud fraction change increases with increasing cloud altitude [54]. However, the correlation between present-day cloud altitude and LW cloud feedback is not so strong, implying that cloud amount and optical depth changes are not negligible in determining this feedback.

The results presented in this study provide guidance for future model developments and emphasize links between model fidelity and cloud feedbacks,

suggesting that observational constraints may be used to assess the credibility of these feedbacks in GCMs. Further analyses that expand these findings are warranted, such as investigating the reasons for the robust response of the total feedback to model setting changes in EC-Earth and the connection between high-cloud top altitude simulated in the present-day climate and the LW cloud feedback. Analysing this latter in other models with the appropriate framework (e.g. the partitioning technique in Zelinka et al. [55]) would help to assess the robustness of this correlation.

Acknowledgments

The research leading to these results has received funding from the European Union's Seventh Framework Program (FP7/2007-2013) under grant agreement n° 244067.
SRB data were obtained from the NASA Langley Research Center Atmospheric Science Data Center. COSP was obtained from the CFMIP website. ISCCP and MODIS data were obtained from the ftp site at IPSL (Institut Pierre Simon Laplace). Finally, we thank Jessica Vial and Karoline Block for their help with the kernel technique and Thorsten Mauritsen for making the ECHAM6 model's radiative kernels freely available online.

Chapter 6

Conclusions and outlook

Processes associated with subgrid scale clouds and the interaction between clouds, large-scale dynamics and radiation are not well understood nor well quantified in GCMs, despite being critically important in regulating the energy flow and establishing the steady state of climate.

Increasing our physical knowledge of how clouds interact with the climate system is a key requirement to improve modeling of the current and future climate. For this reason the present dissertation has begun with the analysis of the main environmental conditions that determine cloud regimes and their response to current climate variability, such as seasonal and ENSO changes. This was accomplished using mainly satellite observations and novel diagnostic techniques. This is a fundamental step for the following part of the thesis, where the ability of a GCM in reproducing the observed cloud regimes was assessed for present-day climate conditions.

Particular emphasis has been given on understanding the fundamental underlying mechanisms that regulate the interplay between clouds, radiation and large-scale circulation. Based on these mechanisms a number of fixes was proposed to improve the simulation of clouds in GCMs. The impact of these and other modifications on the model biases and climate feedbacks were evaluated in the final part of the thesis. Connections between model fidelity and the strength of the cloud feedbacks was also discussed.

6.1 Conclusions

The interaction between large-scale dynamics, clouds and radiation has been explored using observations and models. This coupling gives rise to various cloud regimes characterized by different effects on the hydrological and energetic cycle in the climate system. In the tropics, these cloud regimes can be disentangled in a ω_{500}-SST phase space. One of the main advantages of using such a bivariate approach compared to the more common spatial distribution maps is that one can easier estimate the mean relationships among different fields and quantify the relative contribution of different cloud regimes to the tropics-wide climate. Such a technique is applied with satellite observations to analyse the cloud changes in the ENSO cycle in chapter 2. The transition

of cloud and radiation properties between the resulting regimes is examined in detail. It is shown that the transition from shallow cumuli to thick upper-level clouds acts to reduce the amount of solar radiation reaching the surface, contributing to damp the warm SST anomaly during El Niño. On the other hand, the transition from stratiform low-level clouds to scattered cumuli acts as a positive feedback, which contributes to amplify the El Niño anomaly. The two opposing feedbacks coexist during the ENSO events, but they peak in different seasons. Cloud optical depth is found crucial in determining the sign of the total cloud feedback during the El Niño seasonal phase. It is shown that not all the cloud variability occurring in the ENSO cycle is associated with ω_{500} and SST changes, thus other cloud-controlling factors play a role.

To investigate the relative contribution of the meteorological parameters, which control the cloud interannual and seasonal variability, a novel diagnostic technique built on observational datasets is devised in chapter 3. The method centers on the use of the change in probability distribution functions of the environmental factors to derive the integrated changes in associated cloud properties. Changes in the humidity at surface and SST in the eastern equatorial Pacific and SLP in the western side describe most of the interannual variability in CREs and cloud cover. In addition, off the coast of California, low-cloud amount scales linearly with LTS and EIS, in accordance with other studies, but the covariation in space, within a season, is different and depends on the season. An interesting feature of this methodology is the fact that it takes into account the spatial distribution and possible nonlinear relationships between meteorological parameters and cloud-related variables. Even though such relationships do not immediately reveal causality between clouds and meteorological conditions, this framework is still particularly useful for model cloud evaluation as a constraining test for necessary associations between cloud-related quantities and the environmental factors. From a parameterization perspective, cloud properties must be represented in terms of environmental conditions computed by GCMs at each time step [116]. The GCMs can be ranked according to the sign of the simulated correlation coefficient compared to the observations, as in Clement et al. [28], and whether they can faithfully replicate to what extent an environmental parameter contributes to the observed cloud changes.

The achieved understanding of the role of clouds in the real-world climate, along with the diagnostic tools presented in chapters 2 and 3, are then employed in the cloud modeling evaluation in chapter 4. In order to avoid much of the ambiguity when it comes to assessing cloud simulations with satellite retrievals, satellite simulators are embedded in the model code. This approach is demonstrated to be imperative. A detailed evaluation of clouds and radiative fluxes has been documented for the EC-Earth GCM. The over-

estimation of the cloud optical depth overcompensates the underprediction of the total cloud cover, giving rise to an overly negative NetCRE (globally 5 W/m^2 difference between model and observations), i.e. a too strong cloud cooling effect in EC-Earth, driven by its SW component. This thesis work points to specific physical processes potentially responsible for the model biases in precipitation, cloud amount and radiative fluxes. These include the parameterization of the liquid droplet size, which is underestimated notably for trade cumuli; the temperature-dependent parameterization that distinguishes between ice and liquid water phases, which gives rise to a misrepresentation of mixed-phase clouds; the overestimated mass flux and the erroneous detrainment parameterization in the convection scheme. Finally, analyses of the relationships between meteorological conditions and cloud cover helped to identify deficiencies in the turbulence scheme, partly responsible for the lack of stratocumulus cover.

A number of parameters and processes to be adopted were suggested in order to alleviate the diagnosed biases. These motivated some of the sensitivity experiments in chapter 5. To test the effect of model uncertainties and biases on the simulation of radiative feedbacks, several configurations of the EC-Earth atmospheric GCM are built by altering the physical parameterizations. The largest code changes required were the reduction of the vertical diffusion in free-troposphere in the turbulence scheme and the introduction of the first aerosol indirect effect, that impact the simulation of the liquid droplet radii. Only the former led to improved EC-Earth simulations compared with the observations. Stratocumulus cover increases and the SWCRE bias reduces, notably over the eastern basins of the tropical oceans. It has been shown that details of the EC-Earth representation of cloud microphysical (e.g. ice fall speed and temperature range where supercooled water is allowed to exist) and convective processes (e.g. lateral mass exchange rate for shallow and deep convection) do not appear crucial for the total feedback, due to compensating effects, but are relevant for the cloud feedback, especially its SW component. Furthermore, consistent with previous studies, it is found that model configurations simulating better stratocumulus properties compared with the observations exhibit a stronger positive SW cloud feedback. In addition, connections between simulated deep convective high-cloud altitude in the present-day climate and the LW cloud feedback are discussed. These results suggest that some model biases influence the strength of the cloud feedbacks and observational constraints can be used to assess the credibility of such feedbacks in GCMs.

6.2 Outlook

It has been shown that clouds and moist processes have a profound influence on climate at both regional and planetary scales. On the other hand, these processes are a major concern for many aspects of weather modeling and climate change research. For instance, GCMs exhibit large biases in the radiative fluxes and surface temperature over the Southern Hemisphere oceans for present-day conditions [69]. Notwithstanding, all models agree on simulating a robust negative cloud feedback in this region for warming climate projections [69]. This dissertation shows that this is the case of the EC-Earth GCM as well, mostly because of biases in the SWCRE for low-clouds in current climate conditions (chapter 4) and because of cloud water content increase in a warmer climate (chapter 5). The extent to which this cloud feedback is due to dynamics (e.g. poleward shift of the storm tracks) or thermodynamics/microphysics (e.g. phase change from cloud ice to liquid, involving mixed-phase clouds parameterization) remains to be investigated.

A second line of inquiry takes into account unexplored consequences of the fixed anvil temperature (FAT) hypothesis. This hypothesis predicts a positive LW cloud feedback, particularly strong over the Pacific warm pool, and seems to be a robust feedback mechanism based on theoretical arguments and verified by models and observations [53]. In contrast, no satisfactory hypotheses have emerged so far regarding the SW cloud feedback. In the present-day climate, the tropical deep convective regions are characterized by the near cancellation between the LW and the SW CREs, i.e. N=-SWCRE/LWCRE $\approx$ 1. Chapter 3 shows that the reasons for such a behavior of N are still unknown. If this LW-SW CRE balance is not just a fortuitous coincidence, as claimed by Kiehl [225], but follows from a not immediately obvious energy constraint, then a robust mechanism for the SW cloud feedback could exist. Therefore, further analyses on the factors controlling N represent a promising starting point to elaborate hypotheses for the SW cloud feedback.

Zelinka et al. [55] have shown that GCMs disagree on the magnitude of the LW cloud feedback, even when only its altitude component is considered. The FAT hypothesis predicts that the high-cloud altitude increases in a warming climate in such a way to lead a positive LW cloud feedback. This is a robust mechanism among GCMs. The question is: why do models exhibit such a spread in the prediction of the altitude component of the LW cloud feedback? In chapter 5 it is shown that certain model configurations simulate high-clouds that are lower in altitude in present-day conditions compared to the other configurations and this altitude difference increases in a warmer climate. This can have an important impact on the LW cloud feedback, since the sensitivity of OLR to a given cloud fraction increases with increasing cloud altitude [54] and may explain the intermodel spread in this feedback. Further

analyses are warranted.

Part of the aim of this dissertation has been to look at the data in ways that are better optimized for the research questions being addressed. A number of diagnostic tools was devised, such as the environmental forcing component (EFC) technique presented in chapter 3. An appealing extension of this diagnostics would be to join it with the methodology proposed in Zelinka et al. [55]. They describe a technique for quantifying the individual contribution of the cloud amount, optical depth and cloud-top pressure changes to the cloud feedback. The resulting tool would partition the contribution of the various meteorological parameters to each of the three cloud changes aforementioned. The novel method exhibits at least two promising achievements. Firstly, it would shed light on which cloud-controlling factors are primarily responsible for the different components of the cloud feedback. Secondly, intermodel discrepancies in the impact of each environmental factor on these components may be related to specific aspects of the physical parameterizations in the models.

Finally, the EC-Earth model evaluation presented in chapters 4 and 5 can be further expanded including comparison with satellite retrievals from active sensors. This would highlight biases in the vertical structure of multi-layered cloud systems. Additional sensitivity experiments where different overlap assumptions are challenged or where the entrainment/detrainment parameterizations are made explicitly dependent on the environmental humidity are interesting extensions of the present study.

Bibliography

[1] Arakawa A. Modeling clouds and cloud processes for use in climate models. The physical basis of climate and climate modelling. *GARP Publications Series*, 16:181–197, 1975.

[2] Bodas-Salcedo A., Webb M. J., Bony S., Chepfer H., Dufresne J. L., Klein S. A., Zhang Y., Marchand R., Haynes J. M., Pincus R., and John V. O. COSP: satellite simulation software for model assessment. *Bull. Am. Meteorol. Soc.*, 92(8):1023–1043, 2011.

[3] Coakley J. A. and D. G. Baldwin. Towards the objective analysis of clouds from satellite imagery data. *J. Climate Appl. Meteor.*, 23(7):1065–1099, 1984.

[4] Colman R. A. and B. J. McAvaney. A study of general circulation model climate feedbacks determined from perturbed sea surface temperature experiments. *J. Geophys. Res.*, 102(D16):19383–19402, 1997.

[5] Emanuel K. A. A scheme for representing cumulus convection in large-scale models. *J. Atmos. Sci.*, 48:2313–2335, 1991.

[6] Jonko A, Shell K, Sanderson B, and Danabasoglu G. Climate feedbacks in CCSM3 under changing CO2 forcing. Part I: Adapting the linear radiative kernel technique to feedback calculations for a broad range of forcings. *J. Climate*, 25(15):5260–5272, 2012.

[7] Klein S. A. and D. L. Hartmann. The seasonal cycle of low stratiform clouds. *J. Clim.*, 6:1588–1606, 1993.

[8] Klein S. A. and C. Jakob. Validation and sensitivities of frontal clouds simulated by the ECMWF model. *Mon. Wea. Rev.*, 127:2514–2531, 1999.

[9] Klein S. A., Y. Zhang, M. D. Zelinka, R. Pincus, J. Boyle, and P. J. Gleckler. Are climate model simulations of clouds improving? An evaluation using the ISCCP simulator. *J. Geophys. Res. Atmos.*, 118:1329–1342, 2013.

[10] Korolev A. and P. R. Field. The effect of dynamics on mixed-phase clouds: Theoretical considerations. *J. Atmos. Sci.*, 65:66–86, 2008.

[11] Matheson M. A., Coakley J. A., and W. R. Tahnk. Aerosol and cloud property relationships for summertime stratiform clouds in the north-eastern atlantic from advanced very high resolution radiometer observations. *J. Geophys. Res.*, 110:D24204, 2005.

[12] Randall D. A. and Coauthors. Climate models and their evaluation. *Climate Change 2007: The Physical Science Basis*, S. Solomon et al., Eds., Cambridge University Press, 589-662, 2007.

[13] Rozendaal M. A., C. B. Leovy, and S. A. Klein. An observational study of diurnal variations of marine stratiform cloud. *J. Climate*, 8:1795–1809, 1995.

[14] Senior C. A. and J. F. B. Mitchell. Carbon dioxide and climate. The impact of cloud parameterization. *J. Climate*, 6:393–418, 1993.

[15] Simmons A., Uppala C, Dee D., and S. Kobayashi. ERA-Interim: New ECMWF reanalysis products from 1989 onwards. *ECMWF Newsletter No. 110*, pages 25–35, 2007.

[16] Slingo A. Sensitivity of the earthâs radiation budget to changes in low clouds. *Nature*, 343:49–51, 1990.

[17] Vecchi G. A. and B. J. Soden. Global warming and the weakening of the tropical circulation. *J. Clim.*, 20:4316–4340, 2007.

[18] Walther A. and A. Heidinger. Implementation of the Daytime Cloud Optical and Microphysical Properties algorithm (dcomp) in PATMOS-x. *J. Appl. Meteor. Climatol.*, 51:1371–1390, 2012.

[19] Bender F. A.-M., Rodhe H., Charlson R. J., Ekman A. M. L., and Loeb N. 22 views of the global albedo-comparison between 20 GCMs and two satellites. *Tellus*, 58A:320–330, 2006.

[20] Betts A.K. and A.C.M. Beljaars. Comparisons of ECMWF ISLSCP-II near-surface dataset from ERA-40 with GEWEX observational data sets. *GEWEX News, http://www.gewex.org/Feb2004.pdf*, 14(1), 2004.

[21] Lauer Axel and Kevin Hamilton. Simulating clouds with global climate models: A comparison of cmip5 results with cmip3 and satellite data. *J. Climate*, 3823-3845:26, 2013.

[22] Baker M. B. Cloud microphysics and climate. *Science*, 276:1072–1078, 1997.

[23] Rossow W. B. and R. A. Schiffer. ISCCP cloud data products. *Bull. Am. Meteorol. Soc.*, 72:2–20, 1991.

[24] Rossow W. B., A. W. Walker, D. Beuschel, and M. Roiter. International Satellite Cloud Climatology Project (ISCCP) description of new cloud datasets. *WMO/TD, 737, World Climate Research Programme (ICSU and WMO)*, pp. 115, 1996.

[25] Stevens B. Cloud-transitions and decoupling in shear-free stratocumulus topped boundary layers. *Geophys. Res. Lett.*, 27:2557–2560, 2000.

[26] Stevens B. and J.-L. Brenguier. Cloud controlling factors: Low clouds. *Heintzenberg and Charslon Eds.*, Ernst Strüngmann Forum Report, Clouds in the Perturbed Climate System: Their Relationship to Energy Balance, Atmospheric Dynamics, and Precipitation, 2009.

[27] Stevens B. and Co-authors. On entrainment in nocturnal marine stratocumulus. *Q. J. R. Meteorol. Soc.*, 129(595):3469–3492, 2003.

[28] Clement A. C., R. Burgman, and J. R. Norris. Observational and model evidence for positive low level cloud feedback. *Science*, 325:460–464, 2009.

[29] George R. C. and Wood R. Subseasonal variability of low cloud radiative properties over the Southeast Pacic Ocean. *Atmos. Chem. Phys.*, 10:4047–4063, 2010.

[30] Jakob C. The representation of cloud cover in atmospheric general circulation models. *PhD thesis, Ludwig-Maximilians-Universitaet Muenchen*, pp. 193, 2001.

[31] Lacagnina C. and F. Selten. A novel diagnostic technique to investigate cloud-controlling factors. *J. Geophys. Res. Atmos.*, 118:5979–5991, 2013.

[32] Lacagnina C. and F. Selten. Evaluation of clouds and radiative fluxes in the EC-Earth general circulation model. *Climate Dynamics*, 2014.

[33] Lewellen D. C., W. S. Lewellen, and S. Yoh. Influence of Bowen ratio on boundary layer cloud structure. *J. Atmos. Sci.*, 53:175–187, 1996.

[34] Ou S. C. and K.-N. Liou. Ice microphysics and climatic temperature feedback. *Atmos. Res.*, 35:127–138, 1995.

[35] Wang C. and J. Picaut. Understanding ENSO physics - A review. *Geophys. Monogr., Amer. Geophys. Union*, 147:21–48, 2004.

[36] Wyant M. C. and Coauthors. The PreVOCA experiment: Modeling the lower troposphere in the southeast Pacific. *Atmos. Chem. Phys.*, 10:4757–4774, 2010.

[37] Wyant Matthew C., Bretherton ChristopherS., Bacmeister JulioT., Kiehl Jeffrey T., Held Isaac M., Zhao Ming, Klein Stephen A., and Soden Brian J. A comparison of low-latitude cloud properties and their response to climate change in three AGCMs sorted into regimes using mid-tropospheric vertical velocity. *Climate Dynamics*, 27(2-3):261–279, 2006.

[38] Ma C.-C., C. R. Mechoso, A. W. Robertson, and A. Arakawa. Peruvian stratus clouds and the tropical Pacific circulation: A coupled ocean-atmosphere GCM study. *J. Climate*, 9:1635–1645, 1996.

[39] Lacagnina Carlo and F. Selten. Changes in the cloud properties in response to El Niño: a bivariate approach. *Climate Dynamics*, 40(11-12):2973–2991, 2013.

[40] National Research Council. Learning to predict climate variations associated with El Niño and the Southern Oscillation. *National Academy Press*, pp. 171, 1996.

[41] Bretherton C.S., Roode S.R. de, Jakob C., Andreas E.L., Intrieri J., Moritz R.E., and Persson P.O.G. A comparison of the ECMWF forecast model with observations over the annual cycle at SHEBA. *J. Geophys. Res., Volume: FIRE Arctic Clouds Experiment Special Issue*, 2000.

[42] Cess R. D. and Coauthors. Interpretation of cloud climate feedback is produced by 14 atmospheric general circulation models. *Science*, 245:513–516, 1989.

[43] Cess R. D. and Coauthors. Cloud feedback in atmospheric general circulation models: An update. *J. Geophys. Res.*, 101(D8):12791–12794, 1996.

[44] Cess R. D. and et al. Intercomparison and interpretation of climate feedback processes in 19 atmospheric general circulation models. *J. Geophys. Res.*, 95(D10):16601–16615, 1990.

[45] Cess R. D., M. Zhang, P. Wang, and B. A. Wielicki. Cloud structure anomalies over the tropical Pacific during the 1997/98 El Niño. *Geophys. Res. Lett.*, 28(24):4547–4550, 2001.

[46] Cess R. D., M. Zhang, B. A. Wielicki, D. F. Young, X-L. Zhou, and Y. Nikitenko. The influence of the 1998 El Niño upon cloud-radiative forcing over the pacific warm pool. *J. Clim.*, 14(9):2129–2137, 2001.

[47] Del Genio A. D. Representing the sensitivity of convective cloud systems to tropospheric humidity in general circulation models. *Surv. Geophys.*, 33:637–656, 2012.

[48] Kim D., A. H. Sobel, and I.-S. Kang. A mechanism denial study on the Madden-Julian Oscillation. *J. Adv. Model. Earth Syst.*, 3:M12007, 2011.

[49] Klocke D., Pincus R., and Quaas. On constraining estimates of climate sensitivity with present-day observations through model weighting. *J. Climate*, 24:6092–6099, 2011.

[50] Lebsock Matthew D., Christian Kummerow, and Graeme L. Stephens. An observed tropical oceanic radiativeâconvective cloud feedback. *J. Climate*, 23:2065–2078, 2010.

[51] Rodgers C. D. Retrieval of atmospheric temperature and composition from remote measurements of thermal radiation. *Rev. Geophys.*, 14(4):609–624, 1976.

[52] Rotstayn Leon D. Climate sensitivity of the CSIRO GCM: Effect of cloud modeling assumptions. *J. Clim.*, 12:334–356, 1999.

[53] Zelinka M. D. and D. L. Hartmann. Why is longwave cloud feedback positive? *J. Geophys. Res.*, 115:D16117, 2010.

[54] Zelinka Mark D., Stephen A. Klein, and Dennis L. Hartmann. Computing and partitioning cloud feedbacks using cloud property histograms. Part I: Cloud radiative kernels. *J. Climate*, 25:3715–3735, 2012.

[55] Zelinka Mark D., Stephen A. Klein, and Dennis L. Hartmann. Computing and partitioning cloud feedbacks using cloud property histograms. Part II: Attribution to changes in cloud amount, altitude, and optical depth. *J. Climate*, 25:3736–3754, 2012.

[56] Zelinka Mark D., Stephen A. Klein, Karl E. Taylor, Timothy Andrews, Mark J. Webb, Jonathan M. Gregory, and Piers M. Forster. Contributions of different cloud types to feedbacks and rapid adjustments in CMIP5. *J. Climate*, 26:5007–5027, 2013.

[57] Sun D.-Z. and Coauthors. Radiative and dynamical feedbacks over the equatorial cold tongue: Results from nine atmospheric GCMs. *J. Clim.*, 19:4059–4074, 2006.

[58] Sun D.-Z., J. Fasullo, T. Zhang, and A. Roubicek. On the radiative and dynamical feedbacks over the equatorial Pacific cold tongue. *J. Clim.*, 16:2425–2432, 2003.

[59] Sun D.-Z., Yu Y., and Zhang T. Tropical water vapor and cloud feedbacks in climate models: A further assessment using coupled simulations. *Journal of Climate*, 2(5):1287–1304, 2009.

[60] Enfield DB. Evolution and historical perspective of the 1997-1998 El Niño-Southern Oscillation event. *Bull. Mar. Sci.*, 69:7–25, 2001.

[61] de Rooy Wim C. and A. Pier Siebesma. A simple parameterization for detrainment in shallow cumulus. *Mon. Wea. Rev.*, 136:560–576, 2008.

[62] de Szoeke S. P., Y. Wang, S.-P. Xie, and T. Miyama. Effect of shallow cumulus convection on the eastern pacific climate in a coupled model. *Geophys. Res. Lett.*, 33:L17713, 2006.

[63] Back L. E. Towards an improved understanding of deep convection patterns over the tropical oceans. *Ph.D. Thesis, University of Washington*, page pp. 100, 2007.

[64] Guilyardi E., P. Braconnot, F.-F. Jin, S. T. Kim, M. Kolasinski, T. Li, and I. Musat. Atmosphere feedbacks during ENSO in a coupled GCM with a modified atmospheric convection scheme. *J. Climate*, 22:5698–5718, 2009.

[65] Kay J. E. and Coauthors. Exposing global cloud biases in the Community Atmosphere Model (CAM) using satellite observations and their corresponding instrument simulators. *J. Climate*, 25:5190–5207, 2012.

[66] Kessler E. On the distribution and continuity of water substance in atmospheric circulation. *Meteorological Monographs, Vol. 10. Am. Meteorol. Soc., Boston, MA*, 1969.

[67] Trenberth K. E. The definition of El Niño. *Bulletin of the American Meteorological Society*, 78:2771–2777, 1997.

[68] Trenberth K. E. and D. P. Stepaniak. Co-variability of components of poleward atmospheric energy transports on seasonal and interannual timescales. *J. Climate*, 16:3691–3705, 2003.

[69] Trenberth Kevin E. and John T. Fasullo. Simulation of present-day and twenty-first-century energy budgets of the southern oceans. *J. Climate*, 23:440–454, 2010.

[70] Waliser D. E. Formation and limiting mechanism for very high SST: Linking the dynamics and thermodynamics. *J. Climate*, 9:161–188, 1996.

[71] Waliser D. E. and N. E. Graham. Convective cloud systems and warm-pool SSTs: Coupled interactions and self-regulation. *J. Geoph. Res.*, 98:12881–12893, 1993.

[72] Zebiak S. E. and M. A. Cane. A model El Niño-Southerrn Oscillation. *Mon. Wea. Rev.*, 115:2262–2278, 1987.

[73] Brient F. and S. Bony. How may low-cloud radiative properties simulated in the current climate influence low-cloud feedbacks under global warming? *Geophys. Res. Lett.*, 39:L20807, 2012.

[74] Harrison E. F., P. Minnis, B. R. Barkstrom, V. Ramanathan, R. D. Cess, and G.G. Gibson. Seasonal variation of cloud radiative forcing derived from the Earth Radiation Budget Experiment. *J. Geophys. Res.*, 95:18687–18703, 1990.

[75] Hourdin F. and Co-authors. Impact of the LMDZ atmospheric grid configuration on the climate and sensitivity of the IPSL-CM5A coupled model. *Clim. Dyn.*, 40:2167–2192, 2013.

[76] Louis J. F., Tiedtke M., and Geleyn J.-F. A short history of the operational PBL parametrization at ECMWF. *In Proc. ECMWF Workshop on Boundary Layer Parametrization, November 1981, ECMWF, Reading, UK*, pp. 59-80, 1982.

[77] Ryan B. F. and Co-authors. Simulations of a cold front by cloud-resolving, limited-area, and large-scale models, and a model evaluation using in situ and satellite observations. *Mon. Weather Rev.*, 128:3218–3235, 2000.

[78] Chang FL. and ZQ Li. A new method for detection of cirrus overlapping water clouds and determination of their optical properties. *J. Atm. Sciences*, 62:3993–4009, 2005.

[79] Y. Fouquart and B. Bonnel. Computations of solar heating of the earth's atmosphere: A new parameterization. *Beitr. Phys. Atmos.*, 53:35–62, 1980.

[80] Charney J. G. Carbon dioxide and climate: A scientific assessment. *National Academy Press*, 33 pp, 1979.

[81] Loeb N. G., B. A. Wielicki, D. R. Doelling, G. L. Smith, D. F. Keyes, S. Kato, N. Manalo-Smith, and T. Wong. Toward optimal closure of the earth's top-of-atmosphere radiation budget. *Journal of Climate*, 22(3):748–766, 2009.

[82] Madec G. NEMO ocean engine. *Note du Pole de modelisation, Institut Pierre-Simon Laplace (IPSL), France, No. 27*, pages 1288–1619, 2008.

[83] Chepfer H., S. Bony, D. Winker, G. Cesana, J. L. Dufresne, P. Minnis, C. J. Stubenrauch, , and S. Zeng. The GCM-Oriented CALIPSO Cloud Product (CALIPSO-GOCCP). *J. Geophys. Res.*, 115:D00H16, 2010.

[84] Derbyshire S. H., Maidens A. V., Milton S. F., Stratton R. A., and Willett M. R. Adaptive detrainment in a convective parametrization. *Q.J.R. Meteorol. Soc.*, 137:1856–1871, 2011.

[85] Kawai H. and J. Teixeira. Probability density functions of liquid water path and cloud amount of marine boundary layer clouds: Geographical and seasonal variations and controlling meteorological factors. *J. Climate*, 23:2079–2092, 2010.

[86] Riehl H., T. C. Yeh, J. S. Malkus, and N. E. La Seur. The north-east trade of the pacific ocean. *Quart. J. Roy. Meteor. Soc.*, 77:598–626, 1951.

[87] Schneider S. H. Cloudiness as a global climatic feedback mechanism: The effects on the radiation balance and surface temperature of variations in cloudiness. *J. Atmos. Sci.*, 29:1413–1422, 1972.

[88] Sobel A. H., J. Nilsson, and L. M. Polvani. The weak temperature gradient approximation and balanced tropical moisture waves. *J. Atmos. Sci.*, 58:3650–3665, 2001.

[89] Stone P. H. and J. H. Carlson. Atmospheric lapse rate regimes and their parameterization. *J. Atmos. Sci.*, 36:415–423, 1979.

[90] Su H., J. H. Jiang, D. G. Vane, , and G. L. Stephens. Observed vertical structure of tropical oceanic clouds sorted in large-scale regimes. *Geophys. Res. Lett.*, 35:L24704, 2008.

[91] Sundqvist H. A parameterization scheme for non-convective condensation including prediction of cloud water content. *Q. J. R. Meteorol. Soc.*, 104:677–690, 1978.

[92] Sundqvist H., E. Berge, and J. E. Kristjansson. Condensation and cloud parameterization studies with a mesoscale numerical weather prediction model. *Mon. Wea. Rev.*, 117:1641–1657, 1989.

[93] Zhang M. H., J. J. Hack, J. T. Kiehl, and R. D. Cess. Diagnostic study of climate feedback processes in atmospheric general circulation models. *J. Geophys. Res.*, 99(D3):5525–5537, 1994.

[94] Barker HW, Stephens GL, and Fu Q. The sensitivity of domain-averaged solar fluxes to assumptions about cloud geometry. *Quarterly Journal of the Royal Meteorological Society*, 125:2127–2152, 1999.

[95] Sandu I., B. Stevens, and R. Pincus. On the transitions in marine boundary layer cloudiness. *ACP*, 10:2377–2391, 2010.

[96] Cox S. J., P. W. Stackhouse Jr., S. K. Gupta, J. C. Mikovitz, M. Chiacchio, and T. Zhang. The NASA/GEWEX surface radiation budget project: Results and analysis, in IRS 2004: Current problems in atmospheric radiation. *Proceedings of the International Radiation Symposium, Busan, Korea, 23 - 28 August 2004, edited by H. Fischer and B.-J. Soon*, p. 419, 2004.

[97] Hansen J., A. Lacis, D. Rind, G. Russell, P. Stone, I. Fung, R. Ruedy, and J. Lerner. Climate sensitivity: Analysis of feedback mechanisms. *Climate Processes and Climate Sensitivity, AGU Geophysical Monograph 29, Maurice Ewing Vol. 5. J.E. Hansen, and T. Takahashi, Eds. American Geophysical Union*, pages 130–163, 1984.

[98] Heymsfield A. J. Properties of tropical and midlatitude ice cloud particle ensembles: Part I: Median mass diameters and terminal velocities. *J. Atmos. Sci.*, 60:2592–2611, 2003.

[99] Lloyd J., E. Guilyardi, and H. Weller. The role of atmosphere feedbacks during ENSO in the CMIP3 models. Part II: Using AMIP runs to understand the heat flux feedback mechanisms. *Climate Dyn.*, 37:1271–1292, 2011.

[100] Lloyd J., E. Guilyardi, and H. Weller. The role of atmosphere feedbacks during ENSO in the CMIP3 models. Part III: The shortwave flux feedback. *J. Clim.*, 25:4275–4293, 2012.

[101] Lu J., G. Chen, and D. M. W. Frierson. Response of the zonal mean atmospheric circulation to El Niño versus global warming. *J. Clim.*, 21:5835–5851, 2008.

[102] Morcrette J. J., S. A. Clough, E. J. Mlawer, and M. J. Iacono. Impact of a validated radiative transfer scheme, RRTM, on the ECMWF model climate and 10-day forecasts. *ECMWF Technical Memo No. 252*, pp. 47, 1998.

[103] Murphy J., Sexton D. H., Barnett D. N., Jones G. S., Webb M. J., Collins M., and Stainforth D. A. Quantification of modelling uncertainties in a large ensemble of climate change simulations. *Nature*, 430:768–772, 2004.

[104] Simpson J. On cumulus entrainment and one-dimensional models. *J. Atmos. Sci.*, 28:449–455, 1971.

[105] Simpson J., C. Kummerow, W. K. Tao, and R. F. Adler. On the Tropical Rainfall Measuring Mission (TRMM). *Meteor. Atmos. Phys.*, 60:19–36, 1996.

[106] Soden Brian J., Anthony J. Broccoli, and Richard S. Hemler. On the use of cloud forcing to estimate cloud feedback. *J. Climate*, 17:3661–3665, 2004.

[107] Soden Brian J. and Isaac M. Held. An assessment of climate feedbacks in coupled ocean-atmosphere models. *J. Clim.*, 19:3354–3360, 2006.

[108] Soden Brian J., Isaac M. Held, Robert Colman, Karen M. Shell, Jeffrey T. Kiehl, and Christine A. Shields. Quantifying climate feedbacks using radiative kernels. *J. Clim.*, 21:3504–3520, 2008.

[109] Somerville R. C. J. and L. A. Remer. Cloud optical thickness feedbacks in the CO2 climate problem. *J. Geophys. Res.*, 89(D6):9668–9672, 1984.

[110] Stubenrauch C. J., W. B. Rossow, S. Kinne, S. Ackerman, G. Cesana, H. Chepfer, L. Di Girolamo, B. Getzewich, A. Guignard, A. Heidinger, B. C. Maddux, W. P. Menzel, P. Minnis, C. Pearl, S. Platnick, C. Poulsen, J. Riedi, S. Sun-Mack, A. Walther, D. Winker, S. Zeng, and G. Zhao. Assessment of global cloud datasets from satellites: Project and database initiated by the GEWEX radiation panel. *Bull. Amer. Meteor. Soc.*, 2012.

[111] Vial J., Dufresne J.-L., and Bony S. On the interpretation of inter-model spread in CMIP5 climate sensitivity estimates. *Clim. Dyn.*, 41:3339–3362, 2013.

[112] Wang J. and W. B. Rossow. Effects of cloud vertical structure on atmospheric circulation in the GISS GCM. *J. Clim.*, 11:3010–3029, 1998.

[113] Webb M. J. and Coauthors. On the contribution of local feedback mechanisms to the range of climate sensitivity in two gcm ensembles. *Climate Dyn.*, 27:17–38, 2006.

[114] Yuan J., D. L. Hartmann, and R. Wood. Dynamic effects on the tropical cloud radiative forcing and radiation budget. *J. Climate*, 21:2337–2351, 2008.

[115] Yuan J. and D.L. Hartmann. Spatial and temporal dependence of clouds and their radiative impacts on the large-scale vertical velocity profile. *J. Geophys. Res.*, 113:D19201, 2008.

[116] Zhang Guang J., Andrew M. Vogelmann, Michael P. Jensen, William D. Collins, and Edward P. Luke. Relating satellite-observed cloud properties from MODIS to meteorological conditions for marine boundary layer clouds. *J. Clim.*, 23:1374–1391, 2010.

[117] Morcrette J.-J. and Y. Fouquart. The overlapping of cloud layers in shortwave radiation parameterizations. *J. Atmos. Sci.*, 43:321–328, 1986.

[118] Dufresne J.-L. and S. Bony. An assessment of the primary sources of spread of global warming estimates from coupled atmosphere-ocean models. *J. Climate*, 21(19):5135–5144, 2008.

[119] Houze R. A. Jr. *Cloud Dynamics.* Academic Press, pp. 576, 1993.

[120] Stackhouse P. W. Jr., S. J. Cox, S. K. Gupta, M. Chiacchio, and J. C. Mikovitz. The WCRP/GEWEX surface radiation budget project release 2: An assessment of surface fluxes at 1 degree resolution. *In International Radiation Symposium, St.-Petersburg, Russia, July 24 - 29, IRS 2000: Current Problems in Atmospheric Radiation, edited by W. L. Smith and Y. Timofeyev*, p. 147, 2001.

[121] Stackhouse PW Jr, Gupta SK, Cox SJ, Zhang T, Mikovitz JC, and Hinkelman LM. 24.5-year SRB data set released. *GEWEX News*, 21:10–12, 2011.

[122] Hurrell J.W. and G.G. Campbell. Monthly mean global satellite data sets available in CCM history tape format. *NCAR Technical Note NCAR/TN-371+STR*, 1992.

[123] Betts A. K. and Harshvardan. Thermodynamic constraint on the cloud liquid water feedback in climate models. *J. Geophys. Res.*, 92D:8483–8485, 1987.

[124] Block K. and T. Mauritsen. Forcing and feedback in the MPI-ESM-LR coupled model under abruptly quadrupled CO2. *J. Adv. Model. Earth Syst.*, 5:676–691, 2013.

[125] Krueger S. K., McLean, G. T., and Fu Q. Numerical simulation of the stratus-to-cumulus transition in the subtropical marine boundary layer. Part I: Boundary-layer structure. *J. Atmos. Sci.*, 52:2839–2850, 1995.

[126] Wyrtki K. El Niño - The dynamic response of the equatorial Pacific Ocean to atmospheric forcing. *J. Phys. Oceanogr.*, 5:572–584, 1975.

[127] Emanuel KA, Neelin JD, and Bretherton CS. On large-scale circulations in convecting atmospheres. *Q. J. R. Meteorol. Soc.*, 120:1111–1143, 1994.

[128] Williams KD, Ringer MA, and Senior CA. Evaluating the cloud response to climate change and current climate variability. *Clim. Dyn.*, 20:705–721, 2003.

[129] Williams K.D., M.A. Ringer, C.A. Senior, M.J. Webb, B.J. McAvaney, N. Andronova, S. Bony, J.-L. Dufresne, S. Emori, R. Gudgel, T. Knutson, B. Li, K. Lo, I. Musat, J. Wegner, A. Slingo, and J.F.B. Mitchell. Evaluation of a component of the cloud response to climate change in an intercomparison of climate models. *Clim. Dyn.*, 26:145–165, 2006.

[130] Taylor KE, Stouffer RJ, and Meehl GA. An overview of CMIP5 and the experiment design. *Bull Amer Meteor Soc*, 93:485–498, 2012.

[131] Dhuria H. L. and H. L. Kyle. Cloud types and the tropical earth radiation budget. *J. Clim.*, 3:1409–1434, 1990.

[132] Hartmann D. L. and D. Doelling. On the net radiative effectiveness of clouds. *J. Geophys. Res.*, 96(D1):869–891, 1991.

[133] Hartmann D. L. and K. Larson. An important constraint on tropical cloud-climate feedback. *Geophys. Res. Lett.*, 29:1951, 2002.

[134] Hartmann D. L., L. A. Moy, and Q. Fu. Tropical convection and the energy balance at the top of the atmosphere. *J. Climate*, 14:4495–4511, 2001.

[135] Hartmann D. L., B.-M. E. Ockert, and M. L. Michelsen. The effect of cloud type on earth's energy balance: Global analysis. *J. Clim.*, 5:1281–1304, 1992.

[136] Hartmann Dennis L. *Global Physical Climatology*. Academic Press, 411 pp., 1994.

[137] Kubar T. L., D. L. Hartmann, and R. Wood. Radiative and convective driving of tropical high clouds. *J. Climate*, 20:5510–5526, 2007.

[138] Kuo H. L. and W. H. Raymond. A quasi-one-dimensional cumulus cloud model and parametrization of cumulus heating and mixing effects. *Mon. Wea. Rev.*, 108:991–1009, 1980.

[139] Mitchell D. L., P. Rasch, D. Ivanova, G. McFarquhar, and T. Nousiainen. Impact of small ice crystal assumptions on ice sedimentation rates in cirrus clouds and GCM simulations. *Geophys. Res. Lett.*, 35:L09806, 2008.

[140] Stephens G. L. Radiation profiles in extended water clouds. II: Parameterization schemes. *J. Atmos. Sci.*, 35:2123–2132, 1978.

[141] Stephens G. L. Radiative effects of clouds and water vapor. *Global Energy and Water Cycles, K. A. Browing, and R. J. Gurney, Eds., Cambridge University Press.*, pages 71–90, 1999.

[142] Stephens G. L. and Coauthors. The CloudSat mission and the A-train: A new dimension of space-based observations of clouds and precipitation. *Bull. Amer. Meteor. Soc.*, 83:1771–1790, 2002.

[143] Stephens G. L. and C. M. R. Platt. Aircraft observations of the radiative and microphysical properties of stratocumulus and cumulus cloud fields. *J. Clim. Appl. Meteorol.*, 26:1243–1269, 1987.

[144] Stephens Graeme L. Cloud feedbacks in the climate system: A critical review. *J. Climate*, 18:237–273, 2005.

[145] Tomassini L., O. Geoffroy, J.-L. Dufresne, A. Idelkadi, C. Cagnazzo, K. Block, T. Mauritsen, M. Giorgetta, and J. Quaas. The respective roles of surface temperature driven feedbacks and tropospheric adjustment to CO2 in CMIP5 transient climate simulations. *Climate Dynamics*, 41:3103–3126, 2013.

[146] Yu L., X. Jin, and R. A. Weller. Multidecade global flux datasets from the Objectively Analyzed Air-sea Fluxes (OAFlux) project: Latent and sensible heat fluxes, ocean evaporation, and related surface meteorological variables. *Woods Hole Oceanographic Institution, OAFlux Project Technical Report. OA-2008-01, Woods Hole. Massachusetts*, pp. 64, 2008.

[147] Wang Lei, Yuqing Wang, Axel Lauer, and Shang-Ping Xie. Simulation of seasonal variation of marine boundary layer clouds over the eastern pacific with a regional climate model. *J. Climate*, 24:3190–3210, 2011.

[148] Beljaars A. C. M. and P. Viterbo. The role of the boundary layer in a numerical weather prediction model. *In A. A. M. Holtslag and P. G. Duynkerke (Eds), Clear and Cloudy Boundary Layers, North Holland Publishers*, 1999.

[149] Collins M., R. Knutti, J. Arblaster, J.-L. Dufresne, T. Fichefet, P. Friedlingstein, X. Gao, W.J. Gutowski, T. Johns, G. Krinner, M. Shongwe, C. Tebaldi, A.J. Weaver, and M. Wehner. Long-term climate change: Projections, commitments and irreversibility. in: Climate change 2013: The physical science basis. contribution of working group i to the fifth assessment report of the intergovernmental panel on climate change. *Cambridge University Press, Cambridge, United Kingdom and New York, NY, USA.*, 2013.

[150] Forbes R. M. and A. Tompkins. An improved representation of cloud and precipitation. *ECMWF Newsletter No. 129*, pages 13–18, 2011.

[151] Haynes J. M., R. T. Marchand, Z. Luo, A. Bodas-Salcedo, and G. L. Stephens. A multipurpose radar simulation package: Quickbeam. *Bull. Amer. Meteor. Soc.*, 88:1723–1727, 2007.

[152] Held I. M. and B. J. Soden. Water vapor feedback and global warming. *Annu. Rev. Energy Environ.*, 25:441–475, 2000.

[153] Held Isaac M. and Brian J. Soden. Robust responses of the hydrological cycle to global warming. *J. Climate*, 19:5686–5699, 2006.

[154] Kanamitsu M., W. Ebisuzaki, J. Woollen, S.K. Yang, J.J. Hnilo, M. Fiorino, and G. Potter. NCEP-DOE AMIP-II reanalysis. *Bull. Am. Met. Soc.*, 83:1631–1643, 2002.

[155] Köhler M. Improved prediction of boundary layer clouds. *ECMWF Newsletter*, 104, ECMWF, Shinfield Park, Reading RG2 9AX, UK., 2005.

[156] Lau K. M., C. H. Sui, M. D. Chou, and W. K. Tao. An inquiry into the cirrus cloud thermostat effect for tropical sea surface temperature. *Geophys. Res. Lett.*, 21:1157–1160, 1994.

[157] Martin G. M., D. W. Johnson, and A. Spice. The measurement and parameterization of effective radius of droplets in warm stratocumulus clouds. *J. Atmos. Sci.*, 51:1823–1842, 1994.

[158] Naud C. M., A. D. Del Genio, and M. Bauer. Observational constraints on the cloud thermodynamic phase in midlatitude storms. *J. Climate*, 19:5273–5288, 2006.

[159] Nieuwstadt F. T. M. The turbulent structure of the stable, nocturnal boundary layer. *J. Atmos. Sci.*, 41:2202–2216, 1984.

[160] Rauber R. M. and A. Tokay. An explanation for the existence of supercooled water at the top of cold clouds. *J. Atmos. Sci.*, 48:1005–1023, 1991.

[161] Sanderson B. M., K.M. Shell, and W.J. Ingram. Climate feedbacks determined from radiative kernels in a multi-thousand member ensemble of AOGCMs. *Clim. Dyn.*, 35(7-8):1219–1236, 2010.

[162] Sekiguchi M. and Co-authors. A study of the direct and indirect effects of aerosols using global satellite data sets of aerosol and cloud parameters. *J. Geophys. Res.*, 108, 2003.

[163] Shell Karen M., Jeffrey T. Kiehl, and Christine A. Shields. Using the radiative kernel technique to calculate climate feedbacks in NCAR's community atmospheric model. *J. Clim.*, 21:2269–2282, 2008.

[164] Smith T. M. and R. W. Reynolds. Improved extended reconstruction of SST (1854-1997). *J. Climate*, 17:2466–2477, 2004.

[165] Tiedtke M. Parameterization of cumulus convection in large-scale models. *Physically-Based Modelling and Simulation of Climate and Climatic Change NATO ASI Series, M. E. Schlesinger*, pages 375–431, 1988.

[166] Tiedtke M. A comprehensive mass flux scheme for cumulus parametrization in large-scale models. *Mon. Wea. Rev.*, 117:1779–1800, 1989.

[167] Tiedtke M. Representation of clouds in large-scale models. *Mon. Weather Rev.*, 121:3040–3061, 1993.

[168] Tompkins A. M. The parameterization of cloud cover. *ECMWF Technical Memorandum*, p. 23. Available at http://www.ecmwf.int/publications/, 2005.

[169] Wallace J. M. Effect of deep convection on the regulation of tropical sea surface temperature. *Nature*, 357:230–231, 1992.

[170] Webb M., C. Senior, S. Bony, and J.-J. Morcrette. Combining ERBE and ISCCP data to assess clouds in the Hadley Centre, ECWMF and LMD atmospheric climate models. *Climate Dyn.*, 17:905–922, 2001.

[171] Wyant M., Bretherton C., Rand H., and Stevens D. Numerical simulations and a conceptual model of the subtropical marine stratocumulus to trade cumulus. *J. Atmos. Sci.*, 54:168–192, 1997.

[172] Ockert-Bell ME and Hartmann DL. The effect of cloud type on earth's energy balance: results for selected regions. *J. Clim.*, 5:1158–1171, 1992.

[173] Liou K. N. *An introduction to atmospheric radiation.* Academic Press. Second edition, pp. xiv + 583, 2002.

[174] Allan R. P., Slingo A., and Ringer M. A. Influence of dynamics on the changes in tropical cloud radiative forcing during the 1998 el niño. *J. Clim.*, 15:1979–1986, 2002.

[175] Bechtold P., E. Bazile, F. Guichard, P. Mascart, and E. Richard. A mass-flux convection scheme for regional and global models. *Quart. J. Roy. Meteor. Soc.*, 127:869–886, 2001.

[176] Bechtold P., Köhler M., Jung T., Leutbecher M., Doblas-Reyes F., Rodwell M. J., Vitart F., and Balsamo G. Advances in simulating atmospheric variability with the ECMWF model: From synoptic to decadal time-scales. *Quarterly Journal of the Royal Meteorological Society*, 134:1337–1351, 2008.

[177] Charlock T. P. and V. Ramanathan. The albedo field and cloud radiative forcing produced by a general circulation model with internally generated cloud optics. *J. Atmos. Sci.*, 42:1405–1429, 1985.

[178] Lock A. P., Brown A. R., Bush M. R., Martin, G. M., and Smith R. N. B. A new boundary layer mixing scheme. Part I: Scheme description and single-column model tests. *Mon. Wea. Rev.*, 128:3187–3199, 2000.

[179] Shonk J. K. P., R. J. Hogan, and J. Manner. Impact of improved representation of horizontal and vertical cloud structure in a climate model. *Clim. Dyn.*, 38:2365–2376, 2012.

[180] Siebesma A. P. and Coauthors. Cloud representation in general circulation models over the northern Pacific Ocean: AEUROCS intercomparison study. *Quart. J. Roy. Meteor. Soc.*, 130:3245–3267, 2004.

[181] Siebesma A. P. and J. W. M. Cuijpers. Evaluation of parametric assumptions for shallow cumulus convection. *J. Atmos. Sci.*, 52:650–666, 1995.

[182] Viterbo P., Beljaars A. C. M., Mahouf J.-F., and Teixeira J. The representation of soil moisture freezing and its impact on the stable boundary layer. *Q. J. R. Meteorol. Soc.*, 125:2401–2426, 1999.

[183] Zhu P., Hack J.J., Kiehl J.T., and Bretherton C.S. Climate sensitivity of tropical and subtropical marine low cloud amount to ENSO and global warming due to doubled CO2. *J. Geophys. Res.*, 112:D17108, 2007.

[184] Siebesma A. Pier and J. Teixeira Pedro M. M. Soare and. A combined eddy-diffusivity mass-flux approach for the convective boundary layer. *J. Atmos. Sci.*, 64:1230–1248, 2007.

[185] Bennartz R. Global assessment of marine boundary layer cloud droplet number concentration from satellite. *J. Geophys. Res.*, 112:D02201, 2007.

[186] Chen R., R. Wood, Z. Li, R. Ferraro, and F.-L. Chang. Studying the vertical variation of cloud droplet effective radius using ship and spaceborne remote sensing data. *J. Geophys. Res.*, 113:D00A02, 2008.

[187] Colman R. A comparison of climate feedbacks in gcms. *Climate Dyn.*, 20:865–873, 2003.

[188] Marchand R. and T. Ackerman. An analysis of cloud cover in multiscale modeling framework global climate model simulations using 4 and 1 km horizontal grids. *J. Geophys. Res.*, 115:D16207, 2010.

[189] Marchand R., T. Ackerman, M. Smyth, and W. B. Rossow. A review of cloud top height and optical depth histograms from MISR, ISCCP, and MODIS. *J. Geophys. Res.*, 115:D16206, 2010.

[190] Norris J. R. Low cloud type over the ocean from surface observations. Part II: geographical and seasonal variations. *J. Clim.*, 11:383–403, 1998.

[191] Norris Joel R. and Conway B. Leovy. Interannual variability in stratiform cloudiness and sea surface temperature. *J. Climate*, 7:1915–1925, 1994.

[192] Pincus R. and Baker M. B. Effect of precipitation on the albedo susceptibility of clouds in the marine boundary layer. *Nature*, 372:250–252, 1994.

[193] Pincus R., S. Platnick, S. A. Ackerman, R. S. Hemler, and R. J. P. Hofmann. Reconciling simulated and observed views of clouds: MODIS, ISCCP, and the limits of instrument simulators. *J. Clim.*, 25:4699–4720, 2012.

[194] Wood R. and Bretherton C. S. On the relationship between stratiform low cloud cover and lower-tropospheric stability. *J. Clim.*, 19(24):6425–6432, 2006.

[195] Adler R.F., G.J. Huffman, A. Chang, R. Ferraro, P. Xie, J. Janowiak, B. Rudolf, U. Schneider, S. Curtis, D. Bolvin, A. Gruber, J. Susskind, and P. Arkin. The version 2 Global Precipitation Climatology Project (GPCP) monthly precipitation analysis (1979-present). *J. Hydrometeor.*, 4:1147–1167, 2203.

[196] Marchand Roger and Thomas Ackerman. A cloud-resolving model with an adaptive vertical grid for boundary layer clouds. *J. Atmos. Sci.*, 68:1058–1074, 2011.

[197] Lindzen R.S. and S. Nigam. On the role of sea surface temperature gradients in forcing low level winds and convergence in the tropics. *J. Atmos. Sci.*, 44:2418–2436, 1987.

[198] Bony S., R. Colman, V. M. Kattsov, R. P. Allan, C. S. Bretherton, J.-L. Dufresne, A. Hall, S. Hallegatte, M. M. Holland, W. Ingram, D. A. Randall, D. J. Soden, G. Tselioudis, and M. J. Webb. How well do we understand and evaluate climate change feedback processes? *J. Clim.*, 19:3445–3482, 2006.

[199] Bony S. and J-L Dufresne. Marine boundary layer clouds at the heart of cloud feedback uncertainties in climate models. *Geophys. Res. Lett.*, 32:L20806, 2005.

[200] Bony S., J.-L. Dufresne, H. LeTreut, and J.-J. Morcrette. On dynamic and thermodynamic components of cloud changes. *Climate Dyn.*, 22:71–86, 2004.

[201] Bony S, Lau K-M, and Sud YC. Sea surface temperature and large-scale circulation influences on tropical greenhouse effect and cloud radiative forcing. *J. Clim.*, 10:2055–2077, 1997.

[202] Bretherton C. S. A conceptual model of the stratus-trade cumulus transition in the subtropical oceans. *Proc. 11th Int. Conf. on Clouds and Precipitation, Vol. 1, Montreal, PQ, Canada, Int. Comm. on Clouds and Precip. and Int. Assoc. Meteor. Atmos. Physics*, pages 374–377, 1992.

[203] Bretherton C. S. and Co-authors. An intercomparison of radiatively-driven entrainment and turbulence in a smoke cloud, as simulated by different numerical models. *Q. J. R. Meteorol. Soc.*, 125:391–423, 1999.

[204] Bretherton C. S. and Hartmann D. L. Large-scale controls on cloudiness, in: Perturbed clouds in the climate system: Their relationship to energy balance, atmospheric dynamics and precipitation. *Heintzenberg and Charslon Eds.*, Ernst Strüngmann Forum Report, Clouds in the Perturbed Climate System: Their Relationship to Energy Balance, Atmospheric Dynamics, and Precipitation:217–234, 2009.

[205] Bretherton C. S., Uttal T., Fairall C. W., Yuter S. E., Weller R. A., Baumgardner D., Comstock K., Wood R., and Raga G. B. The Epic 2001 stratocumulus study. *B. Am. Meteorol. Soc.*, 85:967–977, 2004.

[206] Bretherton C. S. and M. C. Wyant. Moisture transport, lower-tropospheric stability, and decoupling of cloud-topped boundary layers. *J. Atmos. Sci.*, 54:148–167, 1997.

[207] Curtis S., A. Salahuddin, R. F. Adler, G. J. Huffman, G. Gu, and Y. Hong. Precipitation extremes estimated by GPCP and TRMM: ENSO relationships. *J. Hydrometeor.*, 8:678–689, 2007.

[208] Kato S., N. G. Loeb, F. G. Rose, D. R. Doelling, D. A. Rutan, T. E. Caldwell, L. Yu, , and R. A. Weller. Surface irradiances consistent with CERES-derived top-of-atmosphere shortwave and longwave irradiances. *Journal of Climate*, 26:2719–2740, 2013.

[209] Lindzen R. S., M.-D. Chou, and A. Y. Hou. Does the earth have an adaptive infrared iris? *Bull. Amer. Meteor. Soc.*, 82:417–432, 2001.

[210] Malkus J. S. Some results of a trade-cumulus cloud investigation. *J. Meteor.*, 11:220–237, 1954.

[211] Mauger Guillaume S. and Joel R. Norris. Assessing the impact of meteorological history on subtropical cloud fraction. *J. Climate*, 23:2926–2940, 2010.

[212] Menon S., A.D. Del Genio, D. Koch, and G. Tselioudis. GCM simulations of the aerosol indirect effect: Sensitivity to cloud parameterization and aerosol burden. *J. Atmos. Sci.*, 59:692–713, 2002.

[213] Park S. and Leovy C. B. Marine low-cloud anomalies associated with ENSO. *J. Clim.*, 17:3448–3469, 2004.

[214] Platnick S. Vertical photon transport in cloud remote sensing problems. *J. Geophys. Res.*, 105:22919–22935, 2000.

[215] Platnick S, MD King, SA Ackerman, WP Menzel, BA Baum, JC Riedi, and RA Frey. The MODIS cloud products: Algorithms and examples

from Terra. *IEEE Transaction Geosciences Remote Sensings*, 41:459–473, 2003.

[216] Solomon S. and Coauthors. Climate change 2007: the physical science basis: contribution of Working Group I to the Fourth Assessment Report of the Intergovernmental Panel on Climate Change. *Cambridge University Press. ISBN 0521705967*, 2007.

[217] Twomey S. Pollution and planetary albedo. *Atmos. Environ.*, 8:1251–1256, 1974.

[218] Twomey S. The influence of pollution on the shortwave albedo of clouds. *J. Atmos. Sci.*, 34:1149–1152, 1977.

[219] Valcke S. OASIS3 user guide (prism 2-5). *CERFACS technical report TR/CMGC/06/73, PRISM Report No 3, Toulouse, France*, pp. 60, 2006.

[220] Bony Sandrine and Kerry A. Emanuel. On the role of moist processes in tropical intraseasonal variability: Cloud-radiation and moisture-convection feedbacks. *J. Atmos. Sci.*, 62:2770–2789, 2005.

[221] Derbyshire S.H., I. Beau, P. Bechtold, J.-Y.Grandpeix, J.-M. Piriou, J.-L. Redelsperger, and P. M. M. Soares. Sensitivity of moist convection to environmental humidity. *Quart. J. Roy. Meteor. Soc.*, 130:3055–3079, 2004.

[222] Uppala S.M. and Coauthors. The ERA-40 re-analysis. *Q. J. R. Meteorol. Soc.*, 131:2961–3012, 2005.

[223] Andrews T., J. M. Gregory, M. J. Webb, and K. E. Taylor. Forcing, feedbacks and climate sensitivity in CMIP5 coupled atmosphere-ocean climate models. *Geophys. Res. Lett.*, 39:L09712, 2012.

[224] Evan A. T., A. K. Heidinger, and D. J. Vimont. Arguments against a physical long-term trend in global ISCCP cloud amounts. *Geophys. Res. Lett.*, 34:L04701, 2007.

[225] Kiehl J. T. On the observed near cancellation between longwave and shortwave forcing in tropical regions. *J. Clim.*, 7:559–565, 1994.

[226] Kiehl J. T. and V. Ramanathan. Comparison of cloud forcing derived from the Earth Radiation Budget Experiment with the NCAR community climate model. *J. Geophys. Res.*, 95(D8):11679–11698, 1990.

[227] Koenigk T, Brodeau L, Graversen RG, Karlsson J, Svensson G, Tjernstrom M, Willen U, and Wyser K. Arctic climate change in 21st century CMIP5 simulations with EC-Earth. *Clim Dyn.*, 40(11):2719–2743, 2013.

[228] Marchand R. T., G. G. Mace, and T. P. Ackerman. Hydrometeor detection using CloudSat-an earth orbiting 94 ghz cloud radar. *J. Atmos. Oceanic. Technol.*, 25:519–533, 2008.

[229] Mauritsen T. and Co-authors. Tuning the climate of a global model. *J. Adv. Model. Earth Syst.*, 4:M00A01, 2012.

[230] Nitta T. Observational determination of cloud mass flux distributions. *J. Atmos. Sci.*, 32:73–91, 1975.

[231] Pierrehumbert R. T. Thermostats, radiator fins, and the local runaway greenhouse. *J. Atmos. Sci.*, 52:1784–1806, 1995.

[232] Wetherald R. T. and S. Manabe. Cloud feedback process in a general circulation model. *Journal of Atmospheric Sciences*, 45:1397–1415, 1988.

[233] Yokohata T., S. Emori, T. Nozawa, Y. Tsushima, T. Ogura, and M. Kimoto. Climate response to volcanic forcing: Validation of climate sensitivity of a coupled atmosphere-ocean general circulation model. *Geophys. Res. Lett.*, 32:L21710, 2005.

[234] Nordeng T.-E. Extended versions of the convection parametrization scheme at ECMWF and their impact upon the mean climate and transient activity of the model in the tropics. *ECMWF Tech. Memo. No. 206*, 1994.

[235] Stocker T.F. and Coauthors. Physical climate processes and feedbacks. *In J.T. Houghton, et al.. Climate Change 2001: The Scientific Basis, Contributions of Working Group I to the Third Assessment Report of the Intergovernmental Panel on Climate Change. Cambridge, U.K.: Cambridge University Press*, 2001.

[236] Bjerknes V. Saturated-adiabatic ascent of air through dry-adiabatically descending environment. *Quart. J. Roy. Meteor. Soc.*, 64:325–330, 1938.

[237] Ramanathan V., L. Callis, R. Cess, J. Hansen, I. Isaksen, W. Kuhn, A. Lacis, F. Luther, J. Mahlman, R. Reck, and M. Schlesinger. Climate-chemical interactions and effects of changing atmospheric trace gases. *Rev. Geophys.*, 25:1441–1482, 1987.

[238] Ramanathan V., R. D. Cess, E. F. Harrison, P. Minnis, B. R. Barkstrom, E. Ahmad, and D. L. Hartmann. Cloud-radiative forcing and climate: Results from the Earth Radiation Budget Experiment. *Science*, 243:57–63, 1989.

[239] Ramanathan V. and W. Collins. Thermodynamic regulation of ocean warming by cirrus clouds deduced from observations of the 1987 El Niño. *Nature*, 351:27–32, 1991.

[240] Grabowski Wojciech W. Cloud microphysics and the tropical climate: Cloud-resolving model perspective. *J. Climate*, 13:2306–2322, 2000.

[241] Hazeleger W., C. Severijns, T. Semmler, S. Stefanescu, S. Yang, X. Wang, K. Wyser, E. Dutra, R. Bintanja, B. van den Hurk, T. van Noije, F. Selten, A. Sterl, and Co-authors. EC-Earth: A seamless Earth-system prediction approach in action. *Bull. Amer. Meteor. Soc.*, 91:1357–1363, 2010.

[242] Hazeleger W., X. Wang, C. Severijns, S. Stefanescu, R. Bintanja, A. Sterl, K. Wyser, T. Semmler, S. Yang, B. van den Hurk, T. van Noije, E. van der Linden, and K. van der Wiel. EC-Earth V2.2: description and validation of a new seamless Earth system prediction model. *Clim. Dyn.*, 39:2611–2629, 2012.

[243] Lin W., M. Zhang, and N. G. Loeb. Seasonal variation of the physical properties of marine boundary layer clouds off the california coast. *J. Climate*, 22:2624–2638, 2009.

[244] Nam Christine C. W. and Johannes Quaas. Evaluation of clouds and precipitation in the ECHAM5 general circulation model using CALIPSO and CloudSat satellite data. *J. Climate*, 25:4975–4992, 2012.

[245] Spencer R. W. and W. D. Braswell. How dry is the tropical free troposphere? Implications for global warming theory. *Bull. Amer. Meteor. Soc.*, 78:1097–1106, 1997.

[246] Rossow W.B. and R.A. Schiffer. Advances in understanding clouds from ISCCP. *Bull. Amer. Meteorol. Soc.*, 80:2261–2288, 1999.

[247] Greuell Wouter, Erik van Meijgaard, Nicolas Clerbaux, and Jan Fokke Meirink. Evaluation of model-predicted top-of-atmosphere radiation and cloud parameters over Africa with observations from GERB and SEVIRI. *J. Climate*, 24:4015–4036, 2011.

[248] Hu Y., S. Rodier, K. Xu, W. Sun, J. Huang, B. Lin, P. Zhai, and D. Josset. Occurrence, liquid water content, and fraction of supercooled water clouds from combined CALIOP/IIR/MODIS measurements. *J. Geophys. Res.*, 115:D00H34, 2010.

[249] Jin Y., W.B. Rossow, and D.P. Wylie. Comparison of the climatologies of high-level clouds from HIRS and ISCCP. *J. Climate*, 9:2850–2879, 1996.

[250] Tsushima Y. and Coauthors. Importance of the mixed-phase cloud distribution in the control climate for assessing the response of clouds to carbon dioxide increase: A multi-model study. *Climate Dyn.*, 27:113–126, 2006.

[251] Zhang Y-C., W.B. Rossow, A.A. Lacis, M.I. Mishchenko, and V. Oinas. Calculation of radiative fluxes from the surface to top-of-atmosphere based on ISCCP and other global datasets: Refinements of the radiative transfer model and the input data. *J. Geophys. Res.*, page 109, 2004.

[252] Zhang Z. and S. Platnick. An assessment of differences between cloud effective particle radius retrievals for marine water clouds from three MODIS spectral bands. *J. Geophys. Res.*, 116:D20215, 2011.

Acknowledgements

The one person I could never thank enough is my daily adviser Frank Selten: he taught me many things in science and life and helped me to successfully finish this thesis. His confidence and support have been indispensable. I am also grateful to him for critically reading my manuscripts, which have greatly benefited from his valuable suggestions and constructive criticism. Secondly, I want to thank my promoter Pier Siebesma for his essential help and patience. The overview he had over my work has been source of inspiration throughout these four years. I am grateful to the KNMI for the friendly atmosphere, which made work a nice place to be. The time I have been spending has turned out very useful, both from a scientific and personal perspective. I am indebted to all the people at KNMI who gave a great contribution to this work by discussing with me. Among others, I cannot help but mention Sara Dal Gesso, my office mate throughout four years, she started this adventure with me, we shared several travels, concerns and funny moments together. Thanks to Jelle van den Berk and Eveline van der Linden for their suggestions on my manuscripts and their help in translating the summary and the propositions of this thesis in Dutch. I would also like to express my gratitude to Brigitta Kamphuis for her administrative and logistics help and her tireless cheerful smile.

A heartfelt thank to those who helped my stay in the Netherlands a time worth living. With you, this challenge became a pleasant great experience. I enjoyed the annual meetings with the participants of the EUCLIPSE project a lot. Many of them are not only very enthusiastic researchers, but are also a great company. In particular I want to thank Solange Fermepin and Gregory Cesana for making our workshops pleasant and worthwhile. Last, but not least, a special thank to my family and longstanding friends, who have been believing and encouraging me despite the distance. And I should not forget to thank Marco Simeoni and his skills in design, since without him the cover of this thesis would have been far less beautiful than it is right now.

About the Author

September 17, 1985	Born in Turin, Italy
2004 – 2007	BSc in Physics, University of Turin Bachelor thesis: *Generation of ocean waves by wind*
2007 – 2009	MSc in Environmental Physics, University of Turin Master thesis: *Lagrangian models for atmospheric dispersion with chemical reactions*, in cooperation with the Italian National Research Council (CNR)
2010 – 2014	Ph.D. project, *The role of clouds in climate model bias and sensitivity*, Delft University of Technology, in cooperation with the Royal Netherlands Meteorological Institute (KNMI)
Present	Post-doctoral researcher in *Aerosol radiative effects*, Netherlands Institute for Space Research (SRON), Earth and Planetary Science (EPS) division, Utrecht

Peer-reviewed Publications

---

in preparation	**Lacagnina Carlo** and Otto Hasekamp. Global ocean evaluation of the aerosol single scattaring albedo estimated by AeroCom models against PARASOL. *J. Climate*.
under review	**Lacagnina Carlo**, Frank Selten and A. Pier Siebesma. Impact of changes in the formulation of cloud-related processes on model bias and model climate sensitivity. *Journal of Advances in Modeling Earth Systems*.
2014	Webb M.J., A.P. Lock, A. Bodas-Salcedo, S. Bony, J. Cole, **C. Lacagnina**, F. Selten, H. Kawai, T. Koshiro, R. Roehrig and B. Stevens. The diurnal cycle of cloud feedback in climate models. *Climate Dynamics*.
2014	**Lacagnina Carlo** and Frank Selten. Evaluation of clouds and radiative fluxes in the EC-Earth general circulation model. *Climate Dynamics*.
2013	**Lacagnina Carlo** and Frank Selten. A novel diagnostic technique to investigate cloud-controlling factors. *J. Geophys. Res. Atmos.*, Vol. 118, pp. 5979-5991.
2013	**Lacagnina Carlo** and Frank Selten. Changes in the cloud properties in response to El Niño: a bivariate approach. *Climate Dynamics*, Vol. 40, Issue 11-12, pp. 2973-2991.
2012	Ferrero Enrico, Luca Mortarini, Stefano Alessandrini and **Carlo Lacagnina**. Application of a Bivariate Gamma Distribution for a Chemically Reacting Plume in the Atmosphere. *Boundary-Layer Meteorology* (2012): 1-15.
2012	Ferrero Enrico, Luca Mortarini, Stafano Alessandrini and **Carlo Lacagnina**. A fluctuating plume model for pollutants dispersion with chemical reactions. *International Journal of Environment and Pollution* (2012): Volume 48, Number 1-4.